FABRICATION AND CHARACTERIZATION OF COMPOSITE DIAMOND LIKE CARBON FILMS FOR SOME APPLICATIONS

Zhang Ping

SCHOOL OF ELECTRICAL & ELECTRONIC ENGINEERING
NANYANG TECHNOLOGICAL UNIVERSITY

2005

Fabrication and Characterization of Composite Diamond Like Carbon Films for Some Applications

Zhang Ping

School of Electrical and Electronic Engineering

A thesis submitted to the Nanyang Technological University
in fulfilment of the requirement for the degree of
Doctor of Philosophy

2005

Acknowledgments

I would like to express my grateful thanks to my supervisor, Associate Professor Tay Beng Kang. Without his full support, encouragement and guidance, this work would not have been completed.

I would like to give my special thanks to my parents for their understanding, encouragement and support for my study from the primary school all the way to the postgraduate degree.

I also would like to thank Mr. Cheng Guan Yow of Surrey University, Professor SPR Silva of Surrey University, Associate Professor Lau Shu Ping, Associate Professor Sun Chang Qing, Associate Professor Li Chang Ming, Dr. Cheng Jing Sheng of Data Storage Institute, Dr. Sheeja, Dr. Yu Guo Qing, Dr. Guo Jian Xin of Hong Kong Philips Pte Ltd, Dr. Zhang Yue Bin, Dr. Huang Lei, Dr. Wang Gang of City University of New York, Dr. Chen Bai Jun, Assistant Professor. Daniel Chua of National University of Singapore, Professor Sun Zhuo of East China Normal University, Dr. Gan Zheng Hao, Dr. Li Zhi Qing, Dr. Zhao Zhi Wei, Mr. Li Jun Feng, Mr. Yu Liu Jiang, Mr. Zhong Wei Hua, Mr. Pan Li Kun, Mr. Lee Hiong Wen, Ms. Sze Jia Yin, Mr. Clemens Yuan, Ms. Ji Xiao Hong, Dr. Gao Jian Xia and all my friends for their help and constructive discussion on this project.

I would also like to express my thanks to the technicians of Ion Beam Processing Lab, Ms. B. G. Neo, Ms. Janet Teh and Mr. Hasman bin Hassan, for their co-operation.

Finally yet most importantly, I would like to thank the Nanyang Technological University for the scholarship awarded to me for my postgraduate study.

Summary

The filtered cathodic vacuum arc (FCVA) technique is powerful for thin film deposition. In this project, several sets of metal containing amorphous carbon (a-C:Me) films were successfully deposited, from metal/carbon composite targets, by using an FCVA system. A systematic investigation of such films has been carried out. The composition of the films and the chemical state of each element were studied by X-ray photoelectron spectroscopy (XPS). The microstructure of the carbon matrix was characterized by Raman scattering. Transmission electron microscope (TEM) was used to study the nano structure. X-ray diffraction (XRD) was used to study the metal cluster crystalline status of the films. The films surface morphology and roughness were determined by atomic force microscopy (AFM). The hardness and Young's modulus were studied using Nanoindentor. Video contact angle (VCA) was used to measure the contact angle. Four-point probe was used to determine the electrical resistivity. Cyclic voltammetry (CV) and electrochemical impedance spectroscopy (EIS) methods were adopted to study the electrochemical properties.

The metal composition in all a-C:Me films increases is always larger than that in the composite targets. The low melting point of the metals in comparison with C is considered as the major reason. TiC and SiC have been found in a-C:Ti and a-C:Si films, respectively. There is no carbide phase observed in a-C:Al and a-C:Ni films.

The Raman study shows that the sp^2 cluster size and composition increase following the increase in metal composition in the targets. The sp^2 cluster size in a-C:Al films is sensitive to the substrate bias while there are not much change for a-C:Ti and a-C:Si

films. 1.89 nm nanocrystalline Ni nanoparticles have been found in a-C:Ni films by TEM and confirmed by XRD.

Metal incorporation such as Ti, Al and Si has been found to be an effective method to decrease the internal stress of ta-C films deposited by the FCVA technique. Though such incorporation results in the decrease of hardness and Young's modulus, their values remain relatively high (much higher than that of a-C:H films). The existence of the TiC and SiC contributes to the higher internal stress, hardness, and Young's modulus of a-C:Ti and a-C:Si films.

The contact angle of a-C:Me films remains relatively constant as a function of different substrate bias and metal composition. The contact angles of a-C:Al, a-C:Ti, a-C:Ni, a-C:Si are around 102°, 95°, 80°, 65°, respectively. The absorption of oxygen on the surface plays an important role on the surface energy of a-C:Me films. Under ultraviolet (UV) irradiation, a-C:Ti films shows a reversible wettability.

With the metal composition increases, the electrical resistivity of a-C:Al films decreases from 40 to 10 Ω-cm and that of a-C:Ti films decreases from 133 to 2.3 × 10^{-4} Ω-cm. In CV study, a-C:Ti films exhibit a wide electrochemical window. The EIS study shows the sensitivity of a-C:Ti films to the negative ions solution is much higher than that to the positive ions solution.

The successful applications of a-C:Me films in information display and bio-MEMS fields have also been shown.

Table of Contents

List of Figures

List of Tables

Chapter 1. Introduction

1.1 Motivations

Diamond-like carbon (DLC) films of different forms have been investigated in the past three decades since the work of Aisenberg and Chabot [1]. They used an ion-beam source to deposit thin carbon films on Si substrates. Since the deposited carbon films have electrical and optical properties similar to those found in natural diamond these films are called 'Diamond-Like Carbon' (DLC) films. These DLC films are predominantly amorphous in nature. They demonstrated the essential role of the particle energy in obtaining hard, substantially amorphous, carbon films with a significant sp^3 bonded carbon component. A variety of methods (ion beam, arc, laser ablation, sputtering, plasma) [2, 3, 4, 5, 6] employ energetic species to deposit these films which may contain hydrogen (a-C:H) or may be hydrogen free (a-C). The DLC with very high sp^3 composition is also named tetrahedral amorphous carbon (ta-C).

The unique set of properties of DLC can be summarized as [2-6]:

1. high hardness and elastic modulus;
2. excellent wear resistance;
3. low coefficient of friction;
4. chemical inertness;
5. bio-compatibility;
6. smooth surface;

7. transparency in the IR region and visible region;
8. high band gap;
9. high resistivity and dielectric strength; and
10. good thermal conductivity.

Due to its rapid developments in the 1980s, a-C:H films have succeeded in gaining several important market niches including:

1. protective coatings for recording (hard discs media and head) [7];
2. a standard solution for a variety of tribological applications; and
3. protective optical coatings (for IR applications) [8].

In a comparison, the properties of hydrogen-free a-C films surpass that of a-C:H films in the following terms [9]:

1. similar or higher deposition rates;
2. significantly higher hardness, elastic modulus and lower wear rate;
3. a much better adhesion to lots of substrates;
4. a much higher thermal stability (>700^{o}C for a-C in vacuum, > 550^{o}C in oxygen, 300^{o}C for a-C:H in vacuum above which hydrogen is evolving, 250^{o}C in oxygen); and
5. better optical properties in the IR range (no C-H stretches).

Hence, a-C films will eventually substitute for a-C:H films in their traditional niches as well as establishing new market niches. One example is the Gillette® "MACH III" [10], a razor blade which is coated with a-C films and has claimed superior performance over conventional blades.

However one main drawback of DLC films is the high internal stress. Such stress can reach values higher than 10 GPa in a-C [11], and approximately 3 GPa in a-C:H [12]. Stress is widely accepted to be an intrinsic property of DLC films arising from the deposition mechanism creating the sp^3 bonds. There are various models trying to explain the development of stress in the deposition process. Different mechanisms for the growth mechanism of ta-C films have been proposed, such as the subplantation model by Lifshitz et al. [13] and stress-induced phase transition processes by McKenzie et al [14]. Analytical expressions for the subplantation process describing the formation of stress and the densification have been proposed by Davis [15] and Robertson [16]. The basic idea of the models by Davis and Robertson is that a carbon ion needs at least the displacement energy to penetrate into the carbon film leading to a densification of subsurface layers of the evolving film [13]. But, not all the energy of the energetic carbon ion is used for penetration (displacement processes). Part of the ion energy is used by momentum transfer collisions that results in a thermal spike. Davis and Robertson modified calculations of Windischmann [17] by allowing implanted carbon atoms to relax to the film surface, due to the high localized temperature generated by the impinging C^+ ions in the thermal spike. The main difference is that the Davis model did not account for densification in the increase in ions, assuming a fixed Young's modulus and Poisson ratio in the calculations.

Robertson's model accounts for the increase in number of ions, a much more denser film is obtained and also explains the increase in stress. In both models, the description of formation of sp^3 bond and hence, the density of the film is synonymous with the intrinsic stress of the film.

This high stress will easily cause DLC films delaminating from their substrates. It limits the applications of DLC films, especially when making thick films, which can be used for carbon based microelectromechanical systems (MEMS).

For the a-C:H film, it has been shown the stress can be effectively reduced by introducing metal into the films. To date, metals including W, Ti, Ta, Fe, Ni, Cr, Cu, Co, Ru, Au, Sn, and Mo has been reported to be successfully incorporated into a-C:H films[18, 19, 20, 21, 22, 23, 24, 25]. The properties of such metal containing hydrogenated amorphous carbon (a-C:H:Me) films have been studied in detail. For example, the hardness of a-C:H:Mo, a-C:H:Ti, a-C:H:Ta, and a-C:H:W films follows the increase in metal composition. This is attributed to the formation of metal carbide clusters within the a-C:H:Me films. The Young's Modulus value for a-C:H:Mo, a-C:H:Ti, a-C:H:Ta, and a-C:H:W films also follows the increase in metal composition. The coefficient of friction for an a-C:H:Ta film with 13 at.% Ta is found to be as low as 0.04 [25]. A sharp change in electrical resistivity from highly insulating to metallic-like has also been reported for a-C:H:Mo, a-C:H:Ru, a-C:H:Ta, a-C:H:Co, and a-C:H:Au films [23, 24, 25]. Therefore, metal incorporation is a good method to improve the properties of DLC films.

Since the properties of a-C:H films can be improved by incorporation of metals, it is interesting to investigate incorporation of metal into hydrogen-free a-C films. Monteiro et al [26] have reported that 4 at.% W was incorporated into a-C films by using a dual source filtered vacuum cathodic arc (FCVA) system. The intrinsic stress of W containing amorphous carbon (a-C:W) film reduces from a high of 10GPa to 1-2 GPa. Chhowalla et al [27] have reported that 2 and 4 at.% B was incorporated into a-C films by using a B/C composite target in an FCVA system, the intrinsic stress of B containing amorphous carbon (a-C:B) film reduces from a high of 10GPa to 1-3 GPa. Wei et al [28] have reported that Cu and Ti were successfully incorporated into a-C films by using a pulse laser deposition (PLD) system. Cu and Ti containing amorphous carbon (a-C:Cu and a-C:Ti) films show a better wear resistance than that of a-C film. Recently, Gerhards et al [29] have reported synthesis of a-C:Cu film by using a mass selected ion beam deposition (MSIBD) system. Feng et al [30] have reported deposition of a-C:Ti film by using an unbalanced magnetron sputter (UBS) system.

Though some results have been achieved for a-C:Me films, most reports are focused on the mechanical properties. A detailed and systematic research work on a-C:Me film, such as the relation between the metal composition and the structure of the films, the relation between the ion energy and the structure of the films, electrical properties, and the surface energy of a-C:Me films, is required.

In the hydrogen-free a-C deposition methods, the ion energy of the MSBID technique is the easiest for fine control and hence the quality of a-C film produced by this

technique is excellent. However, it suffers from a low deposition rate due to its low flux. The filtered cathodic vacuum arc (FCVA) technique has been successfully developed and used in the deposition of a-C films. It employs a magnetic filter to remove unwanted macroparticles and neutral atoms. By applying a DC or pulse bias to the substrate holder, the ion energy can be finely adjusted. The a-C films can be deposited by the FCVA technique at a high deposition rate and the quality of a-C films is comparable to that of a-C films by the MSBID technique. More details will be described in chapter 2. In additionally, the FCVA system is much cheaper than any other system because of its simplicity. But to incorporate metal into a-C films, the target must contain both metal and C. The metal/C composition target is proposed in this work.

It is well known that Ti is a very important and useful metal. With its excellent mechanical and tribological properties, a-C:Ti film has been reported by different groups [26, 28, 30]. Also as TiC is a good conductive ceramic [31] the electrical properties of a-C:Ti is attractive for study. Since Al in bulk is a light and soft metal, it is expected that incorporation of Al will significantly reduces the stress of Al containing amorphous (a-C:Al) films. Si is in the same column in the elements periodic table as C. Thus a-C:Si may have some unique properties. Though Si is a semiconductor material, for ease of comparison, we call it a “metal” in this work. Another interesting element is Ni. It is expected that Ni containing amorphous carbon (a-C:Ni) films may have ferromagnetic properties. Besides that, Ni is a widely used catalyst in the growth of carbon nanotubes (CNT). Therefore, it is interesting to have a systematic study on a-C:Ti, a-C:Al, a-C:Si, and a-C:Ni films.

1.2 Objectives

The main objectives of this study are to deposit a-C:Ti, a-C:Al, a-C:Si, and a-C:Ni films at different deposition conditions using the FCVA system and to carry out a systematically investigation on such films. Thus, the objectives are summarized as:

a) To fabricate metal/C composition targets with various metal composition. This is the first step for the deposition of the a-C:Me films.
b) To deposit high quality a-C:Me films from metal/C composition targets using the FCVA system.
c) To investigate the microstructure, film composition, and surface morphology using available characterization techniques such as Rutherford back scattering (RBS), X-ray photoelectron spectroscopy (XPS), Raman spectroscopy, transmittance electron microscopy (TEM), X-ray diffraction (XRD), and atomic force microscopy (AFM).
d) To examine the effects of the metal composition and ion energy on the film microstructure, film composition, and surface morphology.
e) To study the surface energy, mechanical and electrical properties of a-C:Me films in detail and explore some applications for a-C:Me films.

1.3 Major Contributions of the Thesis

This thesis includes deposition of a-C:Me films using an FCVA system and characterization of a-C:Me films by different investigation methods. The major contributions are listed below:

- The metal/carbon composite targets have been fabricated. The a-C:Al, a-C:Ti, a-C:Ni, and a-C:Si films have been successfully deposited from composite targets.
- The relation between the film composition and process parameters has been studied in detail. The metal composition of a-C:Me films increases following the increase in that in the composite targets and is always larger than that in the composite targets. The low melting point of the metals in comparison with C is considered as one reason. Another possible reason is the self-sputtering yield difference for the metals and C. The atomic weight of C is much lower than that of the metals and it is much easier to sputter. To further understand the self-sputtering effect, the relation between the film composition and the substrate bias is studied. The metal composition in a-C:Al, a-C:Ti, and a-C:Ni films is found to be the richest at middle-bias (80 V for a-C:Ti, 120 V for a-C:Ni, and 200 V for a-C:Al.). This corresponds to the difference in atomic weight and mean ion charge state of each metal element.
- The influence of the type of metal element, metal composition and substrate bias on the microstructure of the films has been investigated in detail. The Raman study shows that the sp^2 cluster size and composition increase

following the increase in metal composition in the targets. The sp^2 cluster size of a-C:Al films is sensitive to the substrate bias while not much change for a-C:Ti and a-C:Si films is observed. Like ta-C films, the sp^3 composition of a-C:Al and a-C:Ti films shows a higher value at middle-bias (80 - 120 V). 1.89 nm nanocrystalline Ni nanoparticles have been found in a-C:Ni films.

- The mechanical properties of a-C:Me films have been investigated in detail. Metal incorporation such as Ti, Al and Si has been found to be an effective method to decrease the internal stress of ta-C films deposited by the FCVA technique. Though such incorporation also results in the decrease of hardness and Young's modulus, their values remain relatively high (much higher than that of a-C:H films). The effect of Al on the internal stress, hardness and Young's modulus is more pronounced than that of Ti and Si. The existence of the TiC and SiC contributes to the higher internal stress, hardness, and Young's modulus of a-C:Ti and a-C:Si films.
- The surface energy of a-C:Me films has been studied in detail. The absorption of oxygen on the surface plays an important role on the polar component of a-C:Me films. The formation of Al-O and Ti-O is responsible for the low polar component. The Ni metallic bond results in a high polar component. As all the films are atomic smooth, the roughness does not have any effect on the surface energy. The photocatalysis mechanism is used to explain the reversible wettability of a-C:Ti films.
- The electrical resistivity of a-C:Ti and a-C:Al films and electrochemical response of a-C:Ti films have been investigated. The electron hopping between sp^2 sites is regarded as the main conduction mechanism. The high

conductivity of the TiC phase in a-C:Ti responds for the low resistivity. Both the CV and EIS studies show the high Ti composition decreases the unique electrochemical properties of DLC. Therefore the low Ti composition a-C:Ti film is more suitable for electrochemical applications.

- The successful growth of carbon nanotubes (CNTs) from a-C:Ni films for display applications and using a-C:Ti coating as a barrier layer in a bio-MEMS mould application have been achieved.

1.4 Organization of the Thesis

This thesis has been organized into the following chapters:

- Chapter 1 introduces the motivations, objectives and major contributions of this thesis.
- Chapter 2 describes the FCVA system, fabrication of composite target, deposition conditions, and characterization methods in detail.
- Chapter 3 reports the microstructure, morphology, composition, surface energy, mechanical, electrical and electrochemical properties of a-C:Ti films in detail.
- In Chapter 4, the microstructure, morphology, composition, surface energy, and mechanical properties of a-C:Si films have been discussed in detail.
- Chapter 5 provides a detailed study on microstructure, morphology, composition, surface energy, mechanical and electrical properties of a-C:Al films.

- Chapter 6 studies the microstructure, morphology, composition, and surface energy of a-C:Ni films.
- Chapter 7 discusses the applications based on a-C:Me films.
- Finally, in Chapter 8, conclusions are made and future work is suggested.

Chapter 2. Film Deposition and Characterization Details

2.1 Introduction

In principle, a carbon atom can adopt three different bonding configurations, sp^3, sp^2 and sp^1 (Figure 2.1). In the sp^3 configuration, each of the carbon's four valence electrons is assigned to a tetrahedrally directed sp^3 hybrid orbital, which then forms a strong σ bond with adjacent atom. At a carbon sp^2 site, three of the four electrons are assigned to the trigonally directed sp^2 hybrids which form σ bonds; the fourth electrons lies in a p_z (p_π) orbital lying normal to the σ bonding plane. The p_π orbital forms weaker π bonds with adjacent p_π orbits. At an sp^1 site, only two of the electrons form σ bonds along ±0x, and the two other electrons are left in orthogonal p_y and p_z orbits to form π bonds.

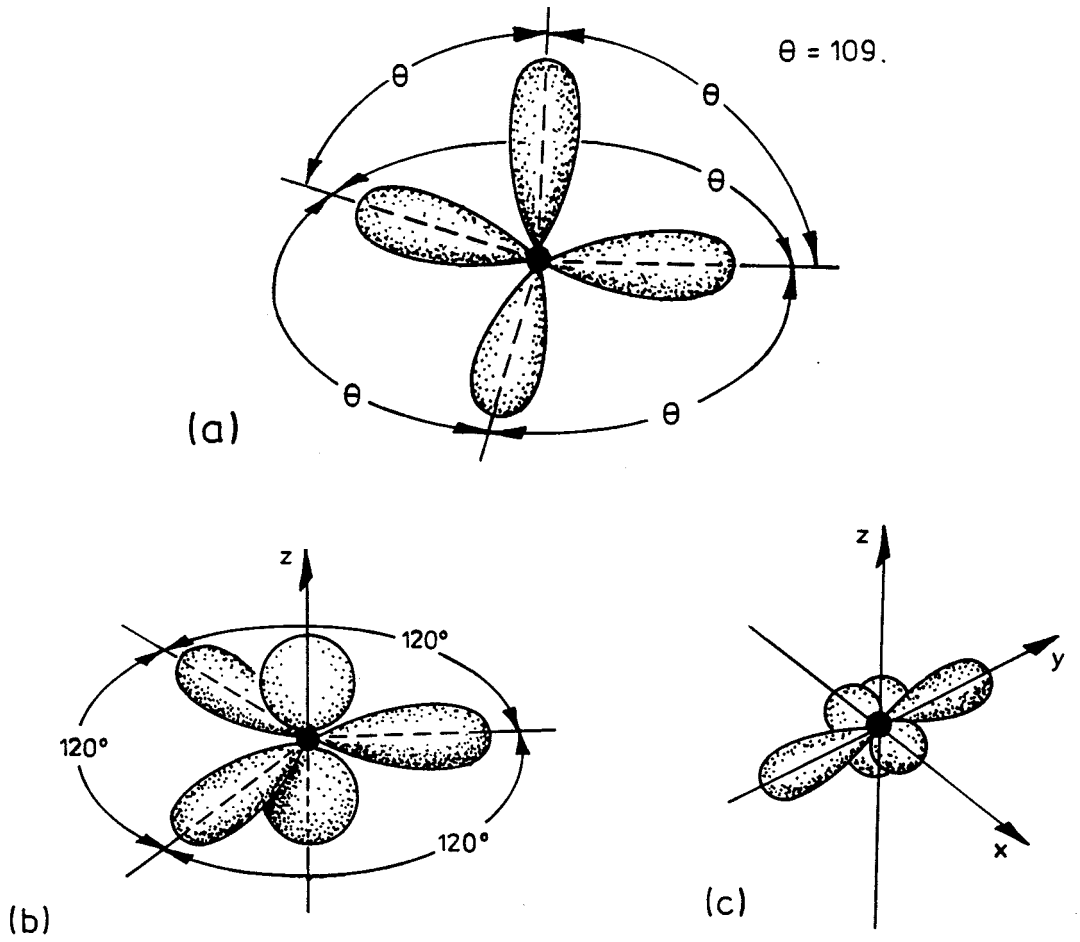

Figure 2.1 Schematic diagrams of (a) sp^3, (b) sp^2 and (c) sp^1 hybridisations of the carbon atom

In nature, single crystal carbon exists in either diamond or graphite. Diamond is a 100% sp^3 bonded structure and graphite is a 100% sp^2 bonded one. The electrical, mechanical, optical properties are very different from each other. Hence the carbon-bonding configuration is very important for the material properties. DLC contains both sp^3 and sp^2 bonds. Therefore DLC has the properties between that of diamond and graphite. Depends on the difference of the sp^3 composition, the properties of DLC can vary a lot.

DLC properties are strongly influenced by the energetic of the deposition process employed. In plasma-based deposition processes the growing film is subjected to a bombardment by a range of species and energies. The plasma variables include the ion energy, density and distribution and the process variables include the deposition rate, gas composition, pressure, flow rate, substrate bias, and substrate temperature.

Among them, the most important parameter is the ion energy. Hyperthermal species (with energy approximately 10 eV to 1 keV) are used extensively in film-deposition technology in the form of plasma and ion-beam techniques. Aisenberg and Chabot [1] initiated the study of DLC films, for which the hyperthermal energy of the species is shown to influence the film properties varying between those of diamond and those of graphite. It is now well established that the deposition process from energetic species is a shallow implantation ("subplantation") process and not a surface process [13]. The dominant factor determining the phase of the evolving films is the relative amount of C species trapped in subsurface layers. This entrapment can result from either direct penetration of the energetic species or momentum transfer to target atoms. The bonding hybridization is expected to adjust readily to the local density, becoming more sp^2 in nature if the density is low and more sp^3 in nature if the density is high. A high density occurs if an incident ion penetrates the first atomic layer of the film, temporarily enters an interstitial position and increases the local density. The local bonding reforms around the atoms to become bulk bonding of the appropriate hybridization. If the ion energy is too low, the ion fails to penetrate and it will just stick to the surface and form sp^2-bonded a-C. At higher energies, the ion will penetrate further into the solid and increase the density in deeper layers. All the

penetrating ions will essentially contribute to the increase in density. However, the ion must also dissipate its kinetic energy. The energy dissipates rapidly in about 10^{-12} s in a "thermal spike" but the energy density is large and available to activate a relaxation of the excess density. The greater the excess energy, the higher is the probability of relaxation. Hence, the optimum ion energy for maximum density is a balance between a sufficient penetrative yield and a small relaxation of the density increment. Therefore, the ion energy is the main crucial parameter for DLC deposition.

In this chapter, the deposition system with its advantages and deposition conditions of composite DLC films will be described in detail.

2.2 Filtered Cathodic Vacuum Arc System

In our study, an off-plane double bend (OPDB) filtered cathodic vacuum arc (FCVA) system is used to deposit metal containing amorphous carbon (a-C:Me) films. During a-C deposition, the carbon plasma is generated from a pure graphite (99.9999%) target in the FCVA system. In order to incorporate metal into the a-C films, the metal/graphite composite target is fabricated and replaces the pure graphite target. The a-C:Me films are deposited from the carbon/metal mixing plasma, which is generated from the composite target.

2.2.1 A schematic diagram of FCVA System

The schematic diagram of a typical FCVA system is shown in Figure 2.2. The whole system includes a cathodic arc source, a plasma-filtering duct, a deposition chamber, and a substrate-biasing supply.

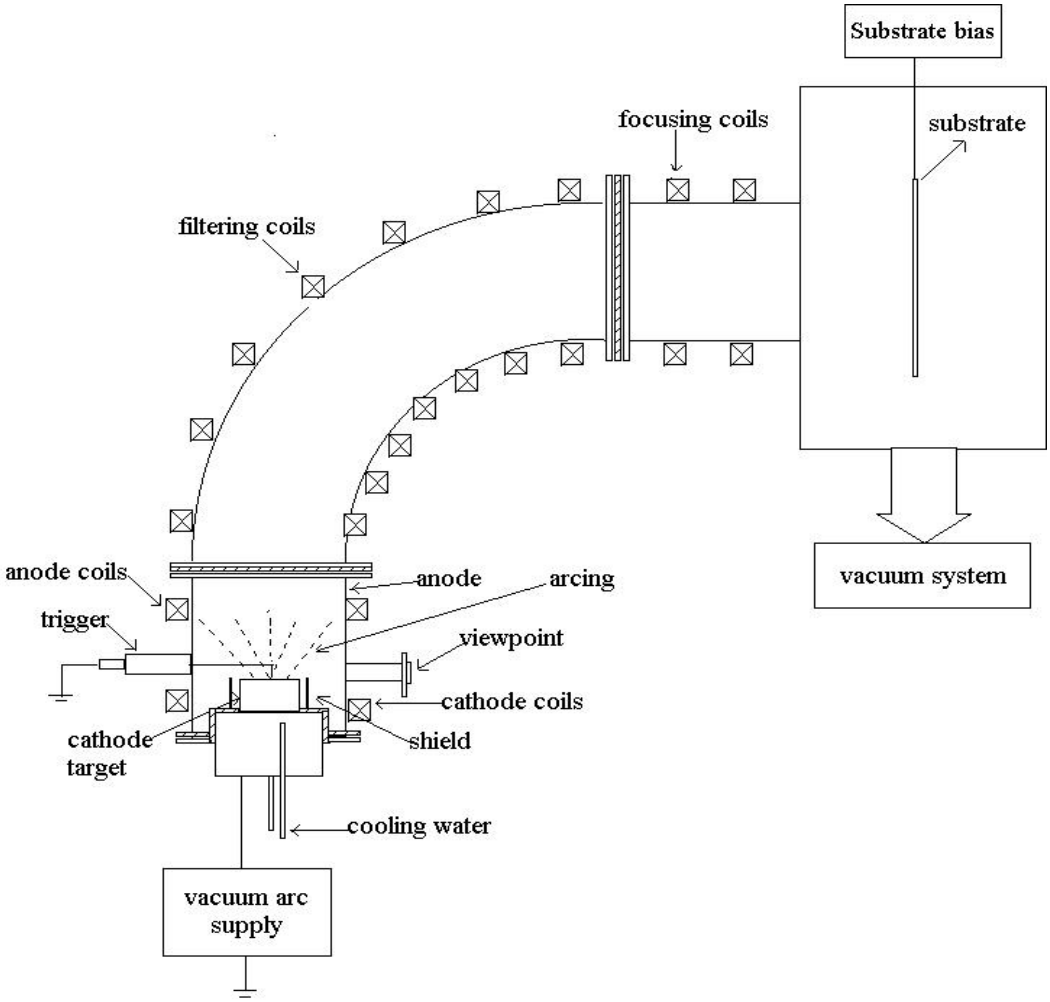

Figure 2.2 The schematic diagram of Filtered Cathodic Vacuum Arc system

2.2.2 The Cathodic Vacuum Arc Source

The cathodic vacuum arc source consists of five parts: a power supply, an arc trigger, a target, a target water-cooling system, and anode/cathode coils. An electrical welding machine (Prestopac 160) with a tunable current of 10 to 250 A is used as the power supply. The anode of power supply is connected to the ground (deposition chamber) and the cathode of power supply is connected to the target. An arc trigger (or a striker) connected to the ground is used to initiate an arc just as in the welding process. The cathode is a 60 mm diameter metal/graphite target mounted onto stainless steel cavity. Both the cathode and anode are cooled by a water chiller. The magnetic field generated by the anode/cathode coils is used to control the cathode arc spot movement.

The vacuum arc is a high current, low voltage electrical discharge between two electrodes in a vacuum ambience. A high current discharge at low voltage cannot be sustained in the vacuum thus a conducting medium is required. The highly ionized plasma, produced by vaporizing the metal/graphite target, works as the conducting media. The vacuum arc can be ignited by bringing the striker to the cathode surface. The triggering circuit is quickly disconnected and the arc is self-sustaining. In this way, the metal/carbon plasma is produced. In our FCVA system, the arc voltage ranges from 18 to 20 V and arc current is typically set at a value from 40 to 100 A. The base pressure of the vacuum is less than 6.7×10^{-4} Pa.

2.2.3 Off Plane Double Bend (OPDB) Filter

The elimination of macroparticles from the ion flux produced by the cathodic arc discharge is important so as to deposit films with good quality. But the use of a macroparticle filter has drawbacks. Filters generally reduce the effective coating rate by a factor of two to ten, depending on the design. The most common filter designs are based on the quarter-torus design, which is published by Aksenov in 1978 [32]. Its basic components are: a tube with a 90° radius bend, magnetic field coils wrapped around it, the cathode at one end, and the substrates to be coated at another end. The bend is sized to eliminate line-of-sight between the cathode and the substrates, while the magnetic field guides the ions and electrons through the filter.

In our FCVA system, a patented steel off-plane double bend (OPDB) torus with a copper coil wound outside, as shown in Figure 2.3, is used. The major advantage of this design over the quarter-torus configuration is that the OPDB filter removes the macroparticles more effectively yet still maintains a high deposition rate [33]. To further improve macroparticle-filtering efficiency, a set of baffles, acting as a mechanical macroparticle filter, can also be installed inside the torus.

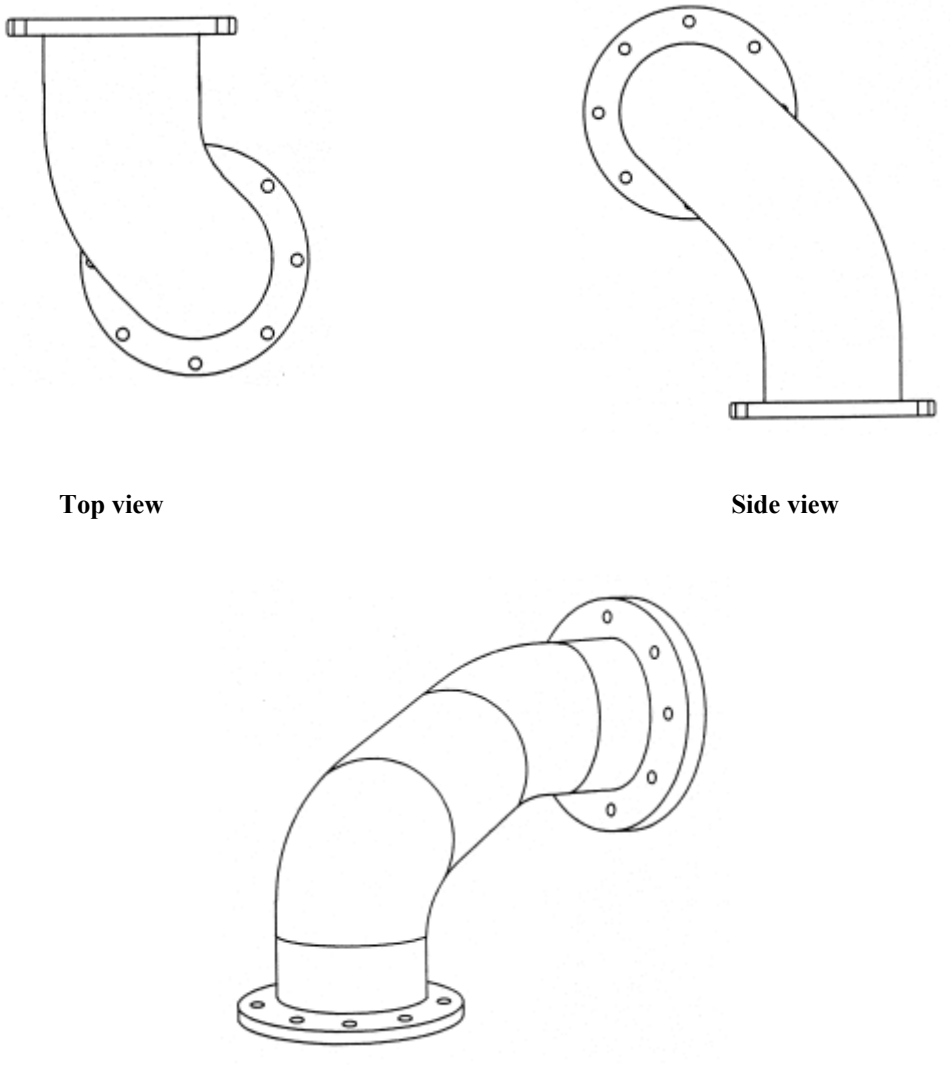

Top view **Side view**

3-D view

Figure 2.3 The off-plane double-bend filter design

The plasma can be scanned by placing field coils at an angle to the filter exit and varying the current in those coils. Since the magnetic field intensity required is just a few mT, the coils and power supplies are simple and straightforward. The commercial FCVA system by the Nanofilm Technologies International Pte Ltd can coat 8-inch wafer with good uniformity in the nanometer scale [34].

2.2.4 Deposition chamber and Bias supply

The deposition chamber, which is grounded, is placed at the exit of the plasma-filtering duct. The vacuum system consists of rotary pump and cryo-pump. The vacuum can be pumped down to 2.67×10^{-4} Pa. The system allows the substrate to be connected to various DC/pulse bias voltages. In this study, a Magtron bipolar system is used. The bias voltage ranges from floating to negative 1000 V.

In the FCVA system, the potential of the plasma beam is obtained with a Langmuir probe. If an electrically floating substrate is placed in the plasma flux, the substrate will have the same potential as the plasma beam, and the ions reaching the substrate will possess their original ion energy. However, if the substrate is biased, the ions will then be accelerated or decelerated within the Debye shielding length when they reach the substrate. The original ion energy in the plasma is measured using a Faraday cup, which was calibrated by an ion beam source with known ion energy. The actual ion energy reaching the substrate can be calculated by [35]:

$$\mathbf{Ei = ne(Vp - Vb) + Eo} \qquad \mathbf{(2.1)}$$

where Ei is the ion energy reaching the substrate, Vp ~ 13 V is the plasma potential [36], Vb is the substrate bias voltage, Eo is the original ion energy in the plasma (~ 28 eV), e is the electron charge, and n is the charge state of the ions in the vacuum chamber.

Comparing with other deposition techniques, our FCVA system with an OPDB filter has several advantages.

1. By applying a bias between the substrate and the chamber, we can easily control the kinetic energy of the ions incident on the substrate. As a result, a more controllable and repeatable results can be achieved.
2. The OPDB filter enables high quality, macroparticle free films to be deposited at a high deposition rate.
3. The system is capable of producing large area uniform coatings with carefully designed scanning and control of the ion beam.
4. Because there is no direct heat transfer from the high temperature arc area to the substrate, the substrate temperature can be independently controlled.

2.3 Fabrication of Composite Target

To incorporate the metal into the carbon films, a metal/graphite composite target is required. By varying the metal element and metal composition, the desired a-C:Me film can be deposited from the corresponding composite target [27]. Therefore, the fabrication of a composite target is the first and very important step for the film deposition process.

By mixing and compacting the high purity small size graphite (99.99% pure, 325 mesh) and metal (99.6% pure, 325 mesh) powder, the composite target is prepared. Firstly, 100 g carbon powder is measured using a high precision digital weighing

machine. According to the desired atomic metal concentration, the weight of the metal is calculated by:

$$W_M = \left(\frac{x\%}{1-x\%}\right) \bullet \frac{M_M}{M_C} \bullet W_C \qquad (2.2)$$

where W_M is the weight of the metal powder, W_C is weight of carbon powder (in our case, it is 100 g), x% is the desired atomic metal concentration, M_M and M_C are the atomic mass of the metal and carbon, respectively. After the calculation, high purity metal powder is measured in the same way. Then the two types of powder are put into the V-shape blender and are mixed for 12 hours to ensure the powder is uniformly mixed. The mixed powder is put into a 60 mm diameter cylindrical stainless steel mould and is pressed under a 0.5 GPa pressure for 30 mins. Finally, by releasing the mould, the fabrication of the composite target is completed.

2.4 Growth Conditions and Related Parameters

In our FCVA system, the deposition parameters that can be varied are: the (a) substrate bias, (b) metal composition in the target, (c) arc current, (d) filter magnetic field. Among them, the substrate bias and metal composition in the target are most important. The substrate bias controls the impinging ion energies on the growing films, while the metal composition in the target will determine the metal composition in the metal/carbon mixed plasma. Therefore, only these two parameters are

considered and investigated in this thesis. The a-C:Me films deposited in this study includes:

a) Two sets of Ti containing amorphous carbon (a-C:Ti) films. One set was deposited from 1, 5, 10, and 20 at.% Ti containing Ti/C composite targets at negative 80 V bias. Another set was deposited from a 5 at.% Ti containing Ti/C composite target at different negative bias ranging from floating to 1000 V.

b) Two sets of Al containing amorphous carbon (a-C:Al) films. One set was deposited from 1, 5, and 10 at.% Al containing Al/C composite targets at negative 80 V bias. Another set was deposited from a 5 at.% Al containing Al/C composite target at different negative bias ranging from floating to 1000 V.

c) Two sets of Si containing amorphous carbon (a-C:Si) films. One set was deposited from 1, 5, 10, and 20 at.% Si containing Si/C composite targets at negative 80 V bias. Another set was deposited from a 5 at.% Si containing Si/C composite target at different negative bias ranging from floating to 1000 V.

d) One set of Ni containing amorphous carbon (a-C:Ni) films. A-C:Ni films were deposited from a 5 at.% Ni containing Ni/C composite target at different negative bias ranging from floating to 1000 V.

According to the previous work on the deposition of ta-C films, the arc current was selected for 80 A and the filter magnetic field was fixed at 40 mT. Before deposition, the deposition chamber was evacuated to a base pressure below 6.67×10^{-4} Pa by a combination of rotary pump and cryo-pump. Highly doped n-type (100) Si wafers, with a resistance about 0.0014 - 0.0020 Ω·cm, and quartz wafers were used as

substrates. Before the substrates were put into the chamber, they were cleaned by acetone, de-ionized water and dried with nitrogen gas. All the depositions were carried out at room temperature. The thickness of the films ranges from 40 – 70 nm. The deposition rate is around 8 – 14 nm/min.

2.5 Characterization Details

2.5.1 X-ray Photoelectron Spectroscopy

XPS is a useful tool to identify and quantify the chemical composition and bonding states in the surface layers of the film. Such a technique involves irradiating the specimen by a monochromatic X-ray source as shown in Figure 2.4. Atoms (except hydrogen) present on the surface possess core electrons, which unlike valence electrons are not directly involved in the bonding. The binding energy of each core electron is characteristic of the individual atom to which it is bound. Since the energy levels are quantised, the photoelectrons have a kinetic energy distribution consisting of a series of discrete bands.

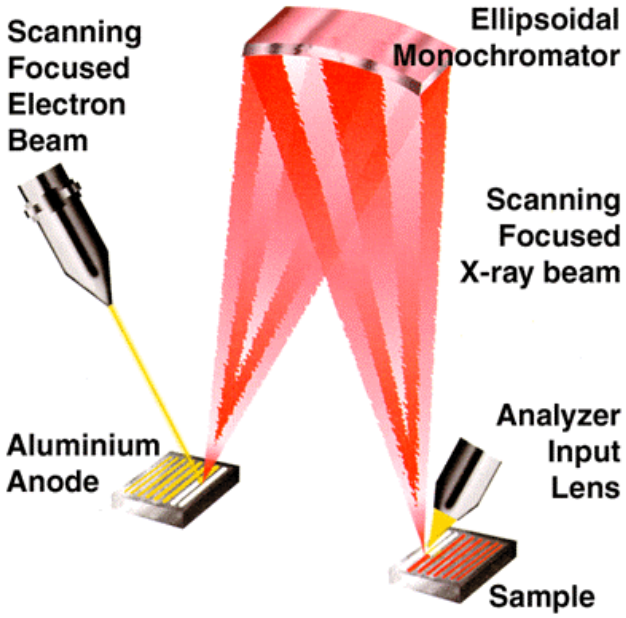

Figure 2.4 The schematic diagram of XPS

XPS experiments has been carried out using a VG MICROLAB 310F spectrometer with an Al K_α (1486.7 eV) X-ray source. The vacuum in the analysis chamber was maintained at about 10^{-6} Pa or lower. Spectra are collected in a concentric hemispherical analyzer in a constant energy mode, with a pass energy Ep of 10 eV. Core-level spectra are obtained by photoelectrons at a take-off angle of 90°, measured with respect to the sample surface. The elemental composition of the films was calculated as [37]:

$$X = (\frac{A_X}{S_X}) / \sum_{i=1}^{N} (\frac{A_X}{S_X}) \qquad (2.3)$$

in which X is the element, A_X is the area under the peak of element X in the spectrum, and S_X is the sensitivity factor.

The analysis of XPS spectrum was done by a widely used free software - XPSPEAK4.1 from Advanced Surface and Materials Analysis Center, Chinese University of Hong Kong. The area of each narrow scan was calculated by the software with a Shirley type background. The sensitivity factors were from VG. The fitting of the XPS spectra was done by XPSPEAK4.1 too. The Gaussian peak shape and Shirley type background was used.

2.5.2 Raman Spectroscopy

Raman scattering is an inelastic scattering process. This means that there is an exchange of energy between the scattered photon and the scattering molecule. The Raman effect probes the vibrational energy levels of molecules and can provide immediate and useful information on the structure and identity of substances in solid, liquid and gaseous phases. The technique is non-contact, non-destructive and requires minimal or no sample preparation. Raman spectroscopy has a number of distinct advantages over Infrared (IR) absorption spectroscopy. Sample preparation in many cases is not required, permitting analysis of bulk or microscopic materials in-situ. Raman spectroscopy has been a well-established technique for the characterization of carbon-based materials [38].

Figure 2.5 illustrates schematic diagram of the Micro Raman Spectroscopy. The Raman spectra are excited using the 514.5 nm line of an Ar^+ laser and collected with backscattering on a CCD camera using a Renishaw 1000 micro-Raman spectroscope. Two multi-layer dielectric filters are used for the rejection of Rayleigh scattering

light. The high-efficiency 1800 grooves mm^{-1} diffraction is used as the single dispersive stage. The spectra range is from 50 to 4000 cm^{-1}. The spectral resolution is 2.0 cm^{-1}.

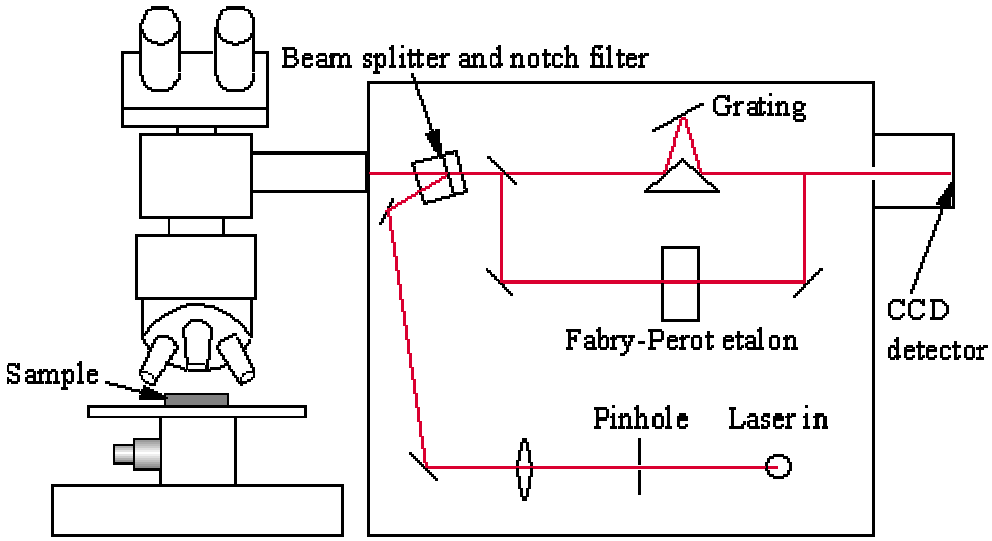

Figure 2.5 The schematic diagram of Micro Raman Spectroscopy

The visible Raman spectrum is largely insensitive to the sp^3 component of the carbon cluster [39]. Therefore, the Raman spectrum monitors the state of the sp^2 carbon component within the films. The asymmetric broad peak in the range 1100-1800 cm^{-1} can be fitted by two peaks centered around 1570 cm^{-1} and 1400 cm^{-1}, defined as the graphite ('G') and disorder ('D') peaks, respectively. This notation arises from the Raman spectrum of nanocrystalline graphite, which generally shows two peaks. One peak is due to the in-plane vibration mode of graphite, and another one is attributed to the small-domain-size graphite region [40, 41].

Proposed by Prawer [42], the G peak is fitted by a Breit-Wigner-Fano (BWF) line-shape with a coupling coefficient Q that represents the skewness of G peak. If the fitting procedure revealed a significant residual in the region of 1350 cm^{-1} (D peak) following fitting of the G peak, the fit is repeated using an additional Lorentzian function for the D peak.

The formulation of the BWF is:

$$I(\omega) = \frac{I_0[1 + 2(\omega - \omega_0)/Q\Gamma]^2}{1 + [2(\omega - \omega_0)/\Gamma]^2} \quad \textbf{(2.4)}$$

where $I(\omega)$ is the intensity as a function of frequency, I_0 is the maximum peak intensity, ω_0 is the peak position, Q is the BWF coupling coefficient and Γ is the full width at half maximum (FWHM). It should be pointed out that the maximum of the BWF line is not at ω_0 but lies at lower frequencies:

$$\omega_{max} = \omega_0 + \frac{\Gamma}{2Q} \quad \textbf{(2.5)}$$

as Q is negative. ω_{max} rather than ω_0 is defined as the G peak position. ω_0 is the position of the undamped mode but has no physical meaning. The Lorentzian line shape is recovered in the limit $Q^{-1} \rightarrow 0$. The BWF line is an effective way to fit the G peak due to the asymmetry of the vibrational density of states (VDOS) of graphite or amorphous carbon towards lower wave numbers [38].

Figure 2.6 shows the BWF line-shape with different Q factors, in which ω_0 is fixed at 1580 and Γ is fixed at 200.

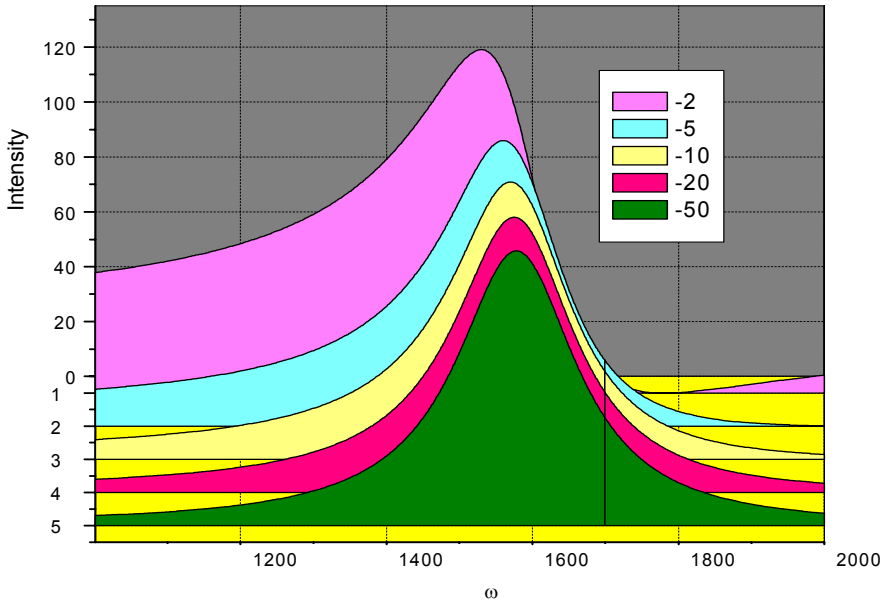

Figure 2.6 The BWF line-shape with different Q factor

2.5.3 Transmission Electron Microscopy

The investigation of the morphology, structure, and local chemistry of metals, ceramics, and minerals is an important aspect of contemporary materials science. Transmission electron microscope (TEM) is an analytical tool that allows detailed nano-structural examination through high-resolution and high-magnification imaging. It also enables the investigation of crystal structures, orientations and chemical compositions in phases, precipitates and contaminants through diffraction patterns, x-ray, and electron-energy analysis. The TEM is an electron-optical microscope that

uses electromagnetic lenses to focus and direct an electron beam. Data is collected from the beam after it passes through the sample. The reason for using an electron beam instead of a light beam is that electrons have a shorter wavelength than photons. Resolution and magnification of a microscope are related to the wavelength and the energy of the radiation. In general, the shorter the wavelength, the better the resolution. Magnifications of up to 5,000,000x and detailed resolution below 1 nm are achieved routinely.

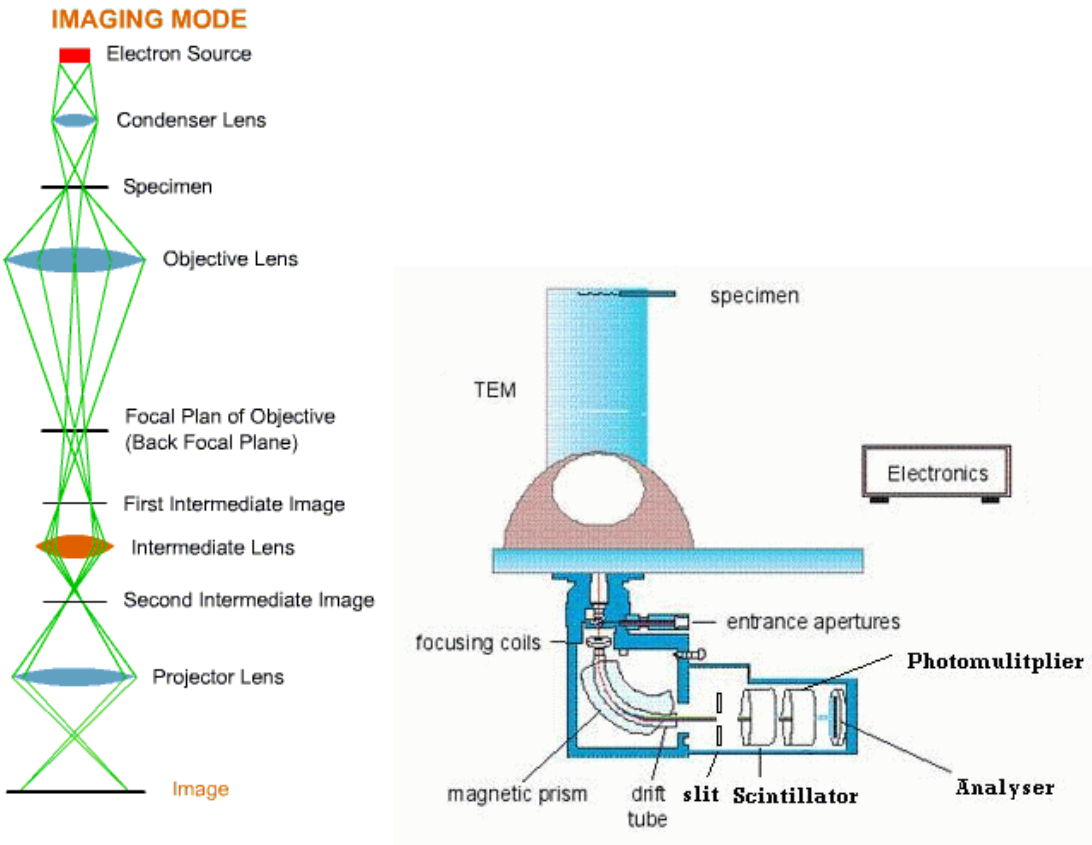

Figure 2.7 Schematic diagrams of TEM and EELS

The schematic diagram of TEM is shown in Figure 2.7. The source radiation is generated using an electron gun. The resulting beam of electrons is focused into a

tight, coherent beam by multiple electromagnetic lenses and apertures. The lens system is designed to eliminate stray electrons as well as to control and focus the electron beam. The corrected beam is focused on the sample. Various techniques are then used to collect data from the electrons that have passed through the sample. For example, image data can be collected by means of a fluorescent screen that is hit by the electron beam. The resulting image may be recorded on photographic film or with a CCD camera linked to a computer.

Electrons that strike the sample and lose some energy in the process are the source of information in EELS. The lost energy is unique to each type of atom that the incoming electron interacts with. By measuring the energy of the scattered electron and subtracting that from the known energy of the incident beam, the energy lost can be calculated. This energy loss indicates what type of atom the electron interacted with and allows chemical identification of the sample. The schematic diagram of EELS is shown in Figure 2.7 together with the TEM.

Some electrons will have undergone only inelastic scattering; that is, they will have lost some amount of energy without a significant change in trajectory and will therefore be contained in the transmitted beam along with the unscattered electrons. The amount of energy the electrons have lost during inelastic scattering will be a function of the scattering they have undergone. These electrons are termed energy loss electrons and can be used for imaging in the STEM mode or for chemical microanalysis.

To collect these electrons for imaging or microanalysis, a magnetic-sector spectrometer and scintillator/photomultiplier detector are placed at the bottom of the microscope column. By scanning over the entire range of electron energies, energy loss spectrum can be collected for microanalysis. By using the spectrometer to collect only electron of live energy, the collected signal can be used to modulate the CRT and produce a scanning image in the STEM mode. Because there is a relationship between some of the energy loss electrons and the atomic species with which they interacted, scanning elemental maps can be generated.

2.5.4 X-ray Diffraction

X-ray Diffraction (XRD) is widely used for the characterization of lattice constant and surface orientation of crystalline materials. In principle XRD measurements measure the distances between planes with x-ray waves (wavelength of a few tenths of a nm). Figure 2.9 shows the schematic diagram of XRD. When

$$n\lambda = 2d\sin\theta \tag{2.6}$$

is satisfied a peak will be measured.

Unlike crystalline materials, due to the lack of long-range ordering, no characteristic diffraction peaks appear in the XRD patterns of amorphous materials. However the short-range ordering in nanocrystalline structure will lead to the presence of some

broadened peaks in the XRD patterns. This makes XRD suitable for the detection of nanocrystallines embedded within the amorphous matrix and to identify their orientation and size.

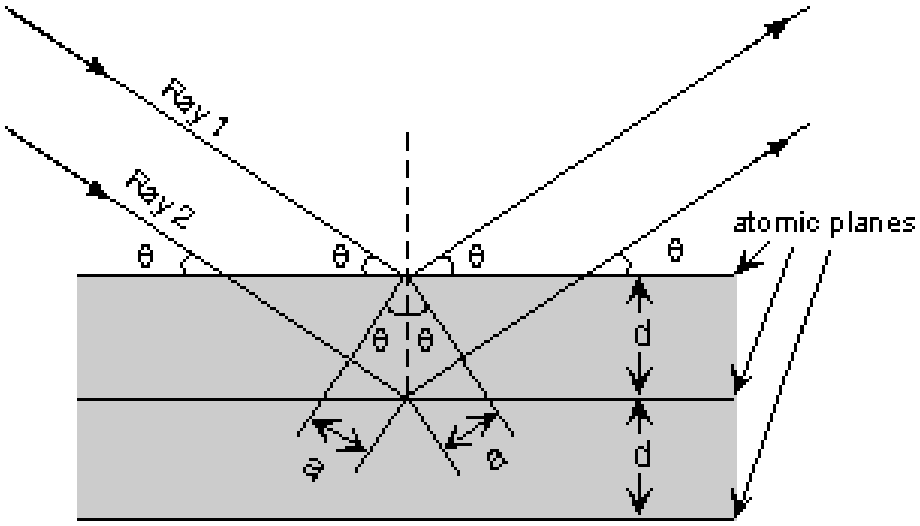

Figure 2.8 The schematic diagram of XRD

For the XRD of thin films, the glancing angle mode is effective and is able to avoid the signal from the Si substrate. In my experiments, the incident angle of the X-ray was fixed at 1^{o}.

2.5.5 Atomic Force Microscopy

Atomic force microscopy (AFM) works by scanning a fine ceramic or semiconductor tip over a surface in much the same way as a phonograph needle scans a record. As shown in Figure 2.9, the tip is positioned at the end of a cantilever beam and is shaped much like a diving board. As the tip is repelled by or attracted to the surface, the cantilever beam deflects. The magnitude of the deflection is captured by a laser that

reflects at an oblique angle from the very end of the cantilever. A plot of the laser deflection versus tip position on the sample surface provides the resolution of the hills and valleys that constitute the topography of the surface. The AFM can work with the tip touching the sample (contact mode), or the tip tapping across the surface (tapping mode) much like the cane of a blind person.

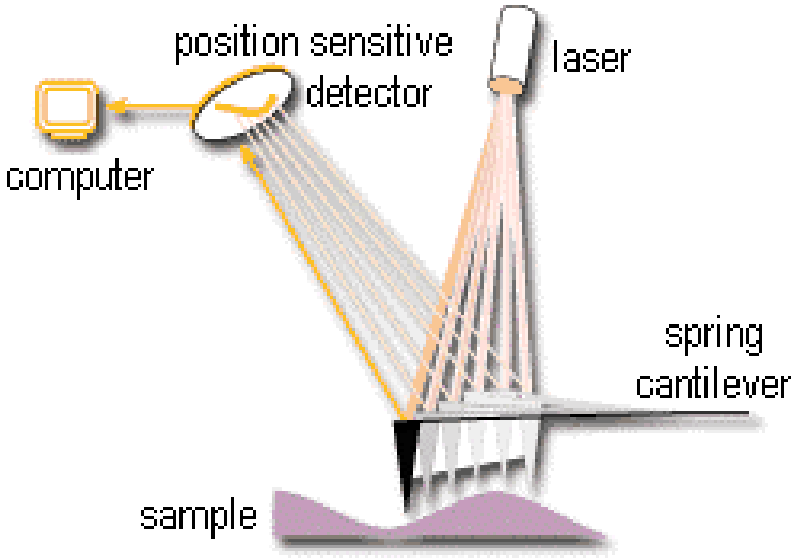

Figure 2.9 The schematic diagram of AFM

The surface morphology was measured by atomic force microscopy (AFM) with tapping mode (Dimension 3000 Scanning Probe Microscope, Digital Instruments). The surface texture of the a-C:Me films was studied over large segments of the substrate with an area of 1 μm^2 at a time. The surface roughness of a-C:Me films was studied in terms of their root mean square (RMS) surface roughness. RMS roughness is defined as:

$$R_{RMS} = \left(\frac{1}{N} \sum (Z_i - Z_{ave})^2 \right)^{1/2} \quad (2.7),$$

where Z_{ave} is the average of the height values within a given area. Z_i denotes the height at the ith location amongst the N points monitored within the area scanned.

2.5.6 Surface energy

The surface free energy (or surface tension) of the films was determined by contact angle measurements. The correlations between contact angle and surface free energy between the solid surface and a liquid droplet is provided by Young's equation [43]:

$$\gamma_{sv} = \gamma_{sl} + \gamma_{lv} \cos\theta \quad \textbf{(2.8)}$$

where γ_{sv} and γ_{lv} are the solid and liquid surface energies, respectively; γ_{sl} is the solid/liquid interfacial energy and θ is the contact angle, as shown in Figure 2.10.

Figure 2.10 The droplet on the solid surface

The contact angle θ and the liquid surface energy γ_{lv} are measurable parameters. In order to determine the surface energy of the solid through the measurement of the contact angle, various theoretical statements describing the interfacial energy γ_{sl} as γ_{sl} = f(γ_{lv} ,γ_{sv}) is used. In this work, the harmonic-mean method was used [44]:

$$(1+\cos\theta)\gamma_{lv} = 4\left(\frac{\gamma_{sv}^{d}\,\gamma_{lv}^{d}}{\gamma_{sv}^{d}+\gamma_{lv}^{d}}+\frac{\gamma_{sv}^{p}\,\gamma_{lv}^{p}}{\gamma_{sv}^{p}+\gamma_{lv}^{p}}\right) \quad \textbf{(2.9)}$$

Here $\gamma_{lv} = \gamma_{lv}^{d} + \gamma_{lv}^{p}$ and the superscripts *d* and *p* refer to the dispersion and polar components, respectively. When two liquids are used, and the values of γ_{lv}^{d} and γ_{lv}^{p} for these liquids are known, the dispersive and polar components of the solid surface energy (γ_{sv}^{d} and γ_{sv}^{p}) can be obtained by solving the two simultaneous equations.

Table 2.1 The dispersive (γ_{lv}^{d}) and polar (γ_{lv}^{p}) components and total surface energy (γ_{lv}) for selected test liquids

Liquid	γ_{lv}^{d} (mN/m)	γ_{lv}^{p} (mN/m)	γ_{lv} (mN/m)
Water	22.1	50.7	72.8
Formamide	39.5	18.7	58.2
Methylene iodide	48.5	2.3	50.8

The measurement of the contact angles of a-C:Me films were carried out in atmospheric conditions at 20^{o}C using a VCA Optima device from AST Products, Inc.. The test liquids (water, formamide and methylene iodide) along with their surface energy (γ_{lv}) as well as the dispersive (γ_{lv}^{d}) and polar (γ_{lv}^{p}) components are detailed in Table 2.1. A droplet with a volume of 0.5 µl was released onto the surface of sample using a syringe needle. The contour of the liquid drop on the solid surface was captured by a CCD camera after 5 seconds, which is to ensure the liquid drop has reached the equilibrium. For each sample and liquid, at least three drops were measured. The accuracy of the contact angle is better than 1^{o}.

2.5.7 Mechanical property

A Tencor P10 surface profiler was used to measure the internal stress of the films. The stress was determined by the radius-of-curvature method [45], which compares the curvature of the bare silicon substrate with that when a thin film is grown on it. The stress σ_s for a thin film of thickness t_c is given by the radius-of-curvature method:

$$\sigma_s = \frac{E_s}{6(1-\nu_s)}\frac{t_s^2}{t_c}\left(\frac{1}{R}-\frac{1}{R_0}\right) \qquad \textbf{(2.10)}$$

where E_s, ν_s, and t_s are Young's modulus, Poisson ratio, and thickness of the substrate. R and R_0 are the radii of curvature of the film-substrate composite and bare substrate, respectively. For a silicon substrate, the E_s =180 GPa, ν_s = 0.26. Several

marks were made on each sample for the position calibration of the curvature measurement. The stress calculated from different points on a same samples show good agreement. The average value calculated from different points of the same sample is used for the stress of that sample.

The hardness and Young's modulus of the films were measured using a Nanoindenter® II from Nano Instrument, Inc. The nano-indenter was operated in a constant-displacement-rate continuous stiffness mode [46]. The continuous stiffness measuring technique was used to measure the film stiffness continuously without the need for discrete unloading cycles. It therefore allows the measurement to be done at small penetration depths and enables hardness and Young's modulus to be measured simultaneously.

2.5.8 Four-Point Probe

A four-point probe with four tungsten pins placed at equal intervals and in line with each other was used to measure the electrical resistivity of a sample. To eliminate the substrate influence on the experimental result, quartz was used as the substrate. The electrical resistivity of the film was calculated as:

$$\rho = \frac{\pi \cdot t_c}{\ln 2}\left(\frac{V}{I}\right) \tag{2.11}$$

where V and I are the measured voltage and current, t_c is the thickness of the film.

Chapter 3. Ti Containing Amorphous Carbon Films

3.1 The Film Composition and Chemical Bonding States

The film composition of a-C:Ti films was calculated by XPS. The chemical bonding state of each element was studied by a narrow scan XPS.

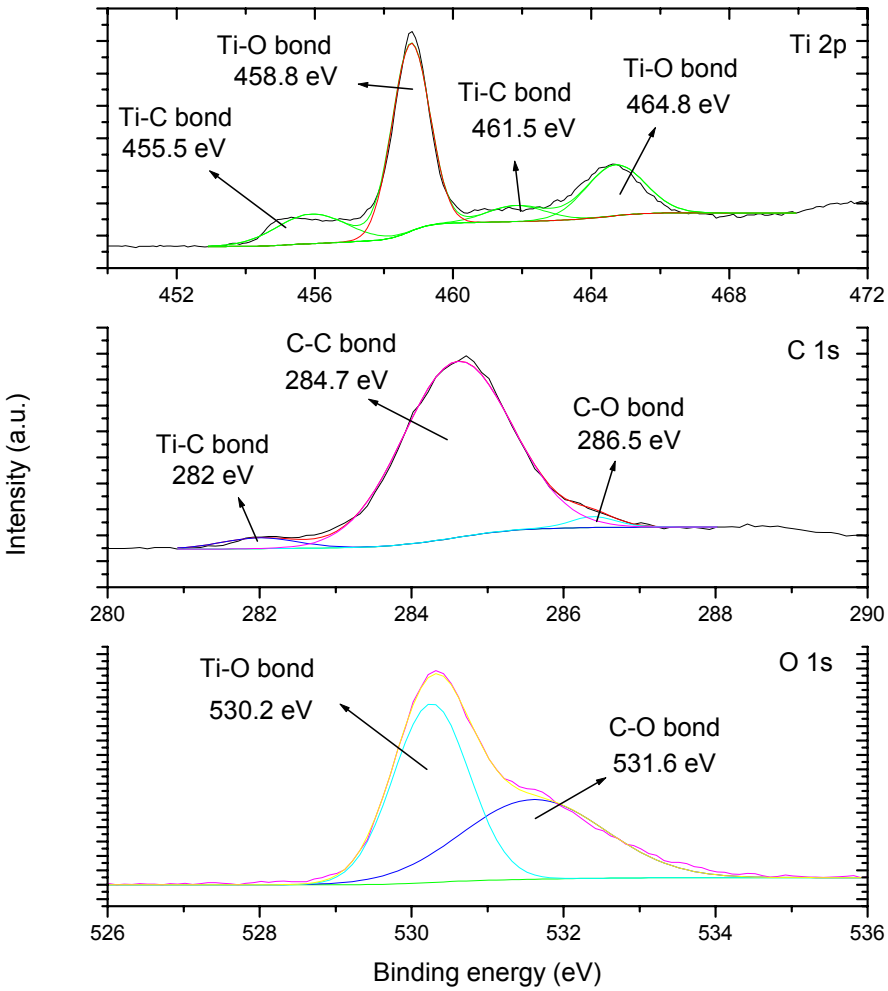

Figure 3.1 Narrow scans of an a-C:Ti film deposited from a 5 at.% target at –80 V bias

Typical Ti 2p, C 1s, and O 1s XPS spectra of an a-C:Ti film are shown in Figure 3.1. The Ti 2p peak corresponds to two sets of spin-orbit doublets, each separated by 6 eV, including Ti-C bond (Ti $2p_{3/2}$ at 455.5 eV, Ti $2p_{1/2}$ at 461.5 eV) and Ti-O bond (Ti $2p_{3/2}$ at 458.8 eV, Ti $2p_{1/2}$ at 464.8 eV) [47]. The C 1s peak can be presented as three components. The peak around 282.0 eV is assigned to the Ti-C bond. The peak around 284.7 eV corresponds to C-C bond. The peak around 286.5 eV is attributed to the C-O bond. Because there is no oxygen involved in the deposition process, it is believed that oxygen was absorbed from the environment and chemically bonded with the metal and carbon when the freshly deposited films were removed from vacuum chamber.

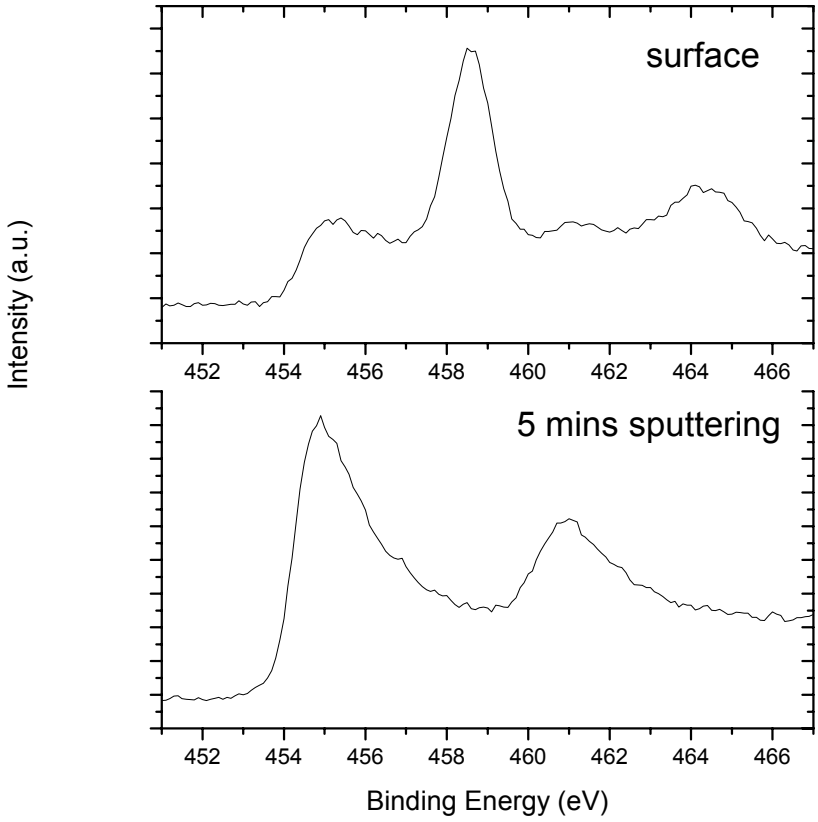

Figure 3.2 Ti 2p narrow scans before and after 5 mins sputtering

In order to confirm that the oxygen was absorbed from the environment, the XPS spectra were acquired after the sample was etched for 5 mins by Ar ions. The narrow scans of Ti 2p before and after etching are shown in Figure 3.2. Clearly, the peaks corresponding to Ti-O bond disappear, confirming that oxygen on the film surface was absorbed from the environment.

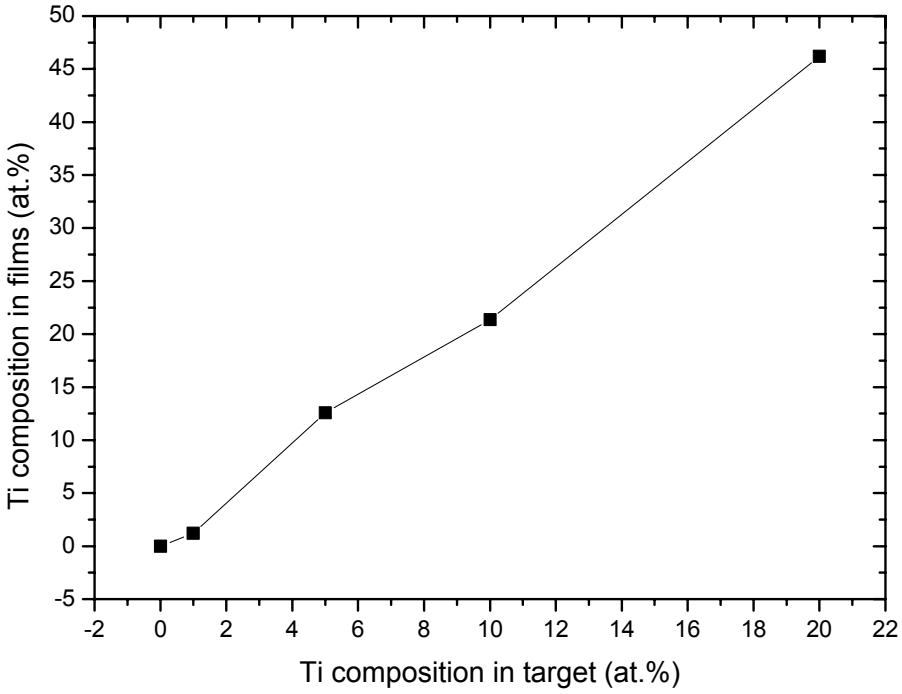

Figure 3.3 The Ti composition in films vs. the Ti composition in targets

The Ti composition of a-C:Ti films deposited from different Ti composition targets is shown in Figure 3.3. The Ti composition in the films increases with the increase in metal composition in the targets and is always larger than that in the targets. This is attributed to two reasons. The first reason is due to the lower melting point of Ti (~1660^{o}C) than that of graphite (~3870^{o}C). Hence, the Ti particles in the arc spot area are completely sublimated and consequently ionized. In contrast, the graphite particles

are partly evaporated with the formation of macro-clusters and micro-particles, which are trapped by the OPDB filter. Thus the metal ion composition in the plasma is higher than that of composite target. Another possible reason is due to the subplantation of Ti atoms. The details are discussed in Chapter 7.

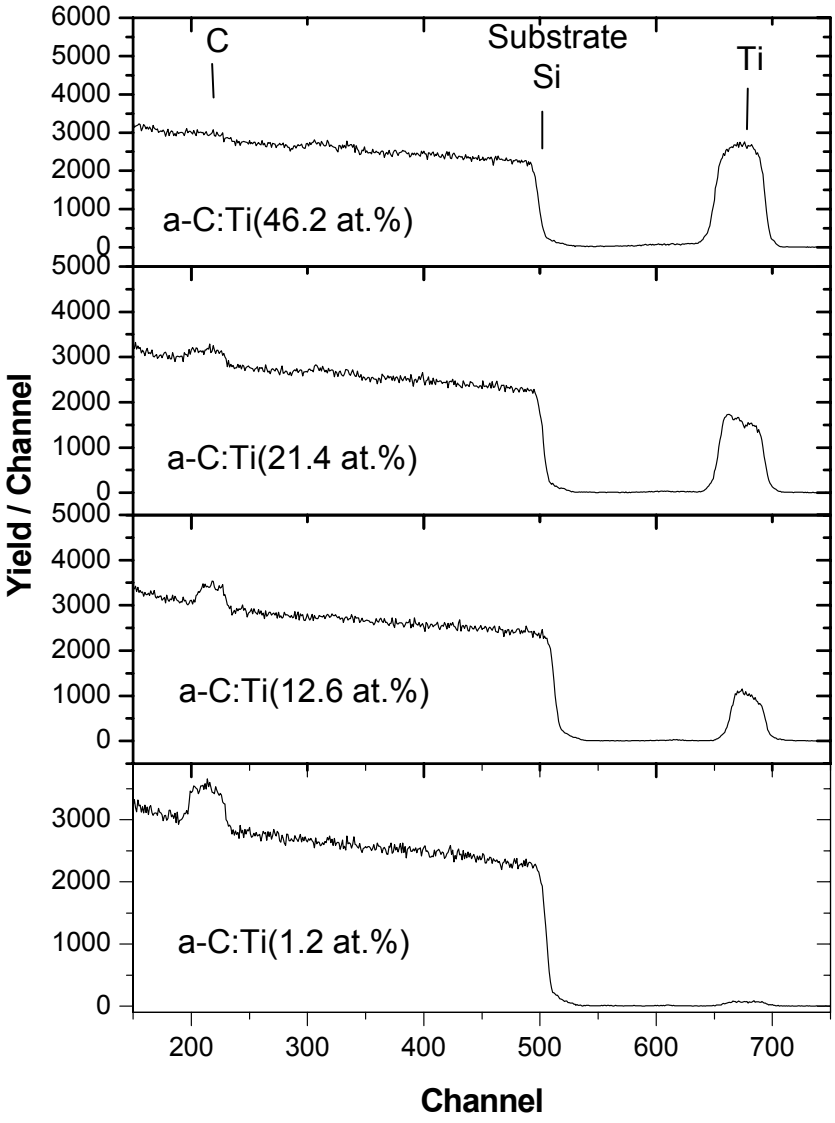

Figure 3.4 RBS spectra of a-C:Ti films

The RBS was taken to further study the film composition. In RBS analysis, a beam of 2 MeV He^{++} ions was projected into the film with an incident angle of 7^{o} to the

normal of the surface of the film, while backscattered He^{++} ions were detected at a scattering angle of 170^{o}. In Figure 3.4, the Ti signal increases and carbon signal decreases gradually with the increase in Ti composition in the targets. This indicates the Ti composition in the film gradually increases. This is no obvious signal of O existing. It shows the O does not exist in the bulk of the film. This conclusions are in consist with XPS results.

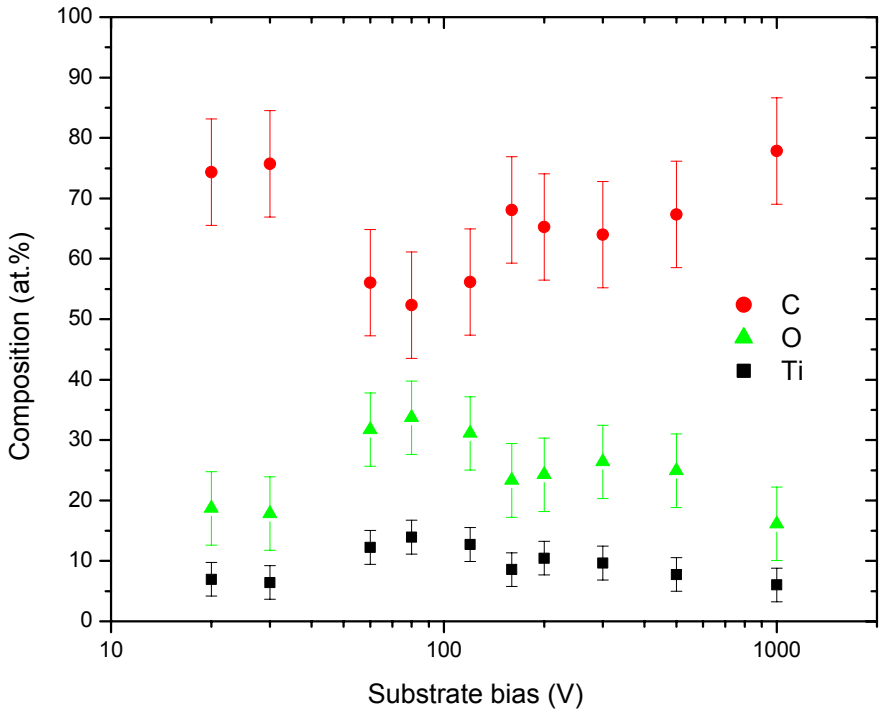

Figure 3.5 The film composition of a-C:Ti films deposited at different bias

To further investigate the self-sputtering effect, one series of a-C:Ti films was deposited at different ion energies from the 5 at.% Ti containing composite target. The film composition of a-C:Ti films deposited at different substrate bias was calculated by XPS and the results are shown in Figure 3.5. It is interesting to note that

the Ti composition increases with the substrate bias but decreases with further increasing the substrate bias. The a-C:Ti film deposited at –80 V has the highest Ti composition. This is explained in detail in Chapter 7.

3.2 Microstructure and Morphology

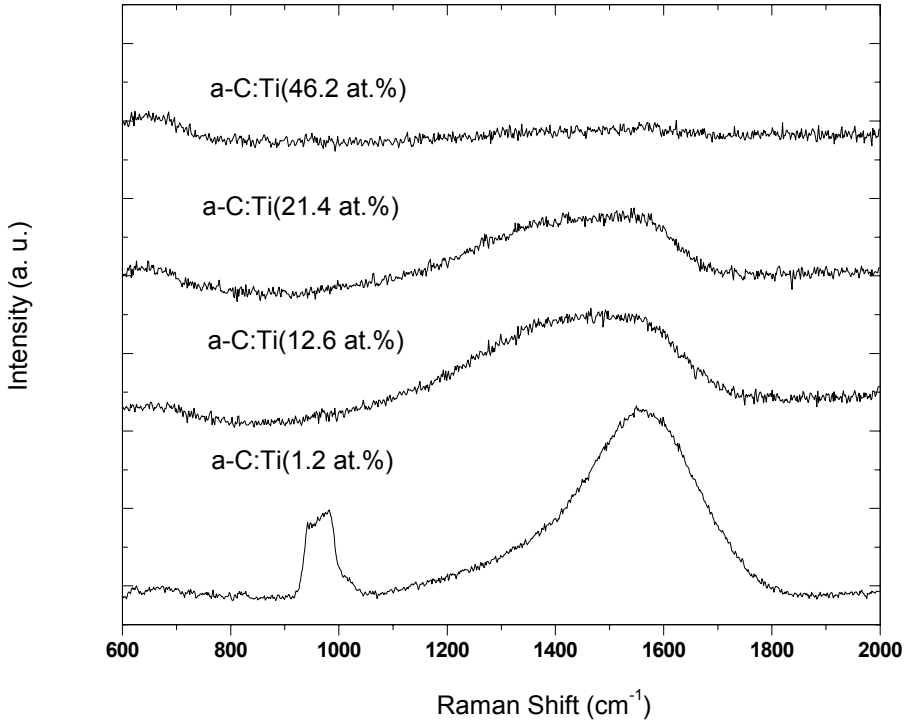

Figure 3.6 Raman Spectra of a-C:Ti films

The Raman spectra of a-C:Ti films deposited from different metal composition metal/carbon targets are shown in Figure 3.6. In the wavenumber region of 1100-1700 cm^{-1}, there is a broad asymmetric scattering band, which is a typical characteristic of ta-C films [38]. For the a-C:Ti (46.2 at.%) film, the amorphous carbon band has

become extremely weak, which implies that most of the carbon atoms in the film have formed chemical bond with Ti. On the Raman spectra, there is another broad peak in the wavenumber region 600-800 cm^{-1}, which is closely related to the formation of TiC in the film [48, 49].

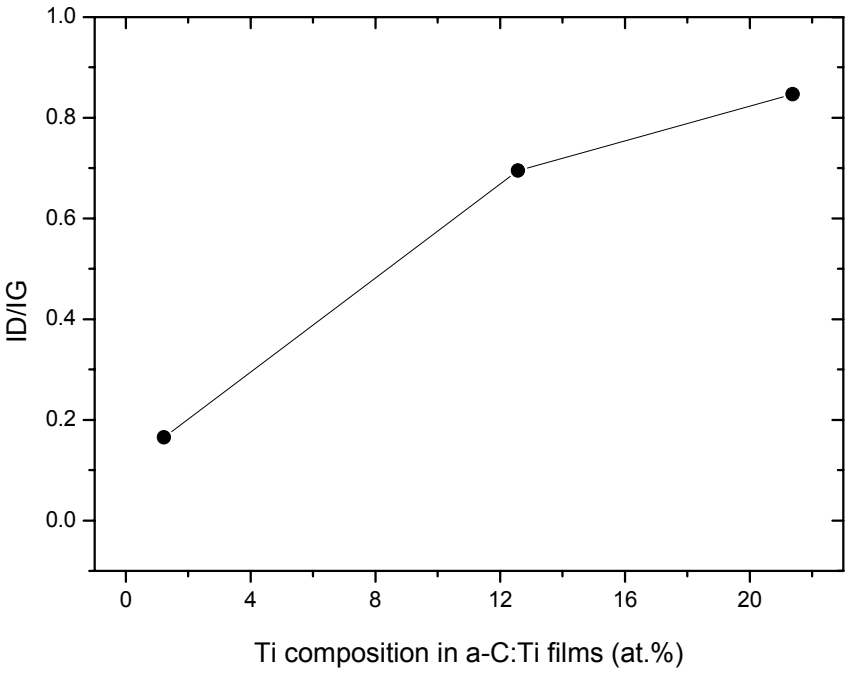

Figure 3.7 The I_D/I_G ratio of a-C:Ti films with different Ti composition

The Breit-Wigner-Fano (BWF) method was used to fit the above spectra. The I_D/I_G ratio is shown in Figure 3.7. The D peak is used for the fitting. The I_D/I_G ratio increases with the increase in Ti composition. This indicates the sp^2 cluster size increases with the increase in Ti composition.

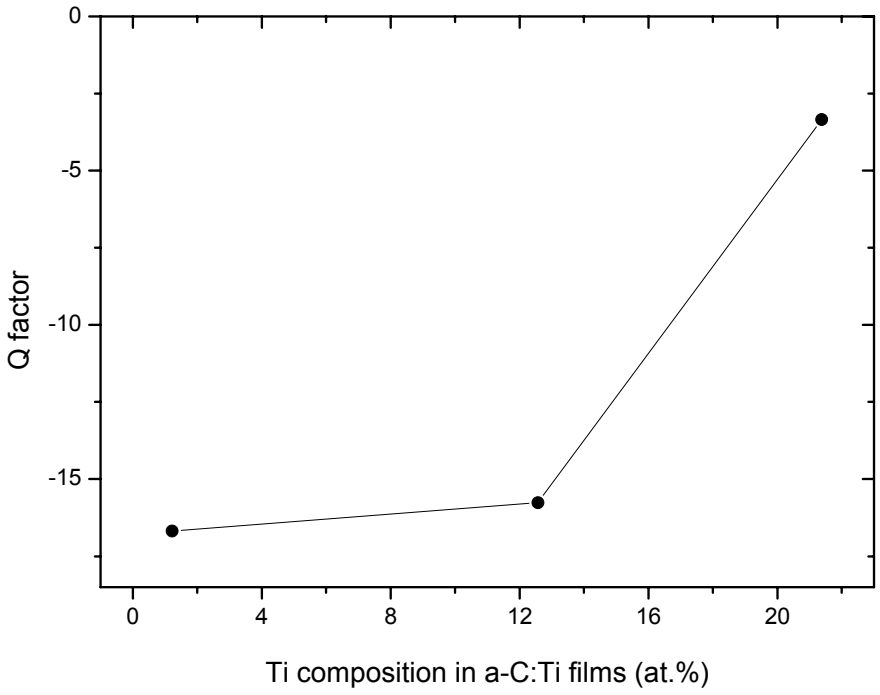

Figure 3.8 The Q factor of a-C:Ti films with different Ti composition

The Q factor is shown in Figure 3.8. It is observed that the Q factor decreases with the increase in Ti composition. This shows the sp^3 composition decreases. The film with more sp^3 composition is more "transparent" to the Raman signal from Si substrate. In Figure 3.6, the Si signal (2^{nd} order, ~ 920 cm^{-1}) from a-C:Ti (1.2 at.%) sample is more pronounced than that of a-C:Ti (12.4 at.%). This is a direct proof showing the a-C:Ti (1.2 at.%) has more sp^3 content. The mechanism of sp^3 formation is known as subplantation mechanism. The implanted C atom generates very high local stress and forces the neighboring C atoms to form sp^3 bond structure. When Ti atom is the neighbor of the implanted C atom, it will affect the formation of sp^3 structure because Ti will bond with its neighbor C.

The Raman spectra of a-C:Ti films deposited from different metal composition metal/carbon targets are shown in Figure 3.9. As discussed, the broad peak in the wavenumber region 600-800 cm^{-1} is closely related to the formation of Ti carbide in the film. The peak around 950 cm^{-1} corresponds to the second order vibration mode of the Si substrate. The Si signal increases with the increase in substrate bias to 120 V but decreases when further increasing the substrate bias. Generally, the more transparent the film is, the higher the sp^3 composition in the film [42]. Hence similar to the case for ta-C film, the a-C:Ti film has a maximum sp^3 composition at 120 V bias.

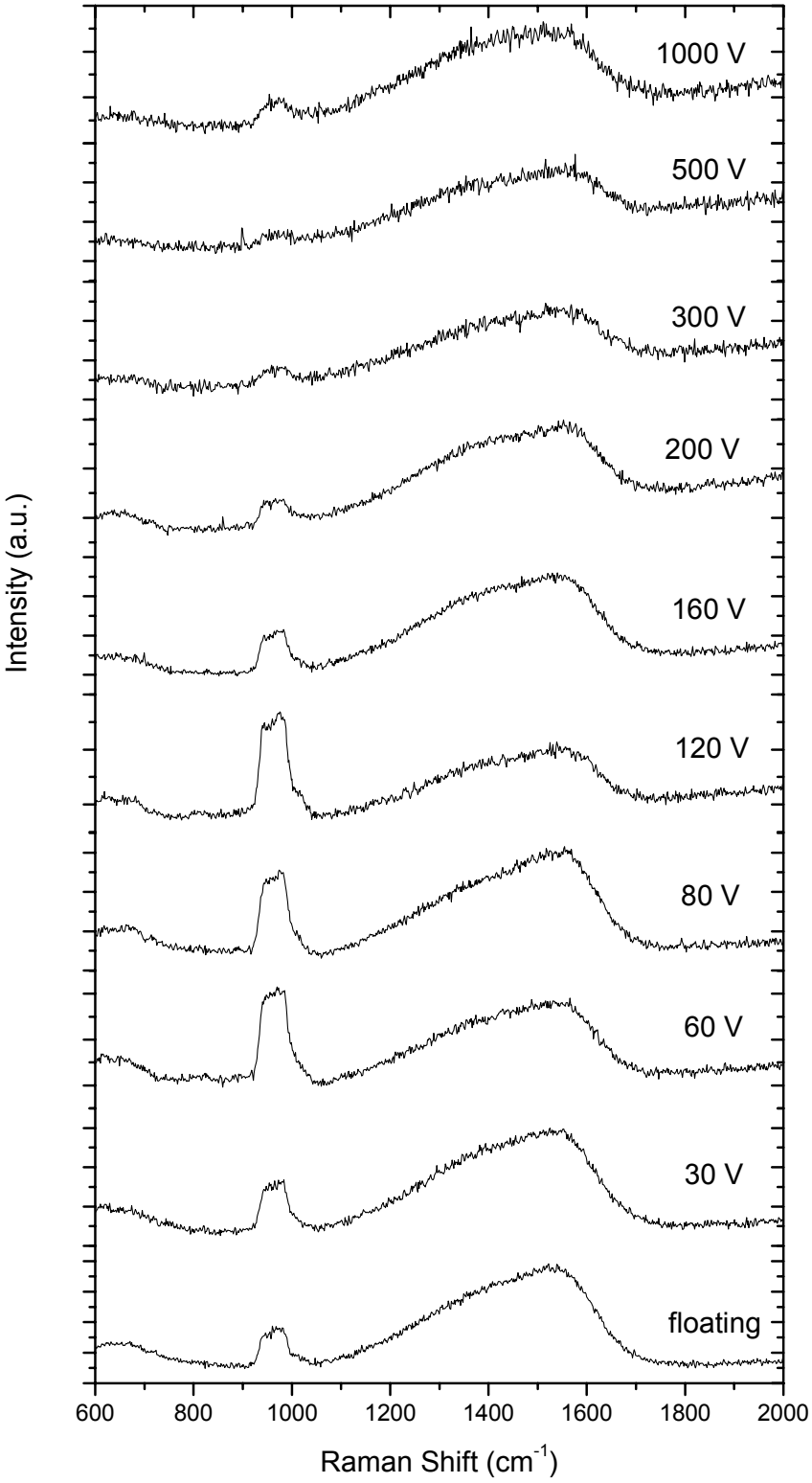

Figure 3.9 Raman spectra of a-C:Ti films deposited at different bias

The BWF method was used to fit the broad asymmetric scattering band in the wavenumber region of 1100-1700 cm^{-1}. Figure 3.10 shows the Q factor as a function of substrate bias. It shows a "V" shape and is very similar to that of the ta-C films deposited at different energy [42, 50]. This suggests the sp^3 composition of a-C:Ti films is richest at middle bias range (120 V in this case). This is consistent with the "transparence" of the a-C:Ti films to the Si signal. The reason may be the same for the pure carbon film. The low energy ions do not have sufficient energy to implant into the film and the ions with excessive energy generate thermal spike and cause the sp^3 bond to relax to an sp^2 structure.

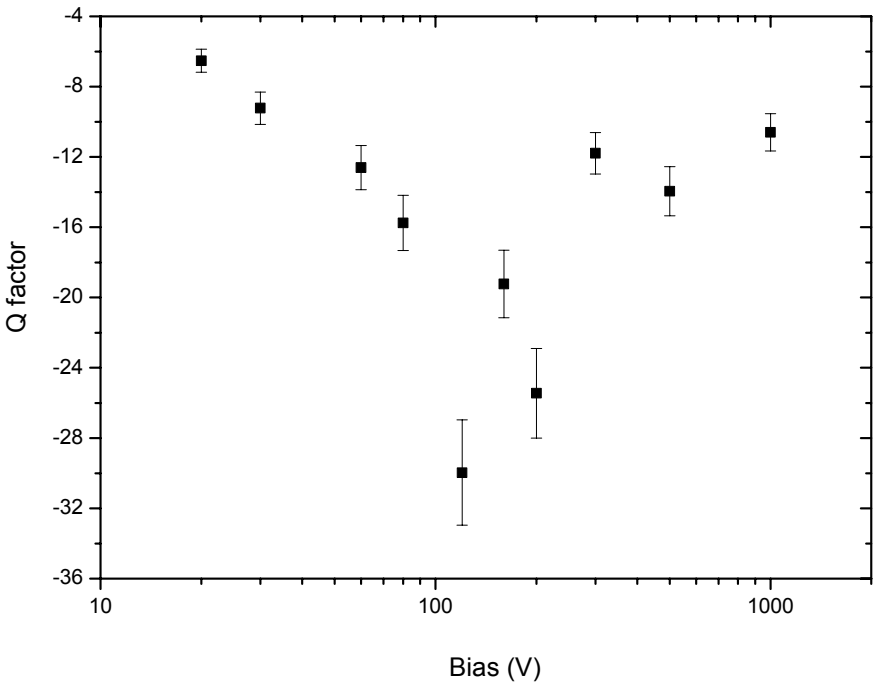

Figure 3.10 The Q factor of a-C:Ti films deposited at different bias

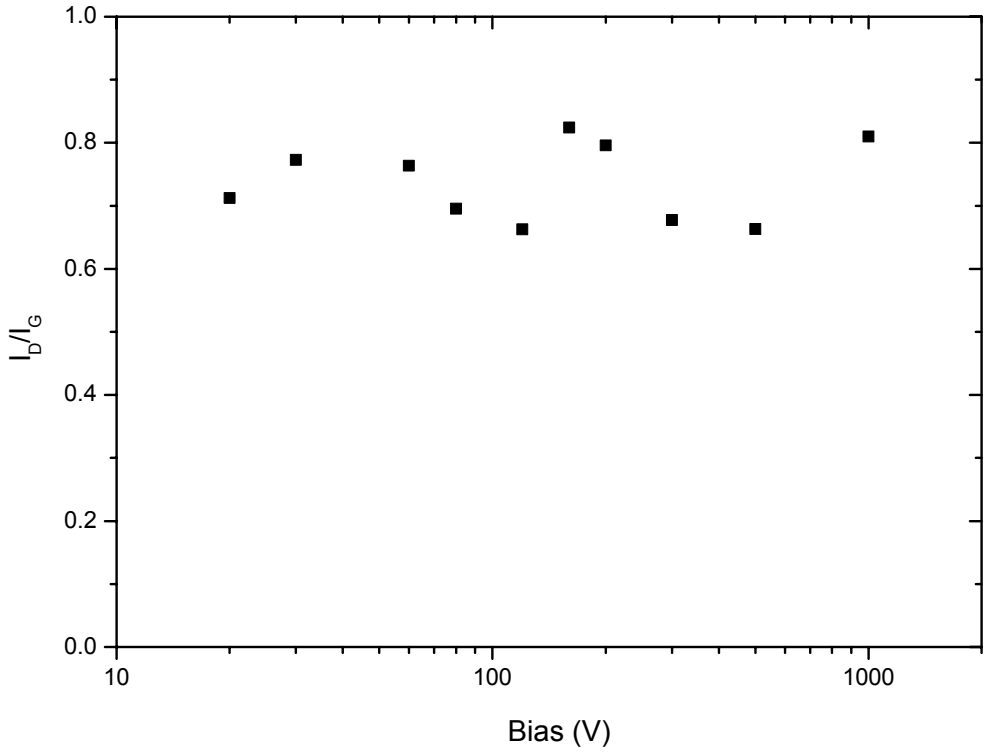

Figure 3.11 The I_D/I_G ratio of a-C:Ti films deposited at different bias

The I_D/I_G ratio is shown in Figure 3.11. The I_D/I_G ratio of a-C:Ti films remains almost constant (around 0.75). This indicates that the size of the sp^2 cluster size is still small and it is not sensitive to the substrate bias. The formation of TiC may be responsible for this.

The nanostructure of a-C:Ti films was studied by high resolution TEM (HRTEM). Figure 3.12 shows the TEM in-plane image of an a-C:Ti film deposited from a 5 at.% Ti composite target at – 80 V bias. It exhibits only a granular contrast, which is typical of the amorphous phase objects. No obvious Ti or TiC clusters are observed in the image. In some regions, it looks like there is a short-range low-degree of

disordered structure. Those structures could be the sp^2 clusters or chains. The size of such regions is smaller than 1 nm.

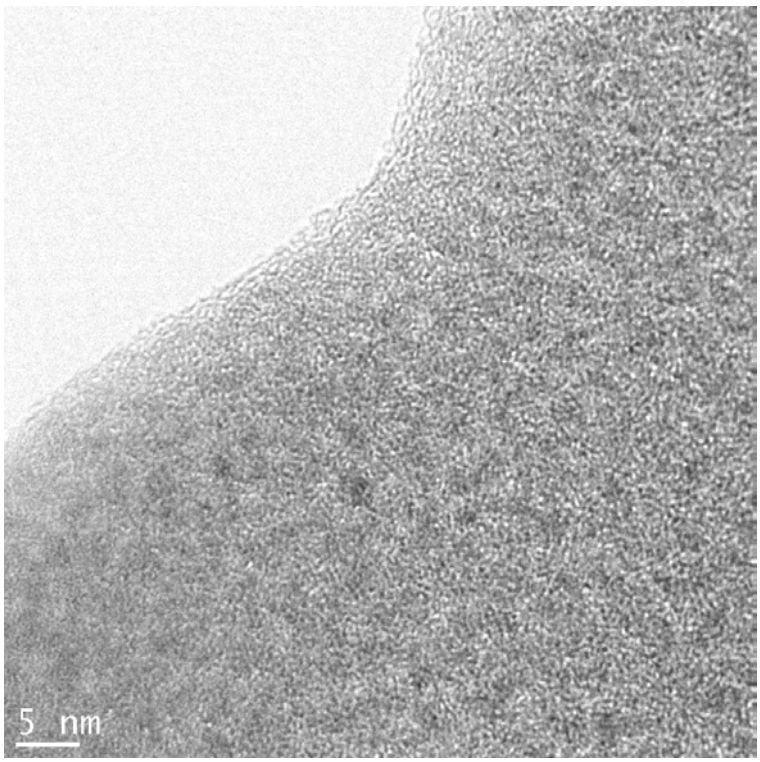

Figure 3.12 The High resolution TEM image of an a-C:Ti film

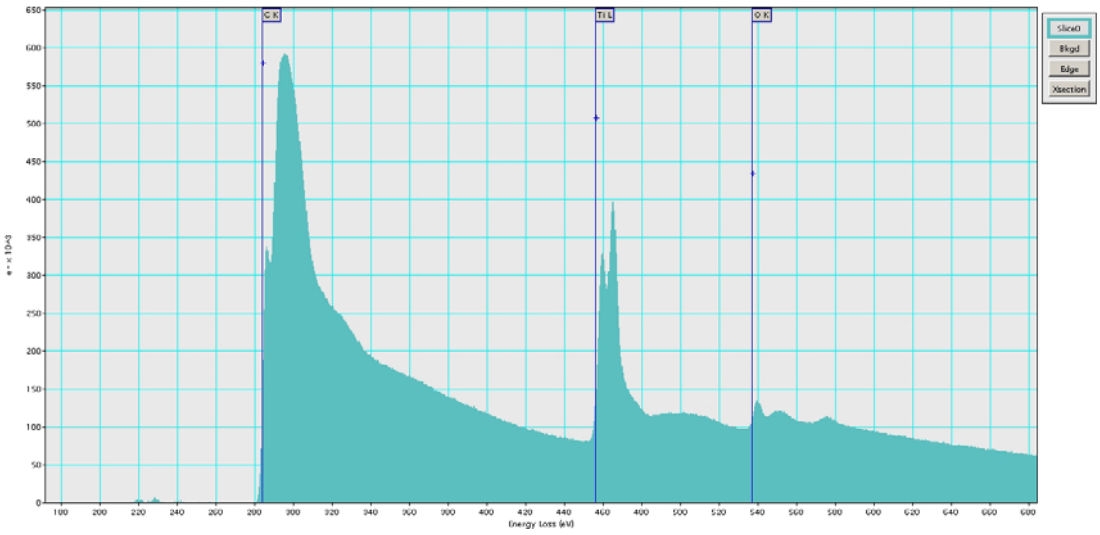

Figure 3.13 The electron energy loss spectrum of an a-C:Ti film

Chemical microanalysis of the a-C:Ti film was performed by EELS. The EELS shown in Figure 3.13 indicates the presence of C, Ti and small amounts of O in the film. Scanning elemental maps for each element were captured and are shown in Figure 3.14. All elements are atomically dispersed. Ti atoms dissolve uniformly within the carbon matrix.

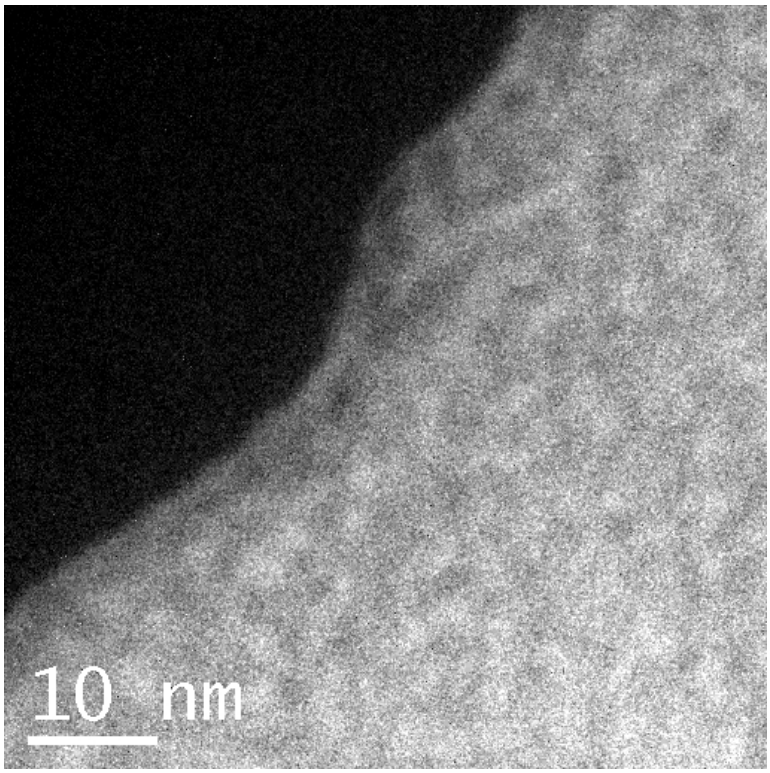

(a) C mapping

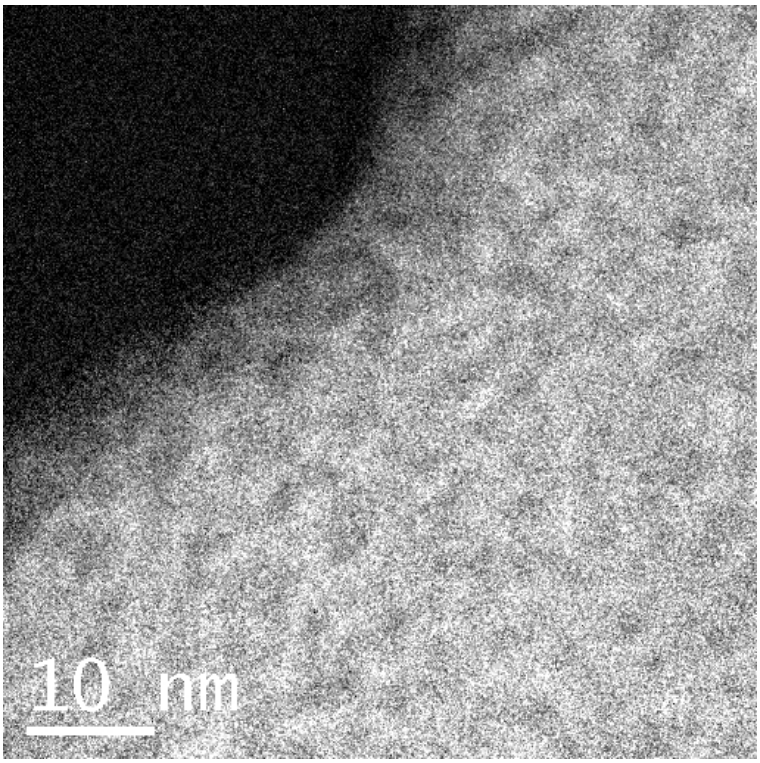

(b) Ti mapping

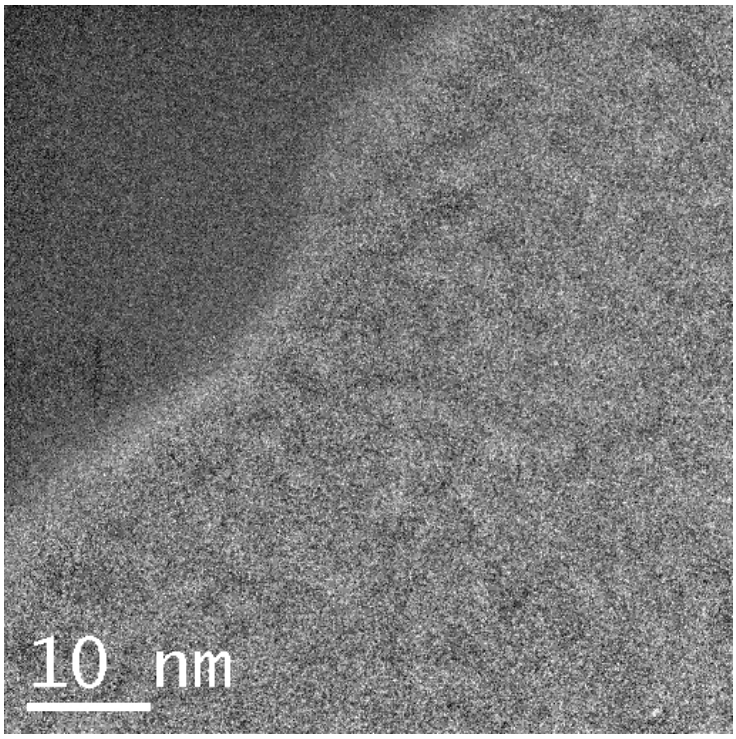

(c) O mapping

Figure 3.14 The C, Ti and O mappings of an a-C:Ti film

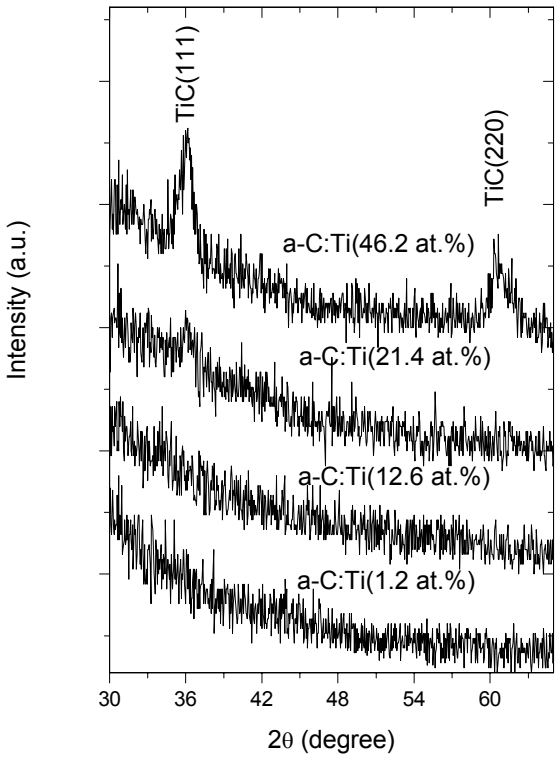

Figure 3.15 XRD spectra of a-C:Ti films with different Ti composition

The XRD patterns of the a-C:Ti films are shown in Figure 3.15. No crystalline phase is determined in the low Ti composition films. For the a-C:Ti (46.2 at.%) film, a cubic TiC crystalline phase is clearly observed.

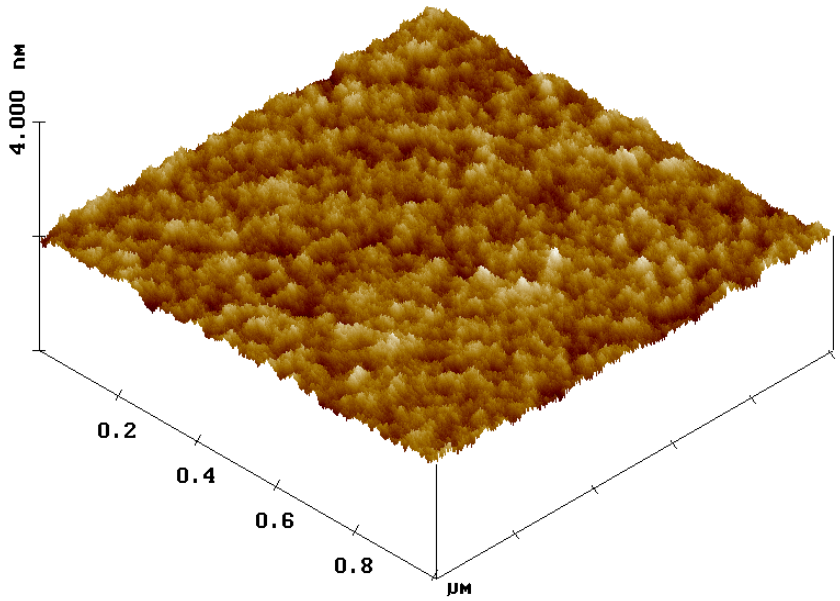

Figure 3.16 The typical AFM image of a-C:Ti film

A typical image of the a-C:Ti film deposited from a 5 at.% composite target at –80 V bias is shown in Figure 3.16. The surface rougness of a-C films increases with the incorporation of Ti. The typical RMS roughness of ta-C films is 0.06 – 0.08 nm. The roughness of a-C:Ti(1.2 at.%) is 0.09 nm. The roughnesses of a-C:Ti (12.6 at.%), a-C:Ti(21.4 at.%) and a-C:Ti(46.2 at.%) are 0.10 nm, 0.14 nm, and 0.21 nm respectively. The increase in roughness indicated the increase in sp^2 composition too [51]. However, due to their amorphous nature, these values are still very small.

3.3 Surface Energy

The contact angle of a ta-C film is around 77.6^{o} [52, 53]. Figure 3.17 and Figure 3.18 show the contact angle for water in contact with a-C:Ti films with different Ti composition and deposited at various bias, respectively. With Ti incorporation, the contact angle increases to 95^{o}. The contact angle for both a-C:Ti films with different Ti composition and a-C:Ti films deposited at various bias show relatively constant value. A typical snapshot of water droplet on an a-C:Ti film is shown in Figure 3.19.

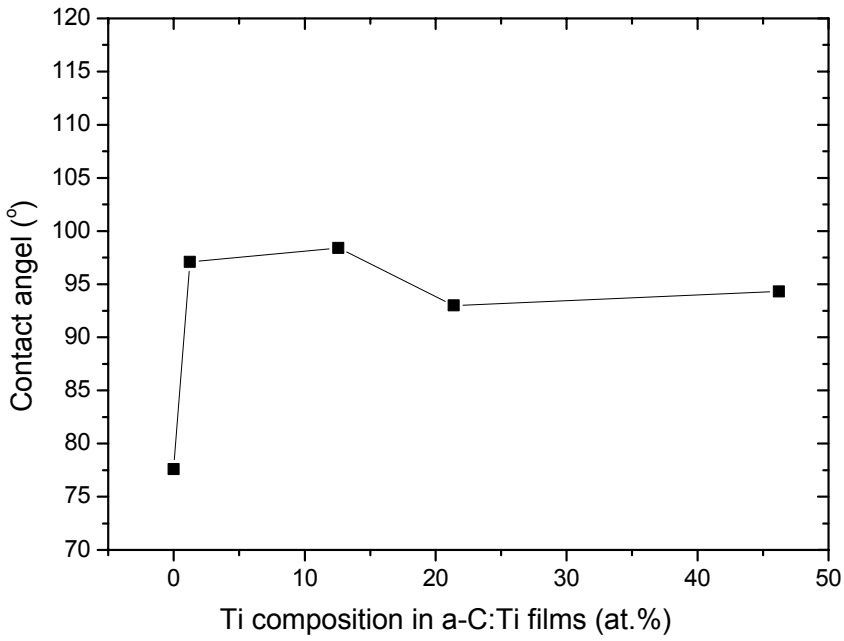

Figure 3.17 The contact angle between water and a-C:Ti with different Ti composition

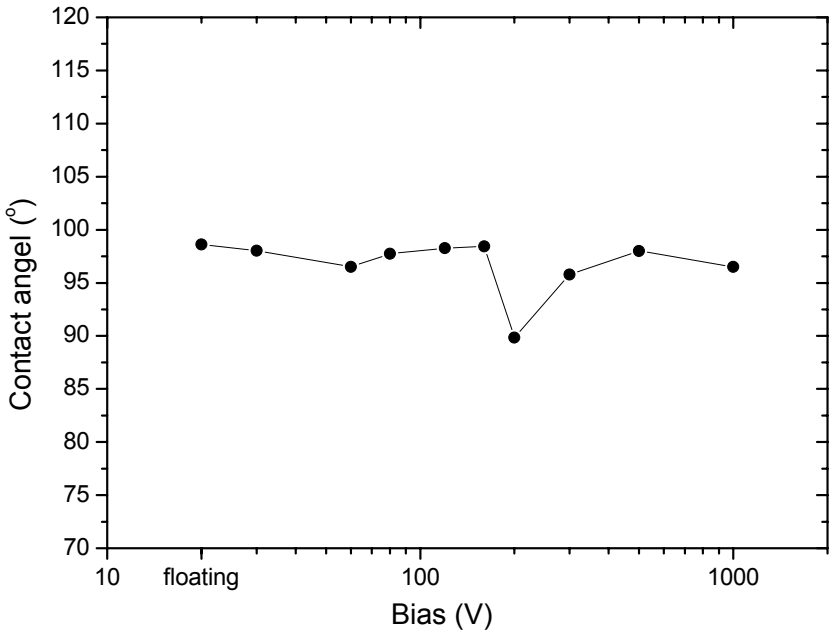

Figure 3.18 The contact angle between water and a-C:Ti as a function of bias

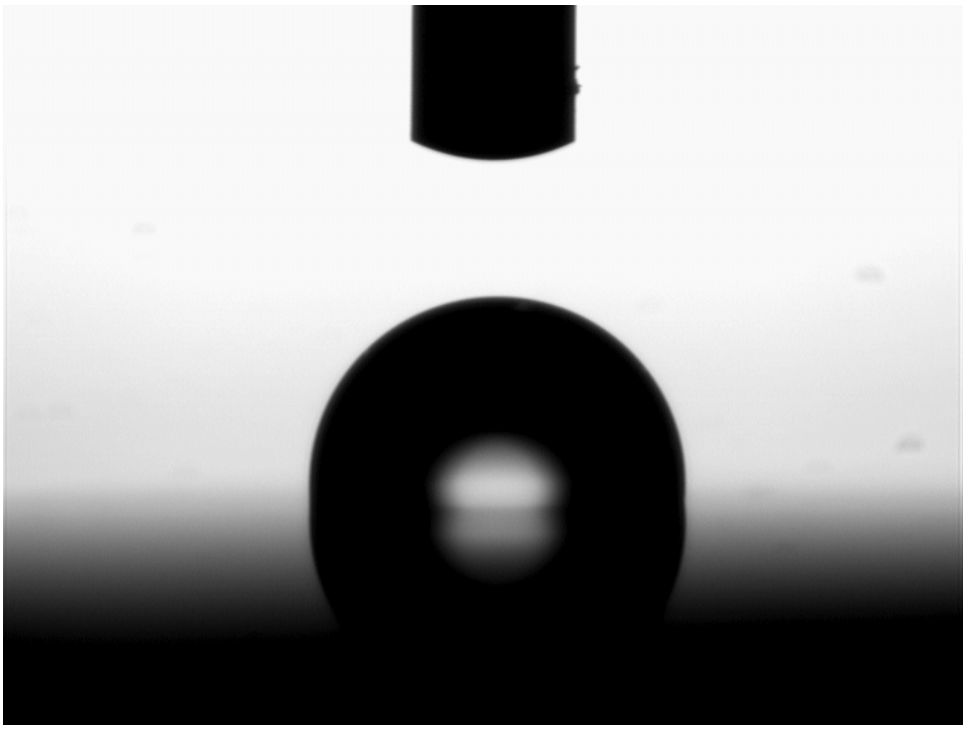

Figure 3.19 A typical image of an a-C:Ti film in contact with water

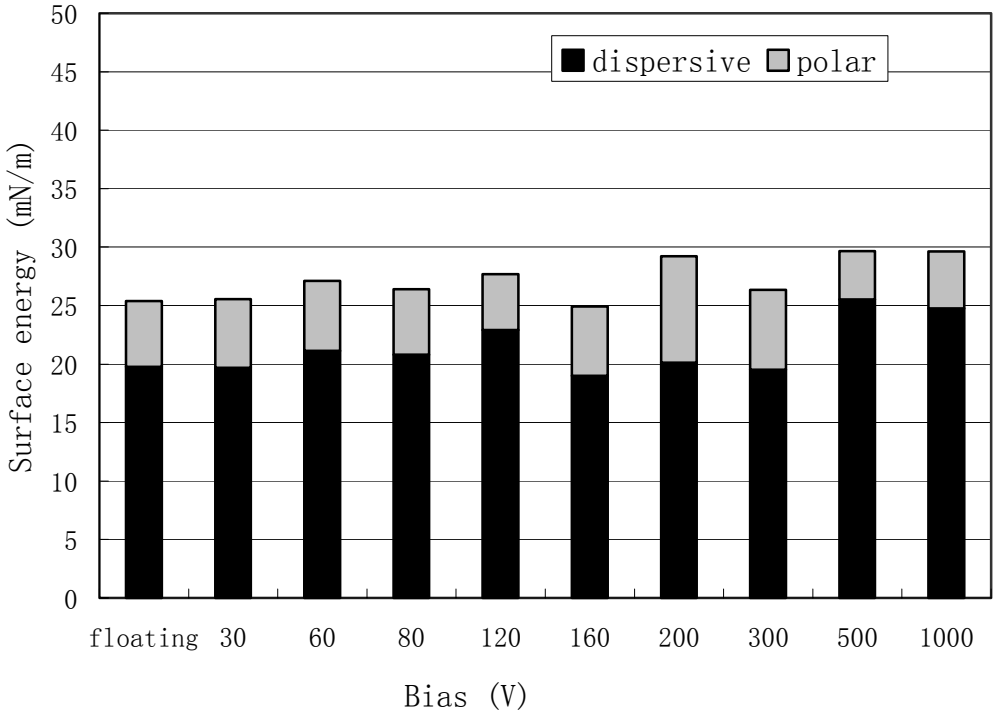

Figure 3.20 The surface energy of a-C:Ti films as a function of bias

The surface energy, including both the dispersive and polar components, was calculated using the harmonic-mean method. The dispersive and polar components and total surface energy of a-C:Ti films deposited at various bias are shown in Figure 3.20. Within experimental error, both the dispersive and polar components of a-C:Ti films are independent of the bias. It is seen that the polar component of the a-C:Ti films is as low as 5.86 mN/m. The small polar component contributes to the low surface energy. It is well known that surface energy is sensitive to the surface morphology and chemical composition. Therefore, the effect of roughness and surface composition on the surface energy will be discussed.

According to Neumann [54], the influence of the surface roughness on the contact angle is very important. A model similar to that for heterogeneous solid surface can be developed to account for surface irregularities and is given by Wenzel's equation:

$$r(\gamma_{sv} - \gamma_{sl}) = \gamma_{lv} \cos\theta_w \quad \textbf{(3.1)}$$

where r is a roughness factor, defined as the ratio of the real and apparent surface areas, and θ_w is the contact angle for a rough surface. This clearly shows that the smoother the contact surface is, the smaller the contact angle is. The a-C:Ti film deposited by the FCVA technique has a very smooth surface. The roughness factor is approximately equal to 1 and in this case the effect of roughness on contact angle is negligible.

The surface energy arises from the imbalance of the force between atoms or molecules inside and interface. Several types of van der Waals interactions contribute to the surface energy. In particular, the polar component results from three different intermolecular forces due to permanent and induced dipoles as well as hydrogen bonding, whereas the dispersive component of the surface energy is due to instantaneous dipole moments. As discussed in the XPS study, the Ti atoms form Ti-O bonds. The formation of Ti-O electrovalent bond makes the electron of the Ti localized [55]. Thus, the induced dipole decreases and polar component of surface energy decreases.

3.4 Reversible Wettability of a-C:Ti Films by UV Irradiation

It have been reported that ultraviolet (UV) illumination makes the originally hydrophobic TiO_2 film surface hydrophilic [56, 57, 58, 59]. Storage in ambience reconverts the surface back to hydrophobic. Several commercial products (e.g. anti-fogging glass and self-cleaning construction materials) have been produced on the basis of this phenomenon. Since the Ti-O bond plays an important role on the surface energy of a-C:Ti films, it is of great interest to investigate the UV treatment on a-C:Ti films. A 244 nm laser was used as the UV source. The laser was focused on the sample surface through an optical microscope. The irradiation area was about 1 cm by 1 cm. In addition, the laser power was fixed at 10 mW. The a-C:Ti films were irradiated for 100 mins. After irradiation, the samples were kept in ambience and the contact angle was measured at different time intervals. As shown in Figure 3.21, the a-C:Ti film becomes hydrophilic after UV irradiation and reconverts to hydrophobic when they are kept in ambience.

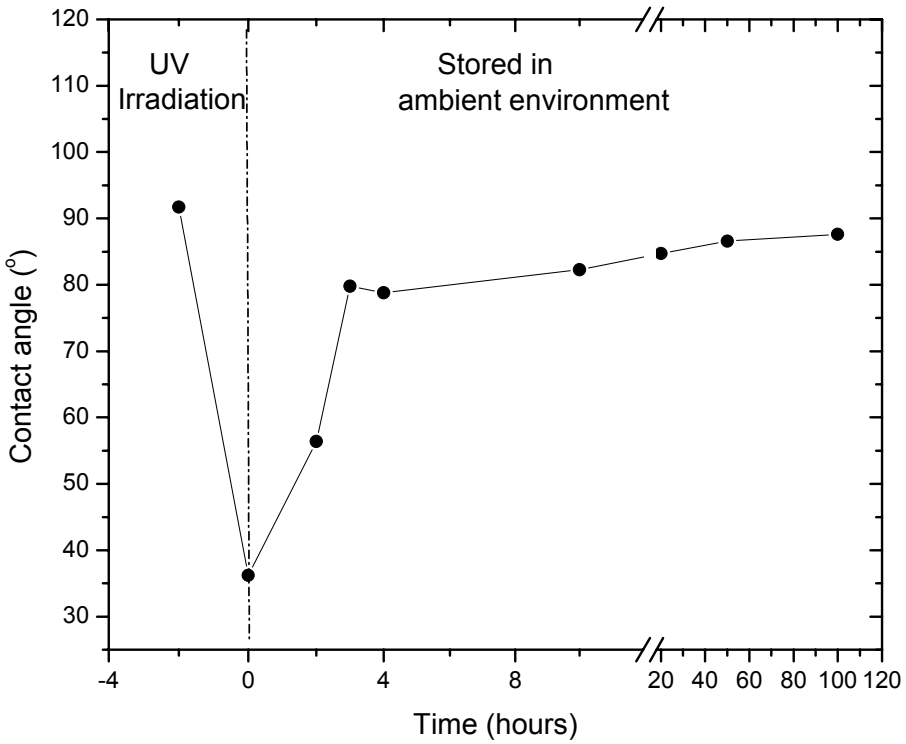

Figure 3.21 The contact angle variation of a-C:Ti films in ambience post UV irradiation

It has been reported that the hydrophilic surface of TiO_2 films after UV irradiation is caused by absorption of the $O\text{-}H^-$ group at the surface. Crystalline TiO_2 is a well-known photosensitive semiconductor with band gap ~3.0 eV. Such band gap illumination generates electron-hole pairs. Electrons and holes can either recombine or move to the surface to react with the species adsorbed on the surface, which is known to be the basis of photocatalysis. Conversely, some of the holes react with the oxygen within the TiO_2 lattice resulting in the formation of surface oxygen vacancies. At the same time, some of the electrons react with lattice Ti^{4+} and Ti^{3+} defective sites

(surface trapped electron) are formed. This process is expressed using the following equations:

$$TiO_2 + 2h\nu \rightarrow 2h^+ + 2e^- \quad (3.2)$$

$$O^{2-} + h^+ \rightarrow O_I^- \text{ (surface trapped hole)} \quad (3.3)$$

$$O_I^- + h^+ \rightarrow 1/2O_2 + \square \text{ (oxygen vacancy)} \quad (3.4)$$

$$Ti^{4+} + e^- \rightarrow Ti_S^{3+} \text{ (surface trapped electron)} \quad (3.5)$$

After the generation of surface vacancy by photo irradiation, the oxygen and water (from moisture) can compete to dissociatively adsorb on it. Since the $O\text{-}H^-$ group absorption has been confirmed by some group [56], it seems that under UV irradiation the absorption of $O\text{-}H^-$ group is more favorable than the oxygen. This hydroxyl groups contribute to a hydrophilic surface. However, the absorption of hydroxyl groups destroys the electronic structure and geometry of the surface, therefore the surface is in a metastable state. After the UV irradiation, the oxygen from the ambient tends to replace the absorbed hydroxyl groups. The surface reverses to a hydrophobic one.

Snapshots of a water droplet on an a-C:Ti film at different post UV irradiation time intervals are shown in Figure 3.22. After UV irradiation, the contact angle decreases to 36.2^o. When the film is stored in air, the contact angle increases to 87.6^o. Nevertheless, this angle is still smaller than the original 95^o.

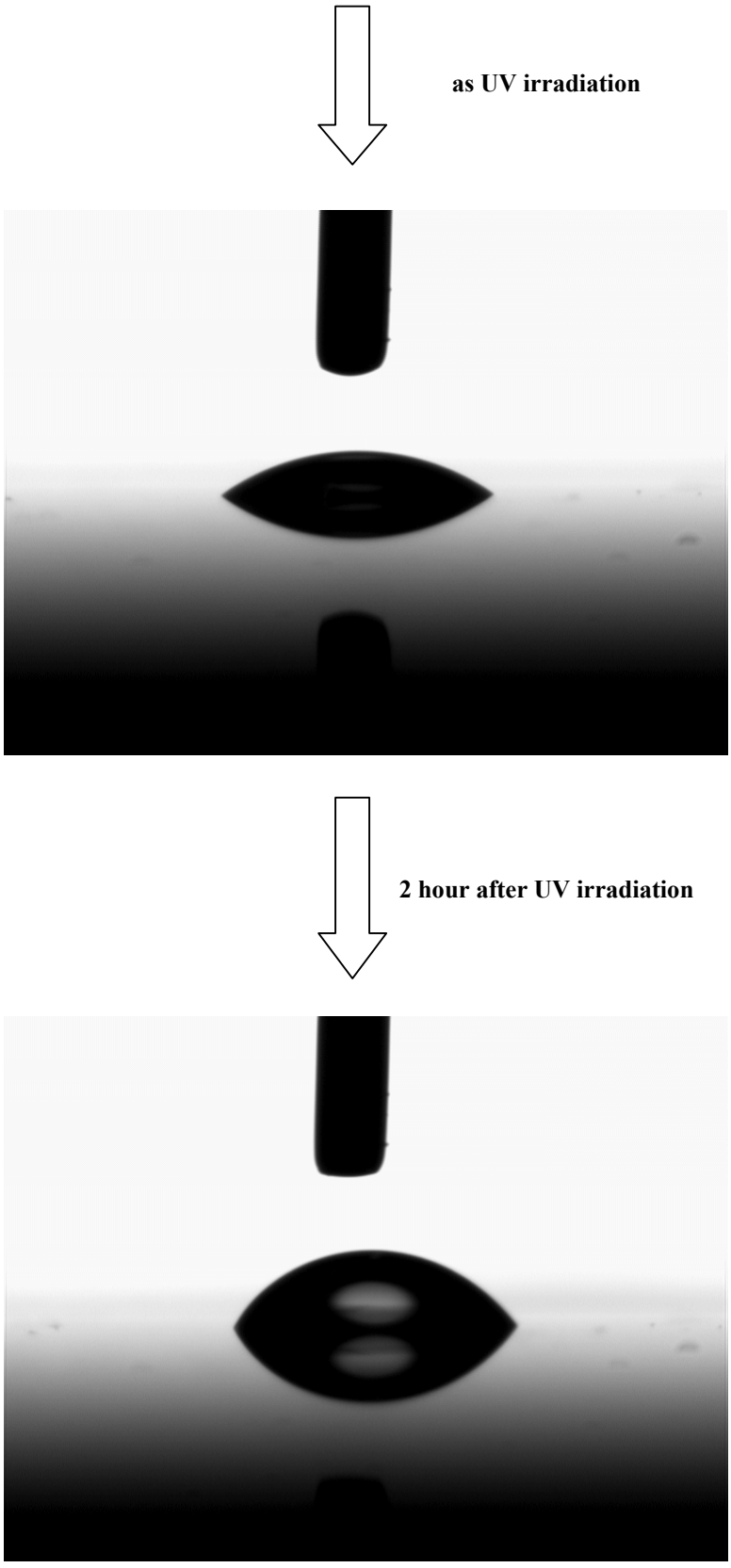

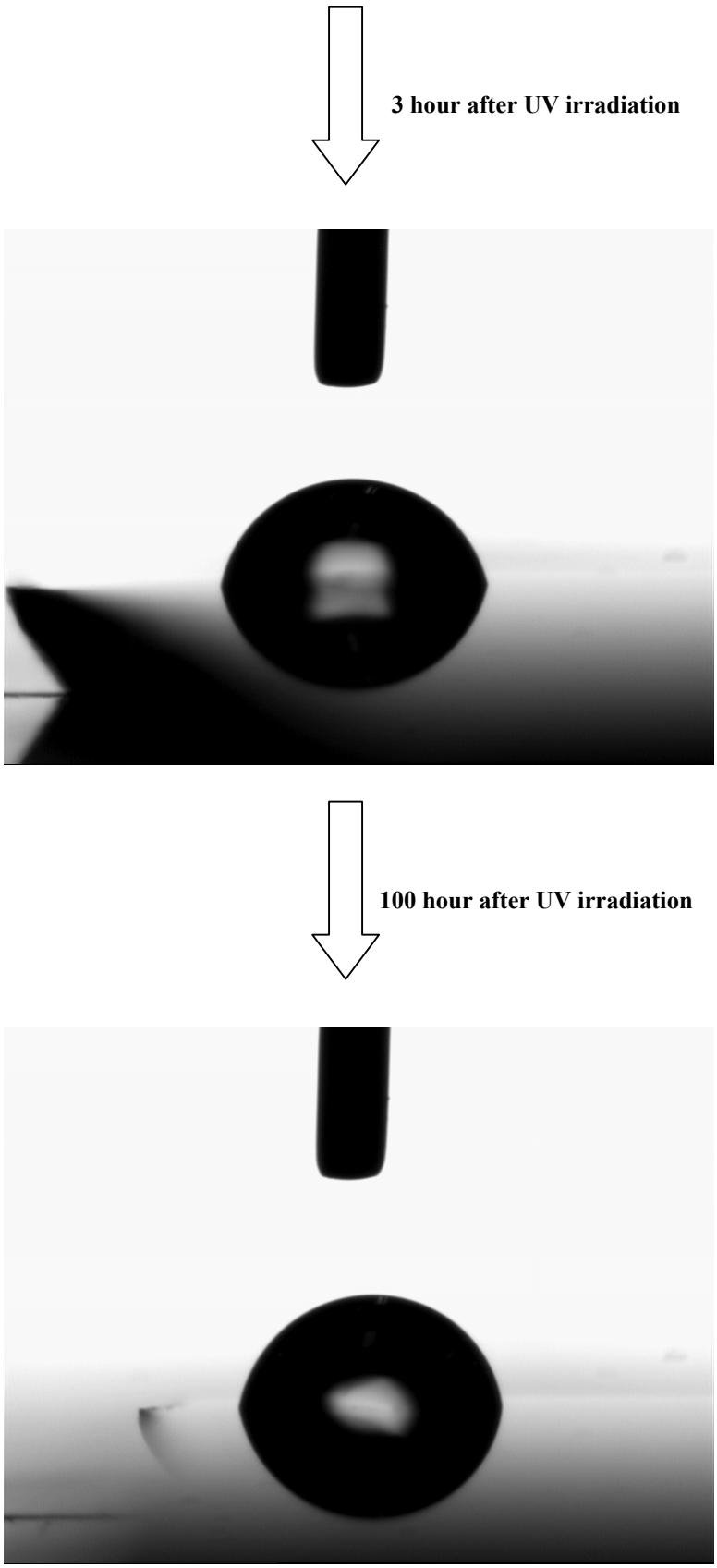

Figure 3.22 Snapshots of water droplet on a-C:Ti films at different post UV irradiation time

3.5 Mechanical Properties

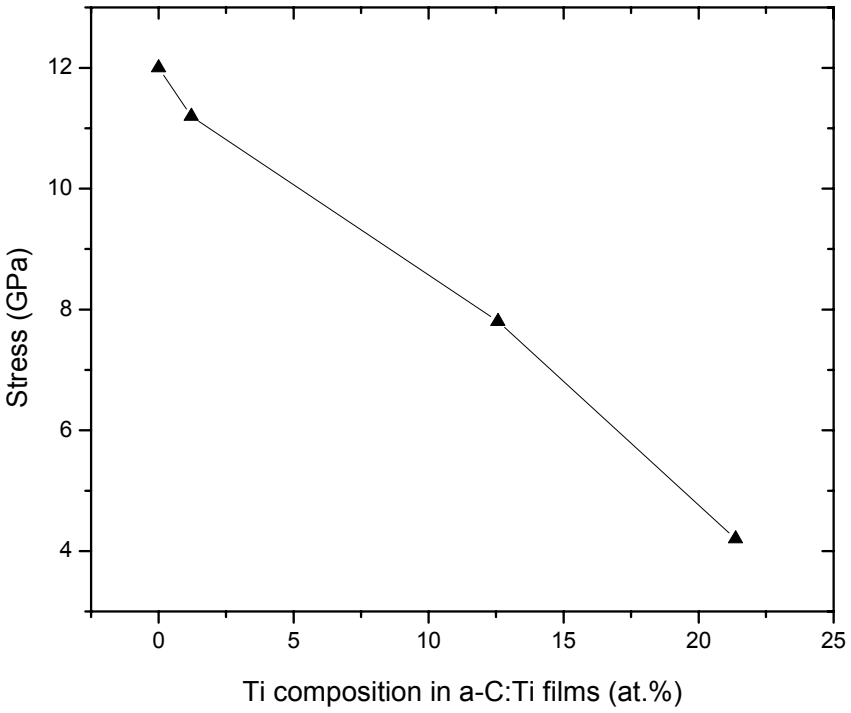

Figure 3.23 The stress of a-C:Ti films with different Ti composition

Figure 3.23 shows the stress of a-C:Ti films as a function of the metal composition in the films. It is clear that incorporating Ti into films reduces the compressive stress. The typical stress for a-C films deposited by the FCVA technique is 12 GPa. The stress drops from 11.3 GPa to 4.2 GPa while the Ti composition in the films increases from 1.2 to 21.4 at.%. The internal stress of a-C films mainly results from the subplantation. As discussed in previous chapter, the incorporation of Ti results in the decrease of sp^3 composition. Sullivan [60] noted that while the atomic volume of sp^2 sites exceeded that of sp^3 sites, their in-plane size is smaller, due to the shorter bond length. Thus the formation of sp^2 sites with their σ plane aligned in the plane of

compression can relieve biaxial compressive stress. Ferrari [61] proposed that only a small increase in sp^2 fraction is needed to account for the stress releasing. Thus a-C:Ti films with high Ti composition have a low stress.

Figure 3.24 and Figure 3.25 shows that incorporation of Ti into the films decreases the hardness and Young's modulus of the films. The relative decrease in hardness and Young's modulus is similar to the reduction of the compressive stress. The typical hardness of an a-C film is 44 GPa. The hardness drops from 36 GPa to 24 GPa with the Ti composition increases from 1.2 to 21.4 at.%. However, it is worth noting that the hardness and Young's modulus are still high. In comparison, the typical hardness for a-C:H films is only 10 GPa [62].

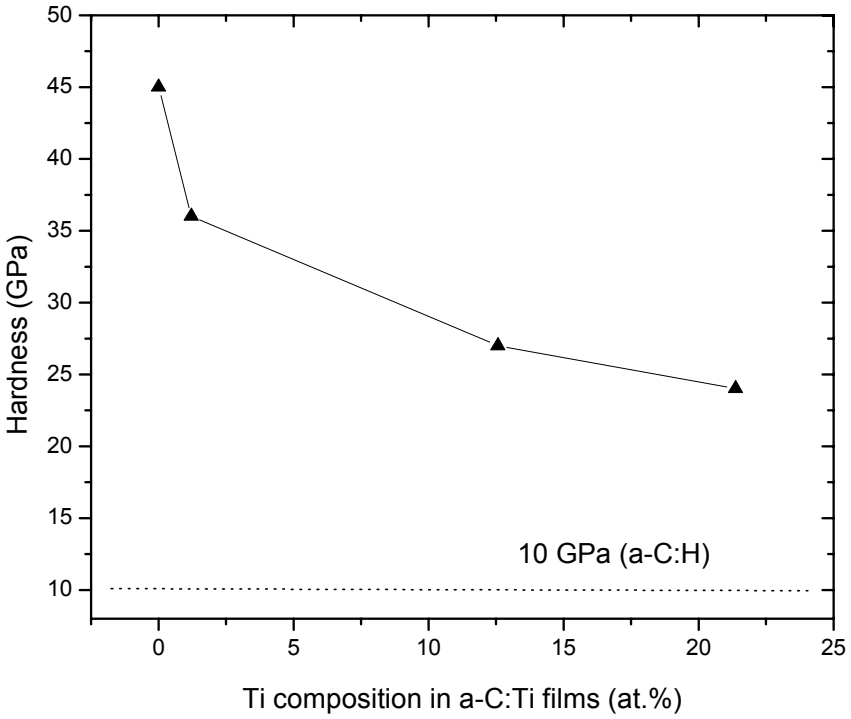

Figure 3.24 The hardness of a-C:Ti films with different Ti composition

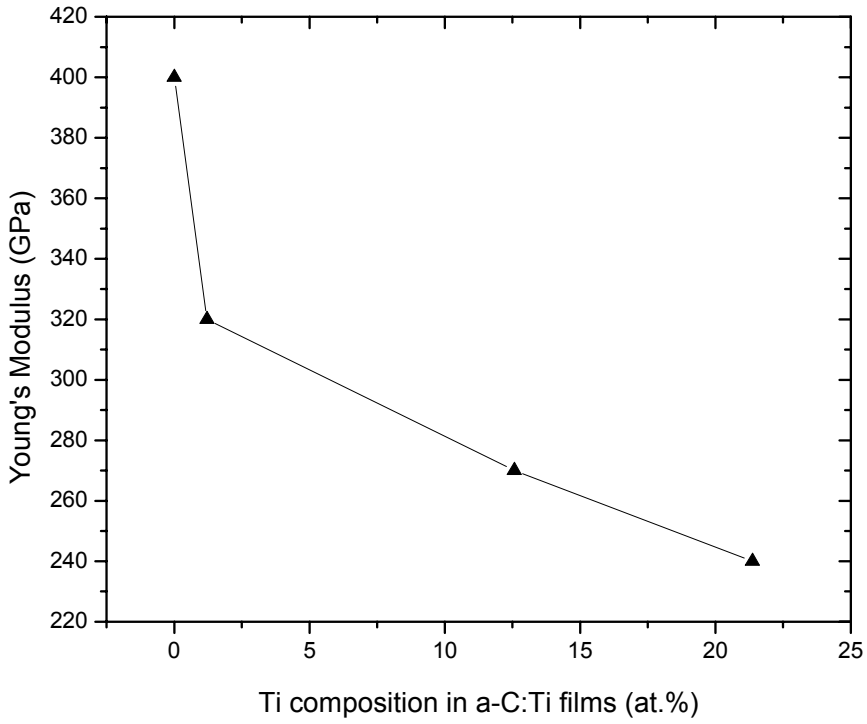

Figure 3.25 The Young's modulus of a-C:Ti with different Ti composition

As proposed by Robertson [63], the hardness and Young's modulus of diamond-like carbon films are mainly determined by the sp^3 composition, which results in a tight three-dimensional diamond-like carbon network. The previous results [50] from our research group also indicate that the hardness and Young's modulus values are strongly correlated with sp^3 fraction in ta-C films. The increase in sp^2 clusters in a-C:Ti films is the main reason for the decrease in hardness and Young's modulus.

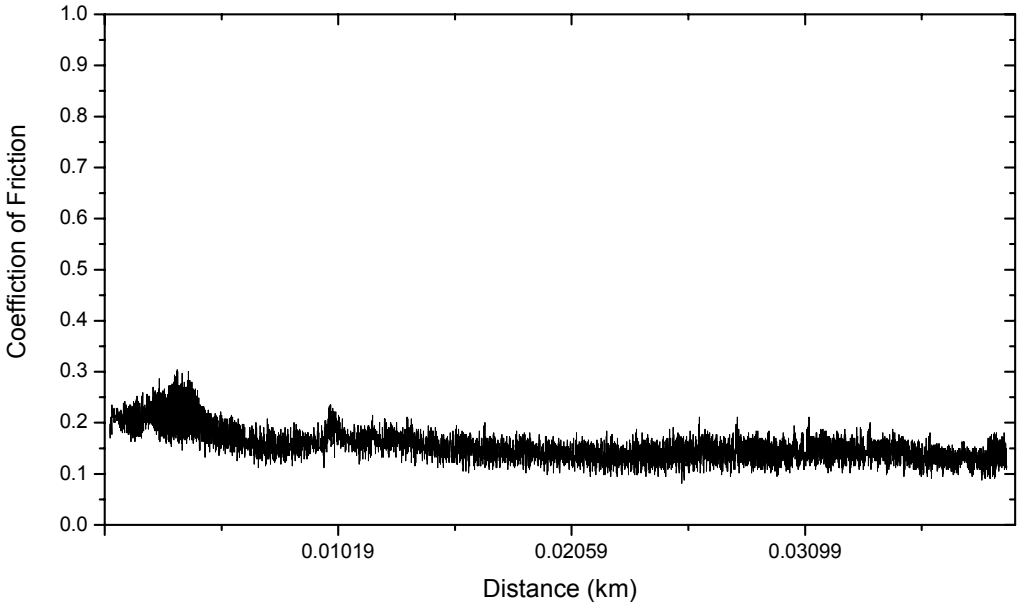

Figure 3.26 Coefficion of friction of a-C:Ti film

As shown in Figure 3.26, the coefficient of friction of an a-C:Ti (12.6 at.%) film is measured using the pin-on-disk method with a tribometer. The load is 1 N and the rotating speed is 5 cm/s. The radius of the track is 5 mm. The steady coefficient of friction is around 0.14.

3.6 Electrical and Electrochemical Properties

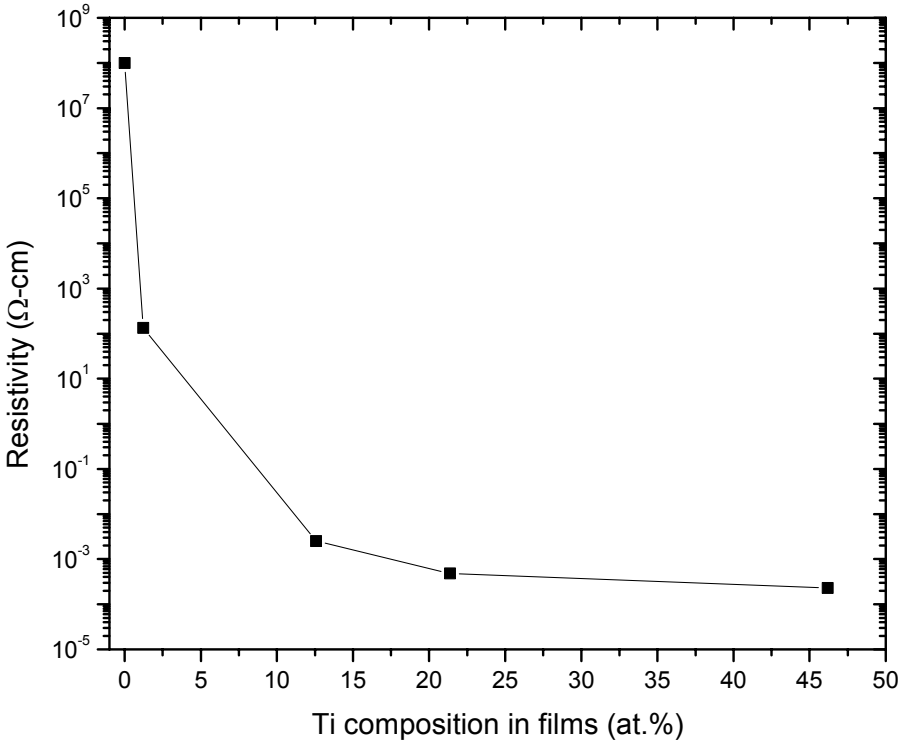

Figure 3.27 The resistivity of a-C:Ti films with different Ti composition

The electrical resistivity of a-C:Ti films with different Ti composition in the films is shown in Figure 3.27. By incorporating Ti into the film, the electrical resistivity changes significantly from its initial value of 10^8 Ω-cm. It decreases by 12 orders of magnitude. Within a-C films, the sp^2 clusters introduce states at or near the Fermi level, depending on their size and on whether they are odd or even numbered. Hopping between clusters has been proposed as a possible mechanism for room-temperature conduction. Recent calculations show that the sp^2 states remains localized even up to 80% sp^2 bonding, well above the percolation threshold. This localization of

states has been attributed to dihedral bond angle disorder, and such localized states result in hopping with low activation energy at room temperature and bandtail conduction at higher temperature. As discussed, with the increase in Ti composition, the sp^2 composition in the films increases, resulting in the decrease of the resistivity of the films. Another factor is that Ti-C bonding is essentially metallic and titanium carbide is a conducting ceramic material with an electrical resistivity as low as 60 × 10^{-6} Ω-cm [31]. A continuous conduction channel may form through TiC phase and sp^2 sites in the films when Ti composition is high. As a result, the a-C:Ti film with high Ti composition has a very low electrical resistivity.

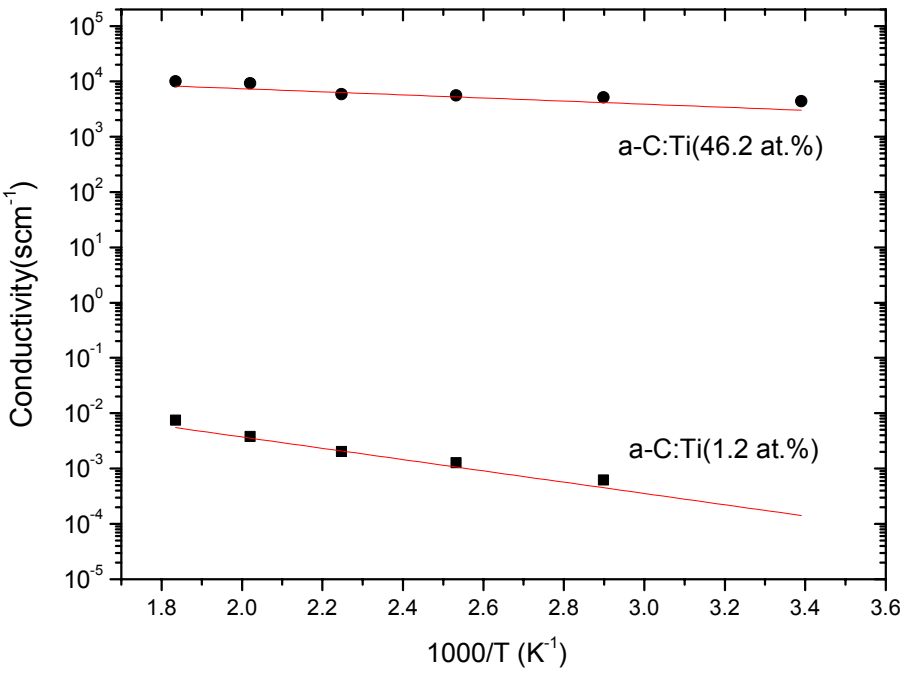

Figure 3.28 The conductivity of a-C:Ti measured as a function of temperature

To further understand the conduction mechanism the conductivity of the two a-C:Ti samples measured from room temperature to 272°C, shown in Figure 3.28. A much

steeper increase in the conductivity with temperature is clearly observed for a-C:Ti (1.2 at.%). A simplest Arrhenius relationship, $\sigma=\sigma_0 exp(-Ea/kT)$, is used to study the conductivity. In which, σ_0 is a temperature independent factor and Ea is the activation energy. Reasonable fits are obtained for the samples over the temperature range studied. The activation energy of a-C:Ti (1.2 at.%) is 0.134 eV and the activation energy of a-C:Ti (46.2 at.%) is 0.0367 eV.

As discussed, for the low Ti composition sample, the hopping of electrons between sp^2 clusters is the dominated conduction mechanism and a continuous conduction channel maybe formed in the high Ti composition sample. Therefore the thermal activated process of a-C:Ti (1.2 at.%) is more pronounced than a-C:Ti (46.2 at.%). The a-C:Ti (46.2 at.%) is more metallic-like.

The low background noise and wide electrochemical window offered by diamond makes it one of most ideal electrode materials for electrochemical analysis [64, 65, 66]. However, the high difficulty and cost of making low resistance diamond are obstacles for its electrochemical application. The a-C:Ti films show a low electrical resistance and have a “Diamond-Like” structure. Therefore it is interesting to investigate the electrochemical behavior of a-C:Ti films.

Electrochemical measurements were made with autolab electrochemical instruments. Cyclic voltammetry (CV) and electrochemical impedance spectroscopy (EIS) were used to study the electrochemical stability and gas evolution reactions in acidic solutions.

The electrochemical cell setup is shown in Figure 3.29. A simple three electrodes, including a working electrode (WE), a platinum plate counter electrode (CE), and a saturated calomel reference electrode (SCE), and a single compartment electrochemical cell were used. A 5 mm diameter rubber o-ring was used to seal the sample. The copper plate was in contact with the substrate.

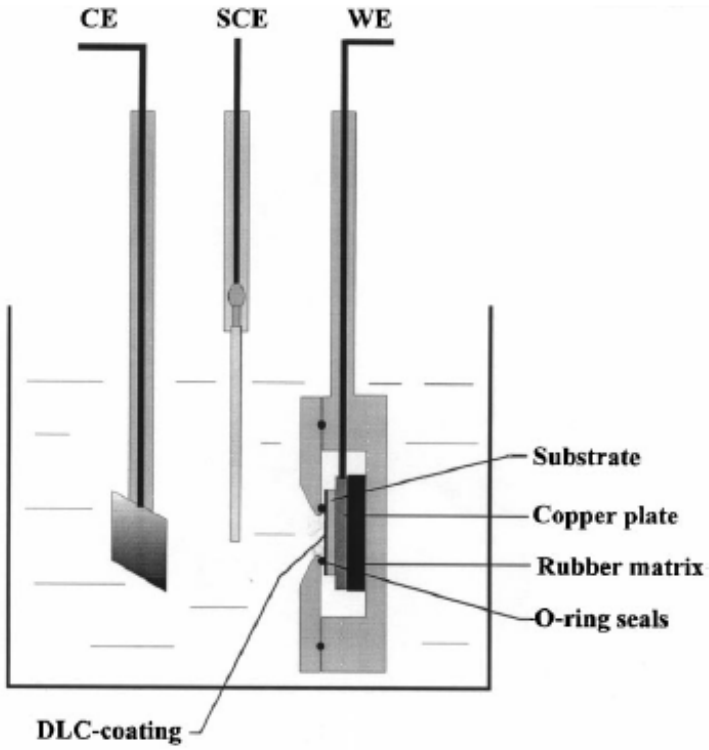

Figure 3.29 The electrochemical cell setup diagram

Cyclic Voltammetry (CV) was used to study the stability of a-C:Ti films with respect to electrochemical oxidation. The experiments were carried out in the 1 M H_2SO_4 acid solution with electrode potential cycling between –500 and 2000 mV vs SCE at room temperature. The scan rate was 100 mV/s.

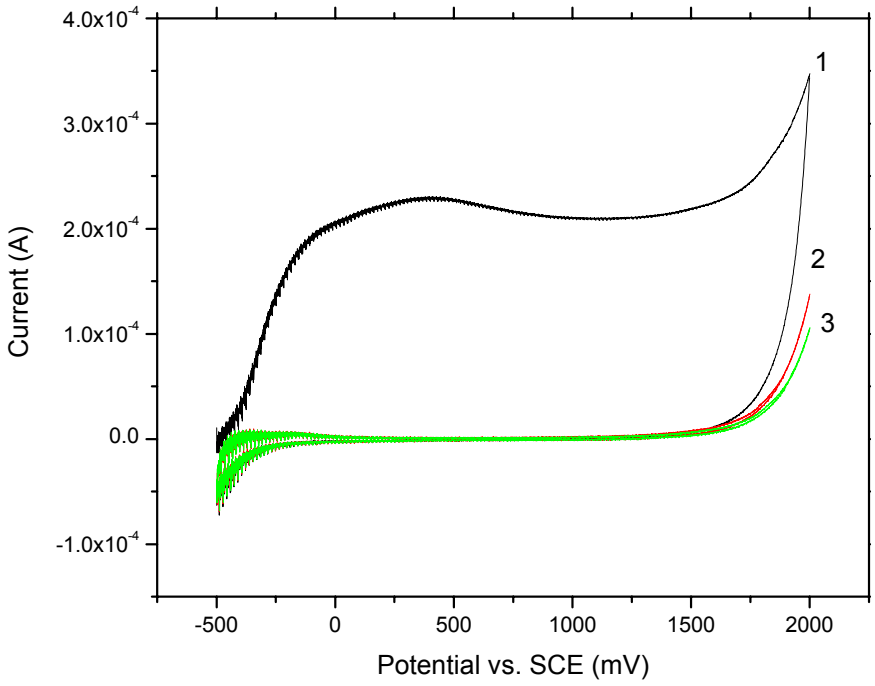

Figure 3.30 Cyclic voltammograms of a Ti plate in H_2SO_4

The multiple cyclic voltammograms of a pure Ti plate are shown in Figure 3.30. During the forward sweep of the first CV cycle in the Ti plate, a large current peak is observed at a potential of -300 mV. This is attributed to the oxidization of the Ti plate. On its reverse sweep, no feature is observed from 2000mV to -250 mV. Beyond a potential of –250 mV, a small current due to hydrogen evolution is observed. Unlike that of the forward sweep of the first cycle, the second and third cycle do not show obvious peak current. This indicates that the oxidization of Ti is non-reversible.

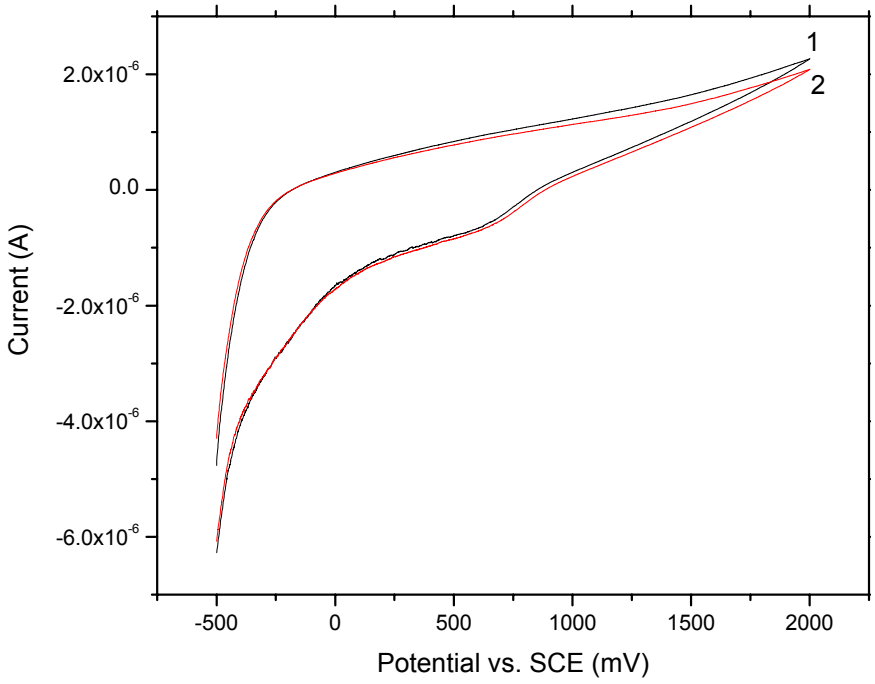

Figure 3.31 Cyclic voltammograms of an a-C:Ti (1.2 at.%) film in H_2SO_4

The multiple cyclic voltammograms of a-C:Ti (1.2 at.%) film are shown in Figure 3.31. The current between 0 and 2000 mV for an a-C:Ti (1.2 at.%) film is <2 μA and is stable with repeated sweeps. No feature due to the oxidation of Ti is observed. Two factors attribute to this phenomenon. One is the minute amount of Ti in the film and the other is the Ti atoms being strongly bonded with the carbon matrix. The result shows the a-C:Ti (1.2 at.%) film has a low background noise with a more than 2000 mV wide electrochemical potential window.

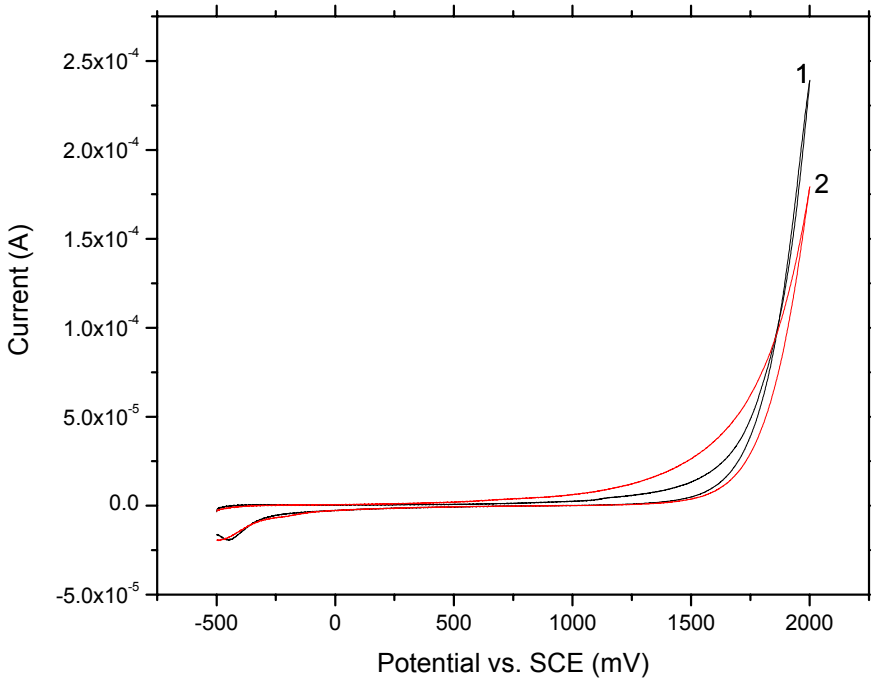

Figure 3.32 Cyclic voltammograms of an a-C:Ti (12.6 at.%) film in H_2SO_4

The multiple cyclic voltammograms of an a-C:Ti (12.6 at.%) film are shown in Figure 3.32. There is a small oxidation peak on the forward sweep at ~1200 mV. The origin of this peak may be the oxidization of Ti within the a-C:Ti film. Because the Ti is bonded with C, this peak appears at a more positive potential when compared to pure Ti.

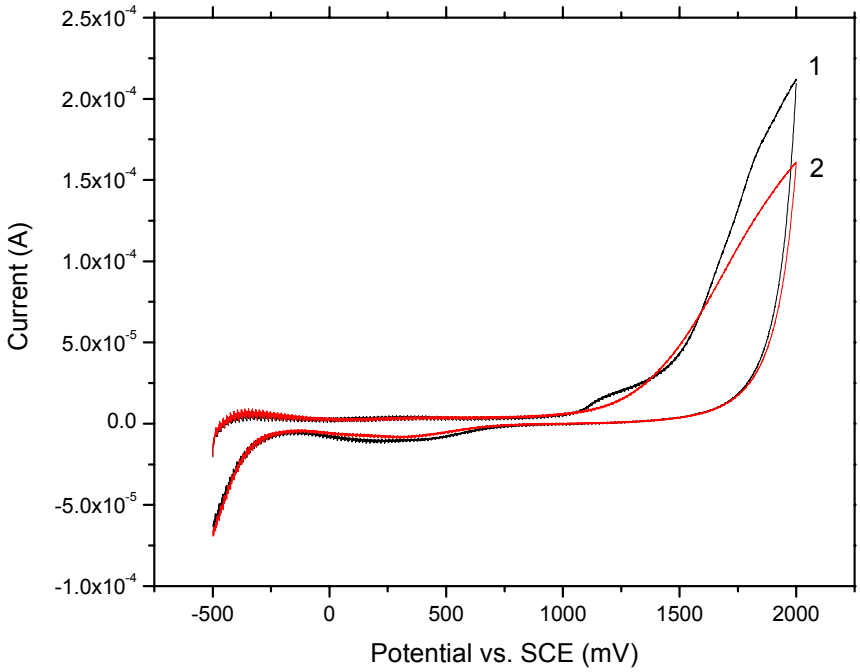

Figure 3.33 Cyclic voltammograms of an a-C:Ti (21.4 at.%) film in H_2SO_4

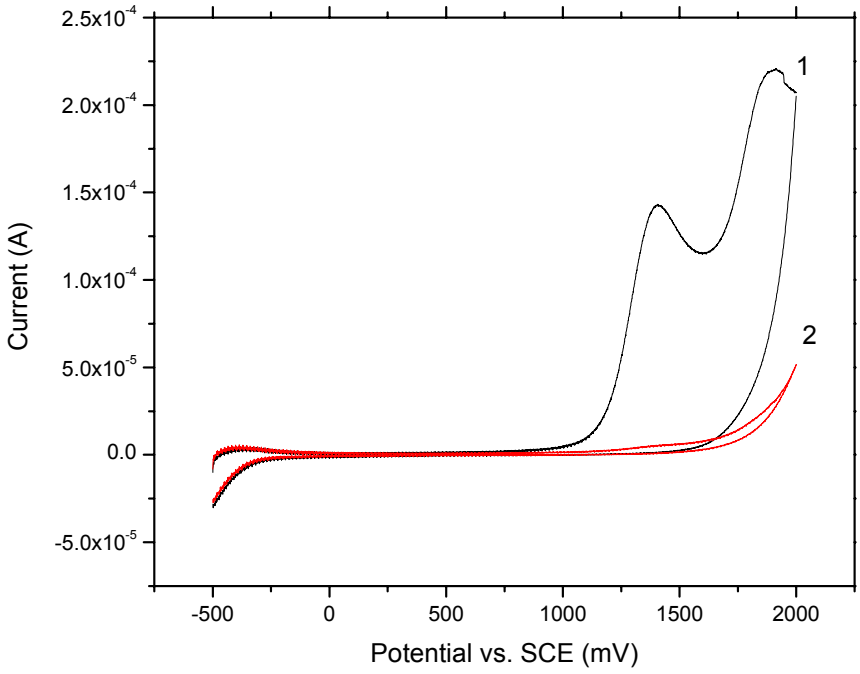

Figure 3.34 Cyclic voltammograms of an a-C:Ti (46.2 at.%) film in H_2SO_4

The multiple cyclic voltammograms of a-C:Ti (21.4 at.%) and a-C:Ti (46.2 at.%) films are shown in Figure 3.33 and Figure 3.34, respectively. Likewise, the oxidation peak has a higher intensity than that of a-C:Ti (12.6 at.%) films. This is consistent with the increase in Ti composition. These results show the low Ti composition films have better electrochemical stability.

The fundamental approach of all impedance methods is to apply a small amplitude sinusoidal excitation signal to the system under investigation and measure the response (current or voltage or another signal of interest) [67]. In the following figure, a non-linear I-V curve for a theoretical electrochemical system is shown.

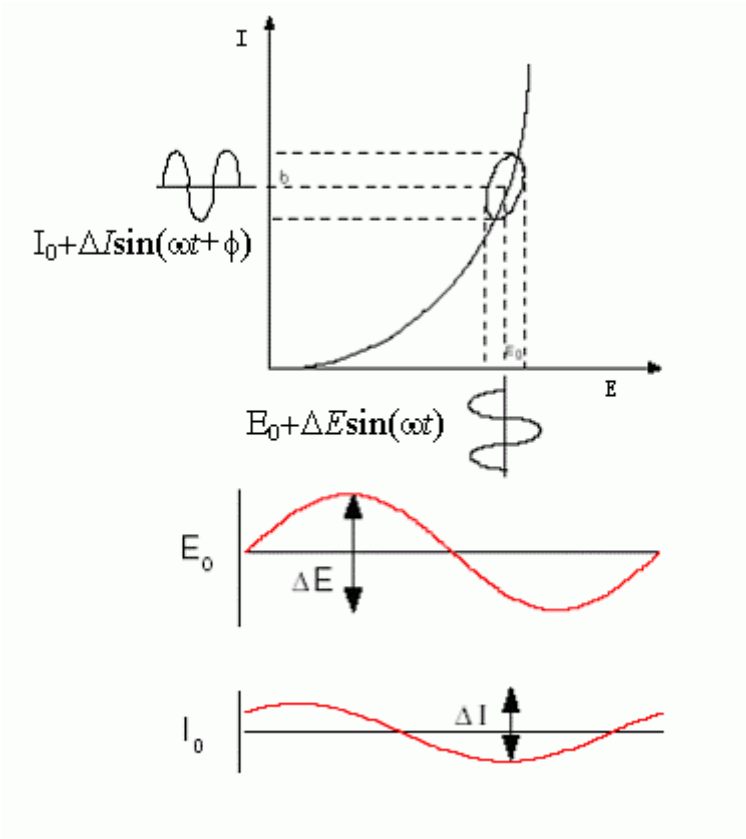

Figure 3.35 The I-V curve for a theoretical electrochemical system

A low amplitude sine wave $\Delta E\sin(\omega t)$, of a particular frequency, is superimposed on the dc polarization voltage E_0. This results in a current response of a sine wave $\Delta I\sin(\omega t+\phi)$ perimposed on the dc current I_0. The current response is shifted with respect to the applied potential. The Taylor series expansion for the current is given by

$$\Delta I = \left(\frac{dI}{dE}\right)_{E_0,I_0}\Delta E + \frac{1}{2}\left(\frac{d^2I}{dE^2}\right)_{E_0,I_0}\Delta E^2 + ... \qquad \textbf{(3.6)}$$

If the magnitude of the perturbing signal dE is small, then the higher order terms in the first equation can be assumed negligible. The impedance of the system can then be calculated using Ohm's law as,

$$Z(\omega) = \frac{\Delta E(\omega)}{\Delta I(\omega)} \qquad \textbf{(3.7)}$$

This ratio is called the impedance, Z(ω), of the system and is a complex quantity with a magnitude and a phase shift which depends on the frequency of the signal. Therefore by varying the frequency of the applied signal one can get the impedance of the system as a function of frequency. Typically in electrochemistry, a frequency range of 100 kHz – 0.1 Hz is used.

The impedance, Z(ω), as mentioned above is a complex quantity and can be represented in Cartesian as well as polar co-ordinates. In polar co-ordinates the impedance of the data is represented by,

$$Z(\omega) = |Z(\omega)|e^{\phi(\omega)} \qquad \textbf{(3.8)}$$

where |Z| is magnitude of the impedance and ϕ is the phase shift. In Cartesian co-ordinates the impedance is given by,

$$Z(\omega) = Z_r(\omega) + jZ_j(\omega) \tag{3.9}$$

where Zr is the real part of the impedance and Zj is the imaginary part and $j = \sqrt{-1}$.

The EIS experiments were conducted with open circuit potentials over a frequency range of 1 mHz to 100 kHz in 5 mM $Fe(CN)_6^{3-/4-}$ and $Ru(NH)_3^{+2/+3}$. The amplitude of AC signal was set to10 mV.

The EIS results can be presented either in Nyquist plots or Bode plots. In the former case, the impedance is plotting the imaginary part as a function of the real part while varying the frequency. The Bode plot directly shows the |Z| and phase angle vs. frequency.

The EIS data can be simulated by the equivalent circuit. As shown in Figure 3.36,

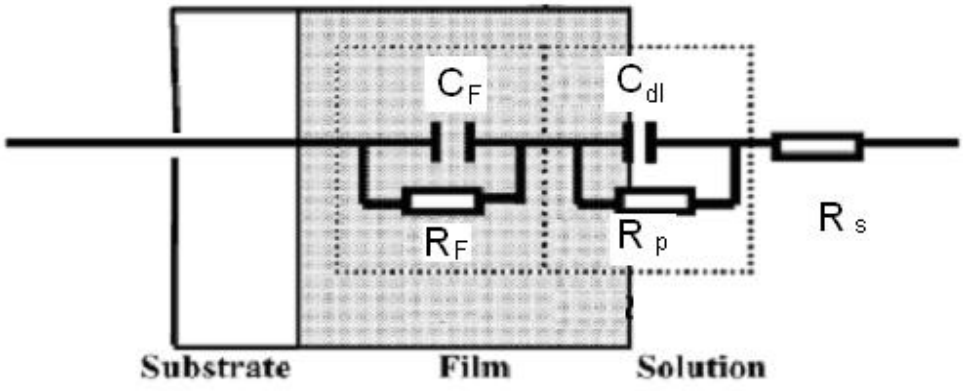

Figure 3.36 The equivalent circuit of chemical reactions

this equivalent circuit can be used to simulate the reaction of an insulating layer coated conductive substrate. In the circuit, C_F and R_F are the capacitance and the ohm resistance of the film, respectively; C_{dl} is the double layer capacitance, while R_p and R_s are the charge resistance of the film and the solution, respectively. If the resistance of film is very low, it can be neglected and the circuit is simply presented by $R_s(C_{dl}R_p)$, a Randle cell.

Both Nyquist and Bode plots for a-C:Ti films in the $Fe(CN)_6^{3-/4-}$ solution are shown in Figure 3.37 - Figure 3.40. It is observed that the total impedance amplitude increases with the increase in Ti composition. This means that the sensitivity of a-C:Ti films to the solution decreases with the increase in Ti composition. A small semi-circle in the Nyquist plot is only observed in an a-C:Ti (1.2 at.%) film. This is caused by the high ohm resistance of the a-C:Ti (1.2 at.%) film. Therefore, the EIS spectrum of a-C:Ti (1.2 at.%) film is simulated by $R_s(C_FR_F)(C_{dl}R_p)$ and those of the a-C:Ti (12.6 at.%), the a-C:Ti (21.4 at.%), and the a-C:Ti (46.2 at.%) films are simulated by $R_s(C_{dl}R_p)$. In simulation, a good fit is achieved by replacing the C_{dl} with a constant-phase-elements (CPE), of which the complex impedance is defined as $Z_{CPE}=[C(j\omega)^n]^{-1}$. The n in the impedance expression describes the deviation of actual electrochemical process occurring at the electrode/solution interface from an ideal capacitor (with n=1) and its value equals to the absolute value of the line-slope of the corresponding linear portion in a log |Z| vs. log (frequency) plot [68].

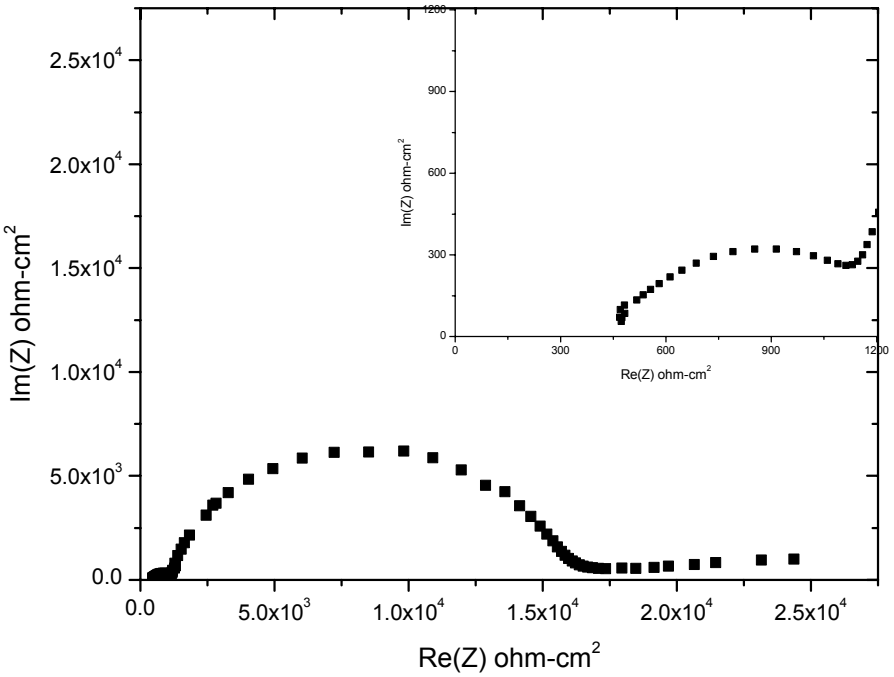

a) A Nyquist plot of an a-C:Ti (1.2 at.%) film measured in $Fe(CN)_6^{3-/4-}$

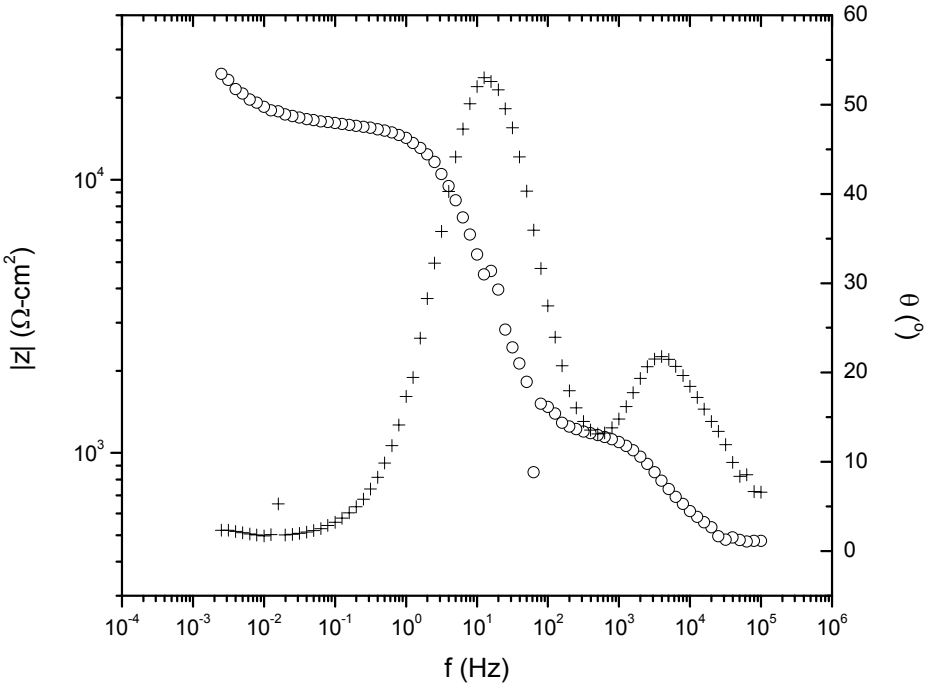

b) A Bode plot of an a-C:Ti (1.2 at.%) film measured in $Fe(CN)_6^{3-/4-}$

Figure 3.37 A Nyquist plot and a Bode plot of an a-C:Ti (1.2 at.%) film measured in $Fe(CN)_6^{3-/4-}$

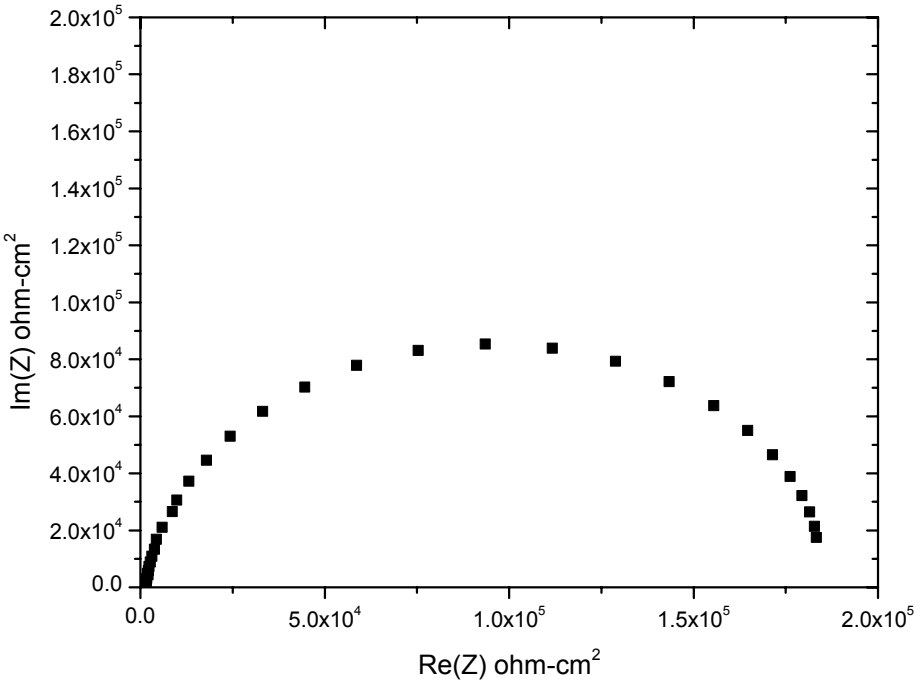

a) A Nyquist plot of an a-C:Ti (12.6 at.%) film measured in $Fe(CN)_6^{3-/4-}$

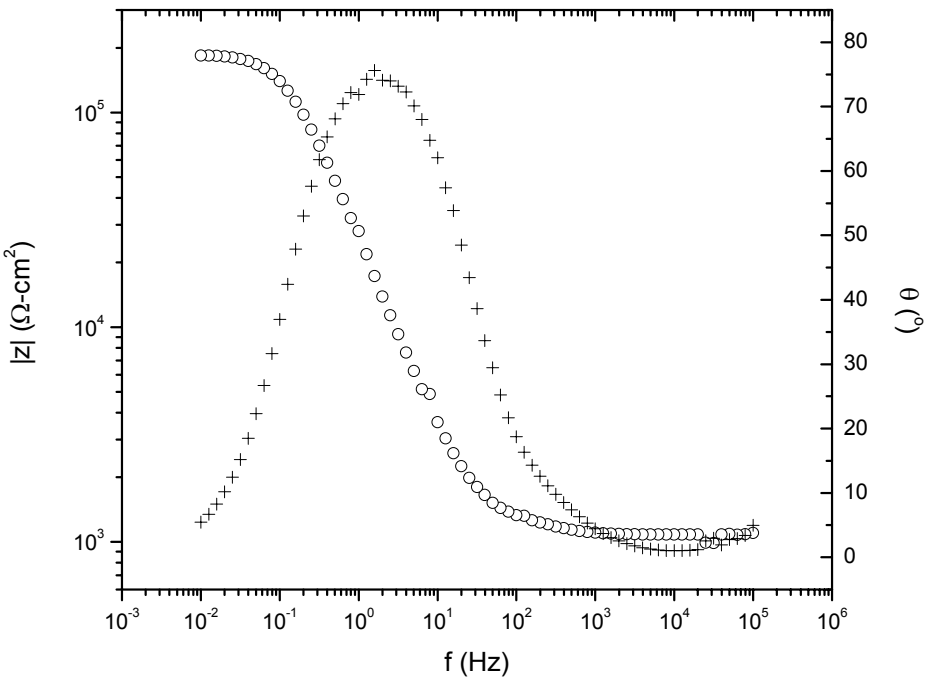

b) A Bode plot of an a-C:Ti (12.6 at.%) film measured in $Fe(CN)_6^{3-/4-}$

Figure 3.38 A Nyquist plot and a Bode plot of an a-C:Ti (12.6 at.%) film measured in $Fe(CN)_6^{3-/4-}$

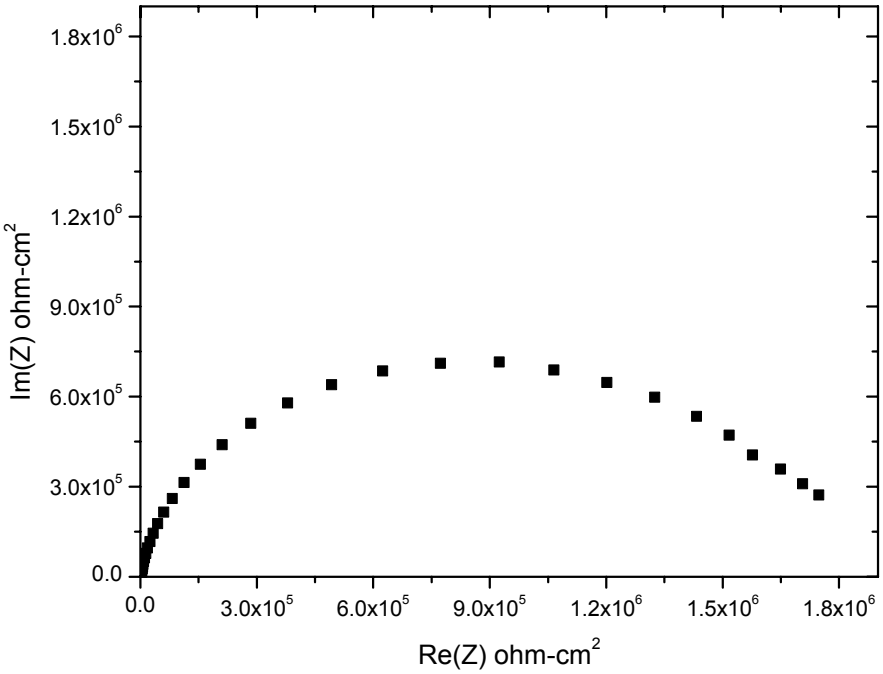

a) A Nyquist plot of an a-C:Ti (21.4 at.%) film measured in $Fe(CN)_6^{3-/4-}$

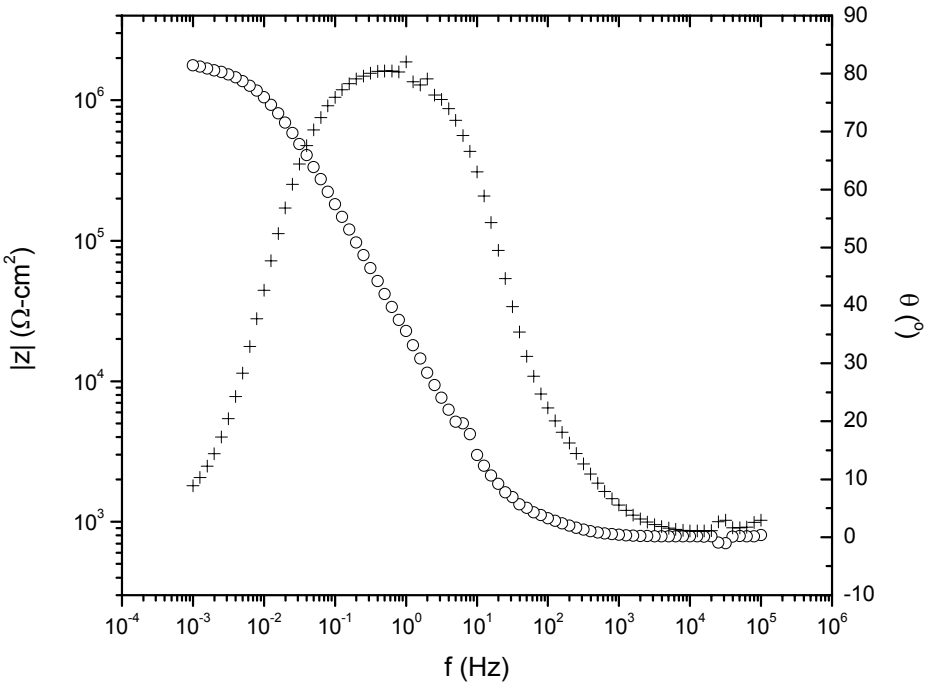

b) A Bode plot of an a-C:Ti (21.4 at.%) film measured in $Fe(CN)_6^{3-/4-}$

Figure 3.39 A Nyquist plot and a Bode plot of an a-C:Ti (21.4 at.%) film measured in $Fe(CN)_6^{3-/4-}$

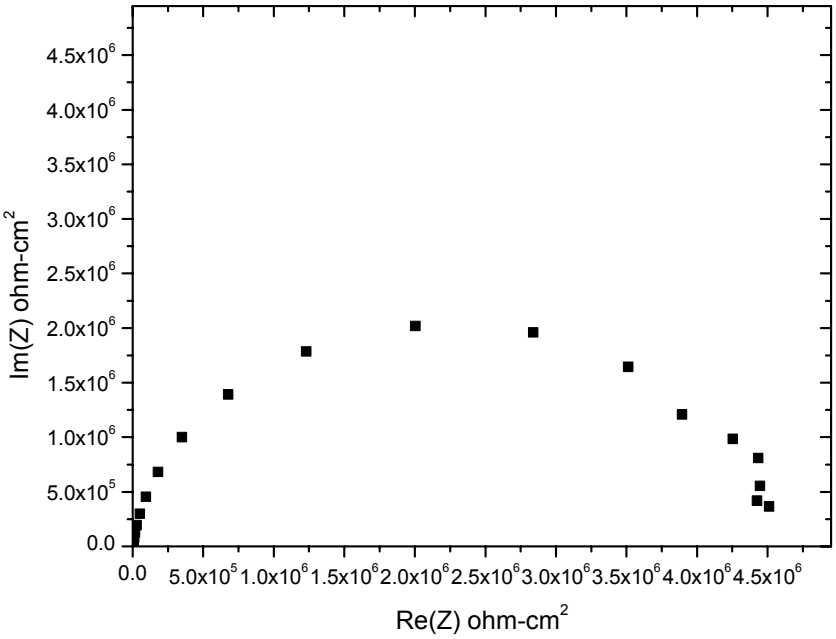

a) A Nyquist plot of an a-C:Ti (46.2 at.%) film measured in $Fe(CN)_6^{3-/4-}$

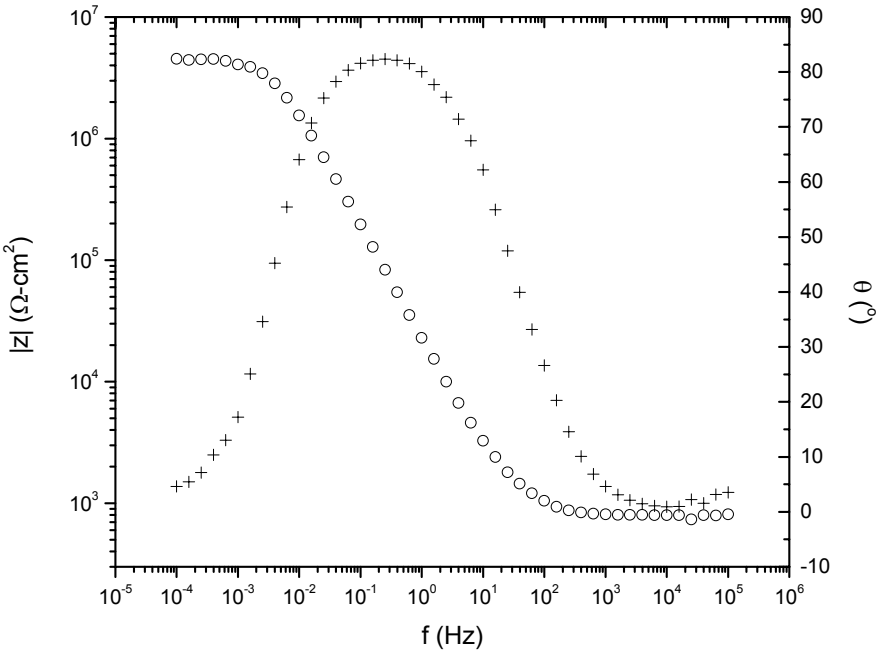

b) A Bode plot of an a-C:Ti (46.2 at.%) film measured in $Fe(CN)_6^{3-/4-}$

Figure 3.40 A Nyquist plot and a Bode plot of an a-C:Ti (46.2 at.%) film measured in $Fe(CN)_6^{3-/4-}$

Table 3.1 The simulation results of a-C:Ti EIS spectra in $Fe(CN)_6^{3-/4-}$

Sample	Rs (Ω-cm^2)	R_F(Ω-cm^2)	C_F(nF)	R_P(kΩ-cm^2)	C_{dl}(uF-cm^2)	n
a-C:Ti (1.2 at.%)	489	600	77.7	14.54	1.812	0.9402
a-C:Ti (12.6 at.%)	1107	--	--	192.5	2.135	0.9093
a-C:Ti (21.4 at.%)	810	--	--	1744	2.399	0.9035
a-C:Ti(46.2 at.%)	815	--	--	4620	2.398	0.9099

The results of simulations are shown in Table 3.1. The main observation is that R_p increases from 14.54 kΩ-cm^2 to 4.620 MΩ-cm^2, which indicates that the charge-transfer kinetics is much lower for the low Ti composition films. The double layer capacitance increases lightly from 1.812 to 2.398 uF-cm^2. These values are much smaller than that of most popular electrode materials, such as a sol-gel graphite paste electrode (2.9 ~ 59.5 mF cm^2), platinum (20 ~ 40 uF-cm^2) or mercury (10 ~ 30 uF-cm^2) [69, 70, 71]. This small capacitance leads to a low capacitance charge current and a faster response, which makes the a-C:Ti films good potential electrode materials for fast electroanalysis applications.

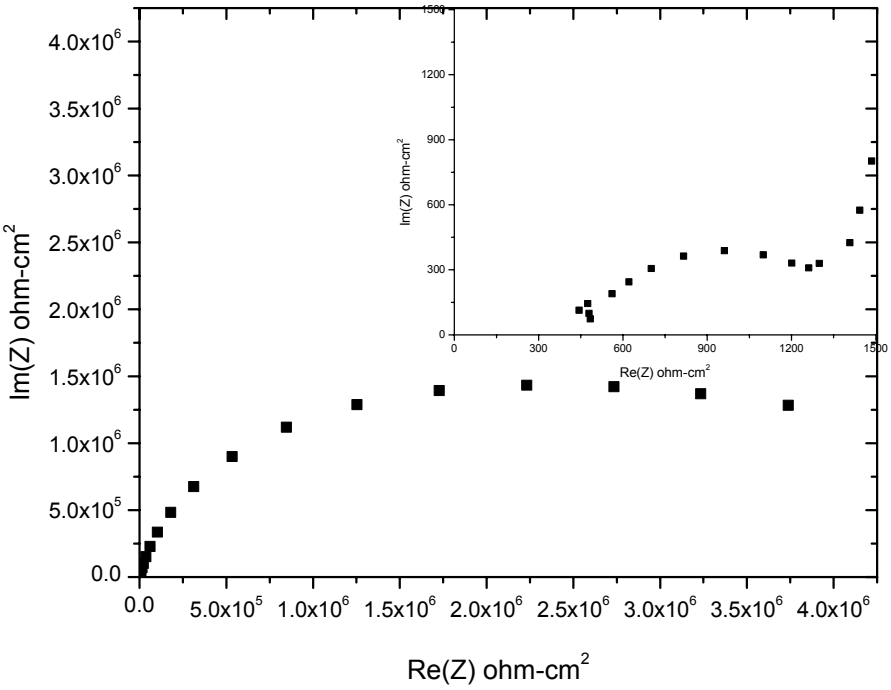

a) A Nyquist plot of an a-C:Ti (1.2 at.%) film measured in $Ru(NH)_3^{2+/3+}$

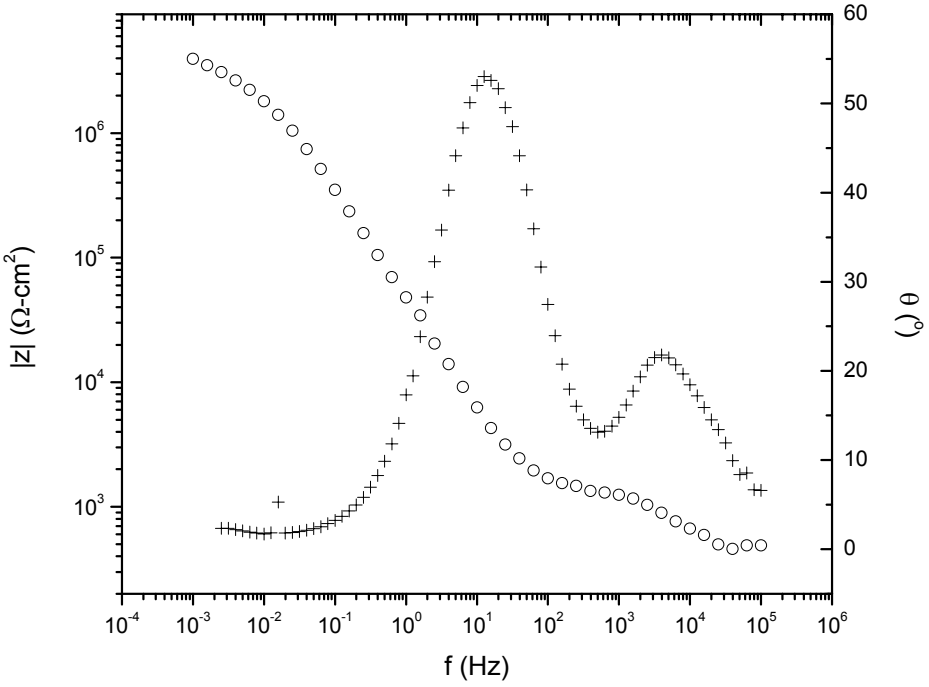

b) A Bode plot of an a-C:Ti (1.2 at.%) film measured in $Ru(NH)_3^{2+/3+}$

Figure 3.41 A Nyquist plot and a Bode plot of an a-C:Ti (1.2 at.%) film measured in $Ru(NH)_3^{2+/3+}$

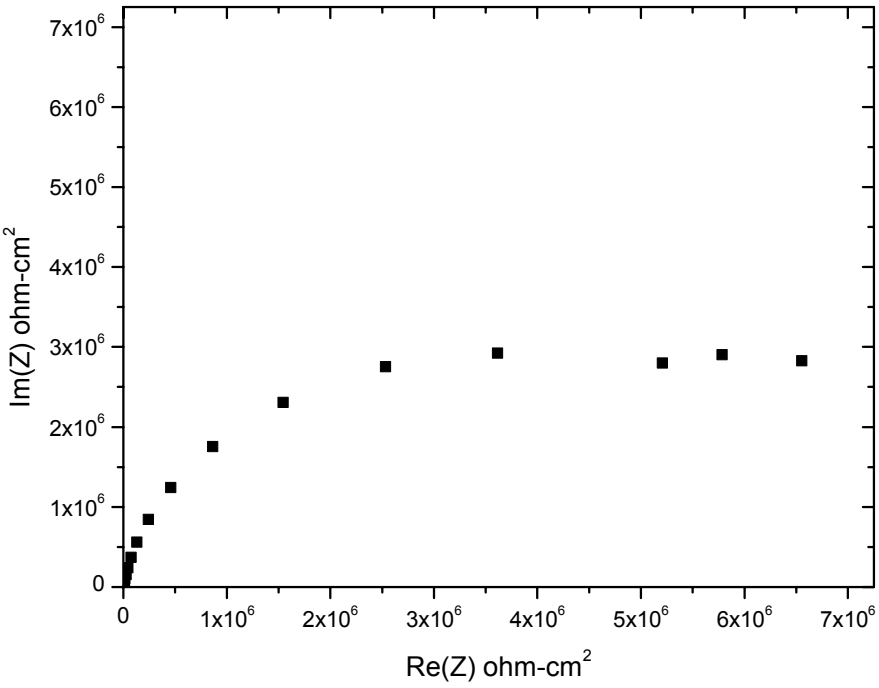

a) A Nyquist plot of an a-C:Ti (12.6 at.%) film measured in $Ru(NH)_3^{2+/3+}$

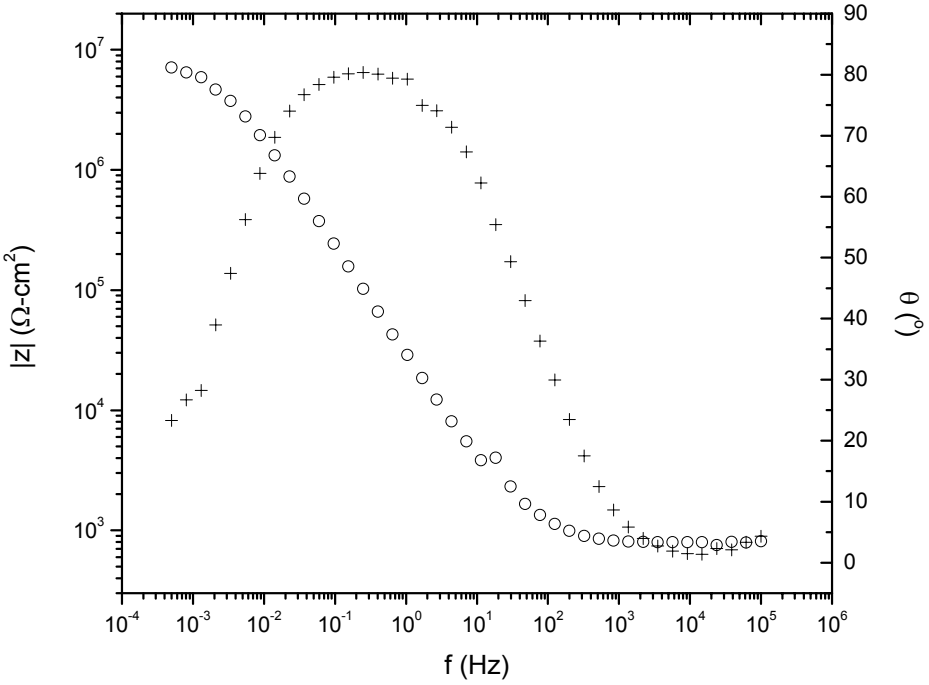

b) A Bode plot of an a-C:Ti (12.6 at.%) film measured in $Ru(NH)_3^{2+/3+}$

Figure 3.42 A Nyquist plot and a Bode plot of an a-C:Ti (12.6 at.%) film measured in $Ru(NH)_3^{2+/3+}$

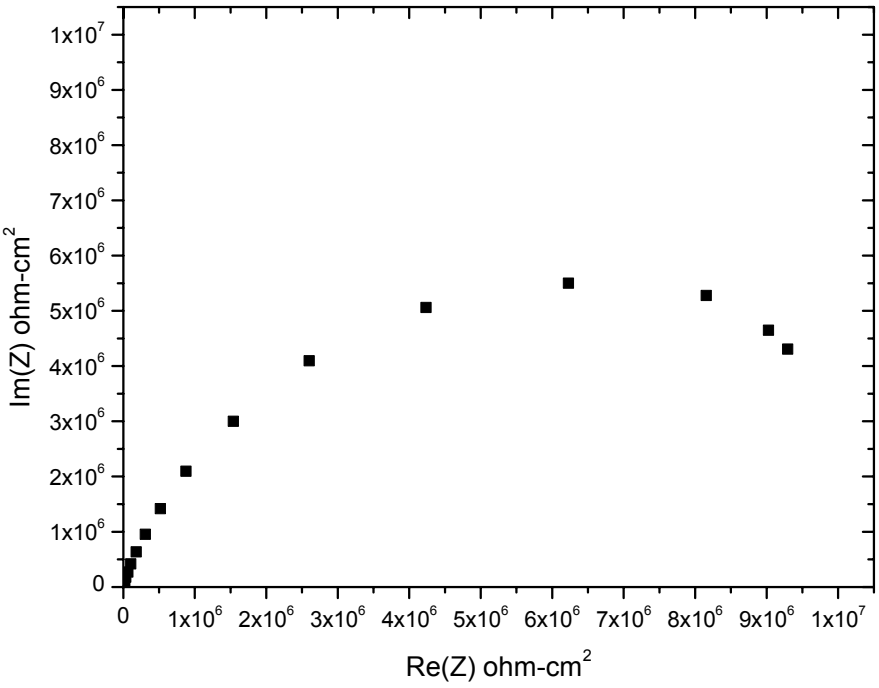

a) A Nyquist plot of an a-C:Ti (21.4 at.%) film measured in $Ru(NH)_3^{2+/3+}$

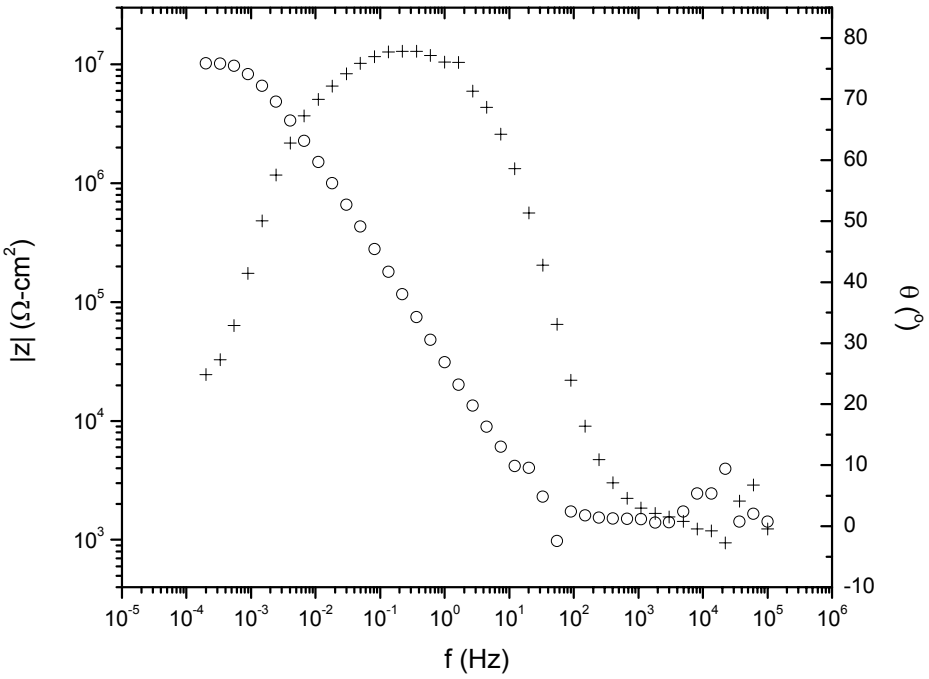

b) A Bode plot of an a-C:Ti (21.4 at.%) film measured in $Ru(NH)_3^{2+/3+}$

Figure 3.43 A Nyquist plot and a Bode plot of an a-C:Ti (21.4 at.%) film measured in $Ru(NH)_3^{2+/3+}$

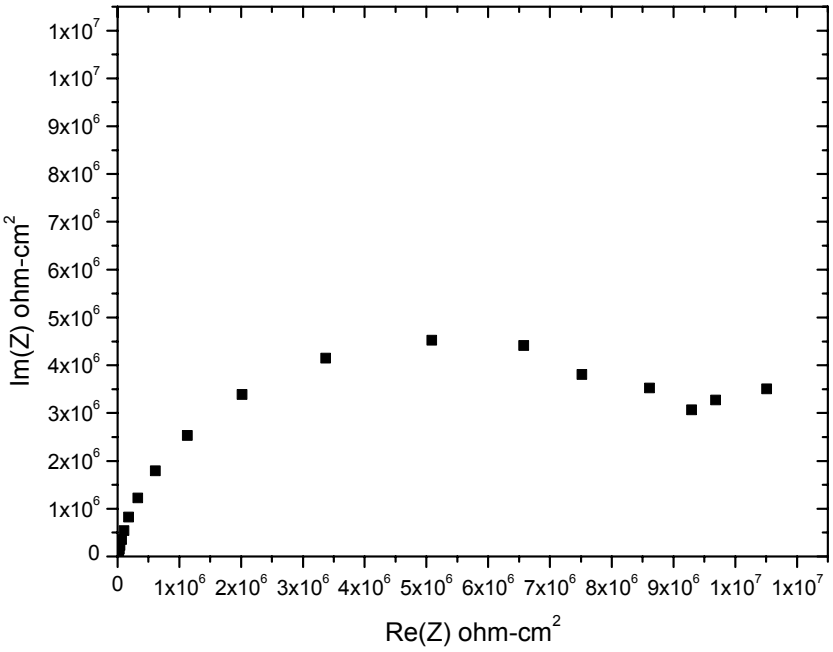

a) A Nyquist plot of an a-C:Ti (46.2 at.%) film measured in $Ru(NH)_3^{2+/3+}$

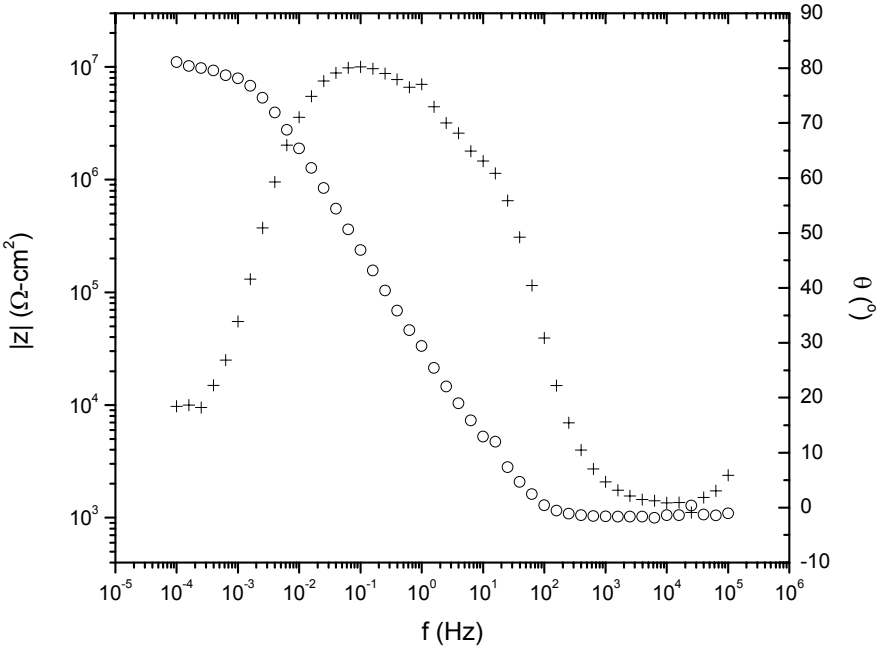

b) A Bode plot of an a-C:Ti (42.6 at.%) film measured in $Ru(NH)_3^{2+/3+}$

Figure 3.44 A Nyquist plot and a Bode plot of an a-C:Ti (42.6 at.%) film measured in $Ru(NH)_3^{2+/3+}$

Both Nyquist and Bode plots for a-C:Ti films measured in the $Ru(NH)_3^{2+/3+}$solution are shown in Figure 3.41 -Figure 3.44. Similar to the EIS spectra in $Fe(CN)_6^{3-/4-}$ solution, the total impedance amplitude increases with the increase in Ti composition. But the impedance value is much higher than that in the $Fe(CN)_6^{3-/4-}$ solution. This indicates that the a-C:Ti films are more sensitive to the $Fe(CN)_6^{3-/4-}$ solution. Thus the a-C:Ti is more active with the negative charged ions in the solution. The results of simulations are shown in Table 3.2.

Table 3.2 The simulation results of a-C:Ti EIS spectra in $Ru(NH)_3^{2+/3+}$

Sample	Rs (Ω-cm^2)	R_F(Ω-cm^2)	C_F(nF)	R_P(MΩ-cm^2)	C_{dl}(uF-cm^2)	n
a-C:Ti (1.2 at.%)	475	769	54.8	3.73	0.703	0.8705
a-C:Ti (12.6 at.%)	811	--	--	7.82	1.104	0.8722
a-C:Ti (21.4 at.%)	1424	--	--	12.04	1.234	0.8761
a-C:Ti(46.2 at.%)	1030			11.03	0.9295	0.866

The CV and EIS study shows the low Ti composition a-C:Ti film has a wide electrochemical window with low background noise and is more sensitive to the electrochemical reaction. Due to its small double layer capacitance, it is promising to be used as the electroanalysis electrode.

3.7 Summary

In this chapter, the microstructure, morphology, composition, surface energy, mechanical, electrical and electrochemical properties of a-C:Ti films are investigated in detail. The Ti composition in a-C:Ti films increases with the increase in Ti composition in the composite targets. The Ti composition in a-C:Ti films has a maximum value at - 80V bias. The sp^2 cluster size and composition increase with the increase in Ti composition in the targets. The a-C:Ti film is sp^3 rich at the mid bias. The surface energy of a-C:Ti films is not sensitive to either the Ti composition or substrate bias. Ti incorporation has been found to be an effective method to decrease the internal stress of a-C films. Though such incorporation also results in the decrease of hardness and Young's modulus, their values remain relatively high (much higher than that of a-C:H films). The relatively high conductivity of TiC phase in a-C:Ti is responsible for the low resistivity of the a-C:Ti films with high titanium composition. All a-C:Ti films exhibit a wide electrochemical window and a small double layer capacitance. The electrochemical stability of the low Ti composition films is excellent. The sensitivity of a-C:Ti films to the negative ions solution is much higher than that to the positive ions solution. The sensitivity of the a-C:Ti films decreases with the increase in Ti composition. Therefore the low Ti composition a-C:Ti films are more suitable for electrochemical applications.

Chapter 4. Al Containing Amorphous Carbon Films

4.1 Film Composition and Chemical Bonding States

The film composition of a-C:Al films was calculated by XPS. The chemical bonding state of each element was studied by narrow scan XPS.

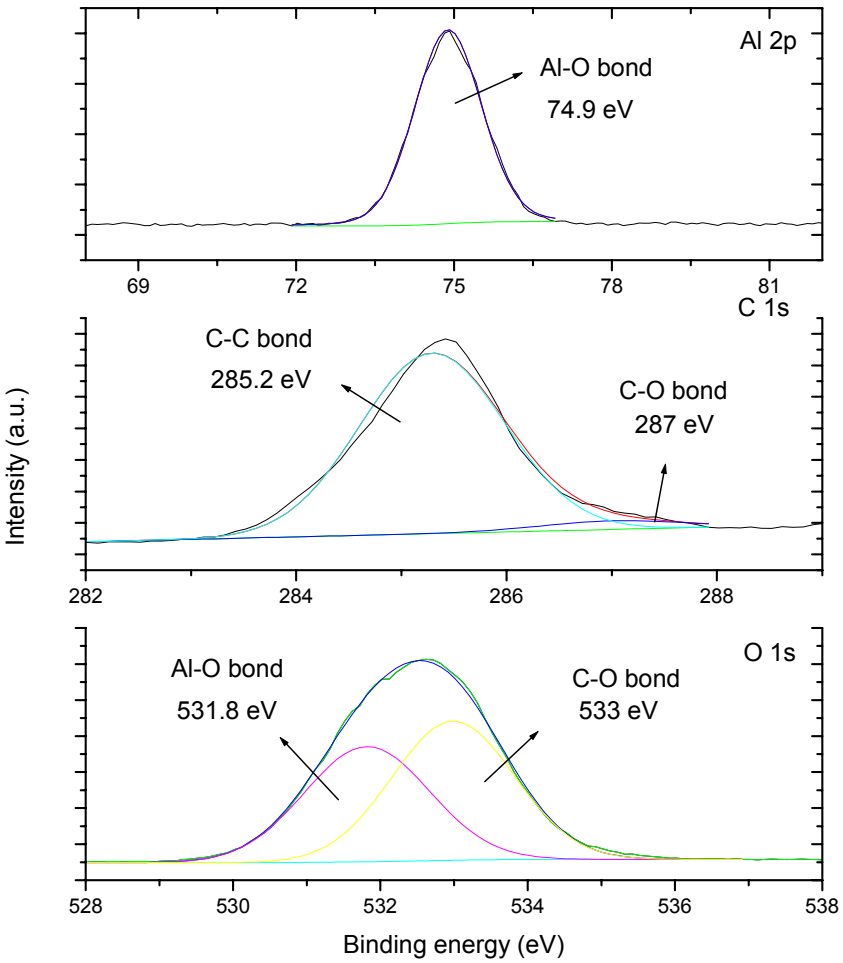

Figure 4.1 Narrow scans of an a-C:Al film deposited from a 5 at.% target at –80 V bias

Typical Al 2p, C 1s, and O 1s XPS spectra of a-C:Al film are shown in Figure 4.1. The Al 2p peak corresponds to the Al-O bond (Al 2p at 74.9 eV) [72]. There was no Al carbide phase found. The C 1s peak is presented as two components. The peak around 285.2 eV corresponds to the C-C bond. The peak around 287 eV can be attributed to the C-O bond. Similar to a-C:Ti films, the oxygen was absorbed from the environment and chemically bonded with Al and carbon when the freshly deposited films were stored in ambience.

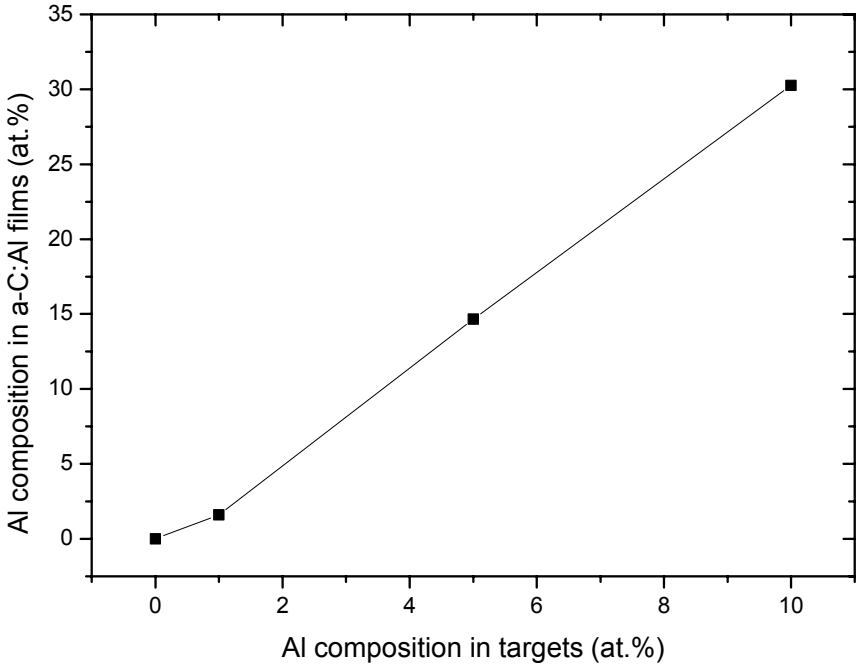

Figure 4.2 The Al composition in films vs. the Al composition in targets

The Al composition of a-C:Al films deposited from different Al composition composite targets is shown in Figure 4.2. The Al composition in the films increases with the increase in metal composition in the targets and is always larger than that in

the targets. This is attributed to the low melting point of Al (~660^{o}C) in comparison with that of graphite (~3870^{o}C).

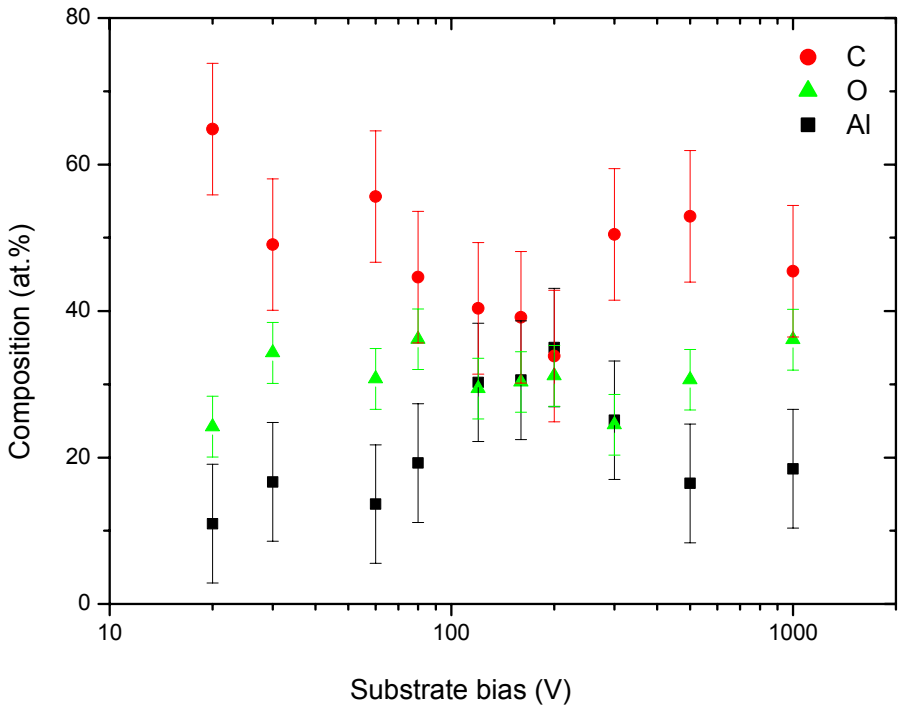

Figure 4.3 The film composition of a-C:Al films deposited at different bias

The films composition of a-C:Al films deposited from the 5 at.% Al containing composite target at different bias is shown in Figure 4.3. Similar to that of a-C:Ti films, the Al composition increases with the increase in substrate bias but decreases with further increase in substrate bias. The a-C:Al film deposited at –200 V has the highest Al composition, while the a-C:Ti film deposited at –80 V has the highest Ti composition. The different behavior for Ti and Al on the metal composition is discussed in Chapter 7 in detail.

4.2 Microstructure and Morphology

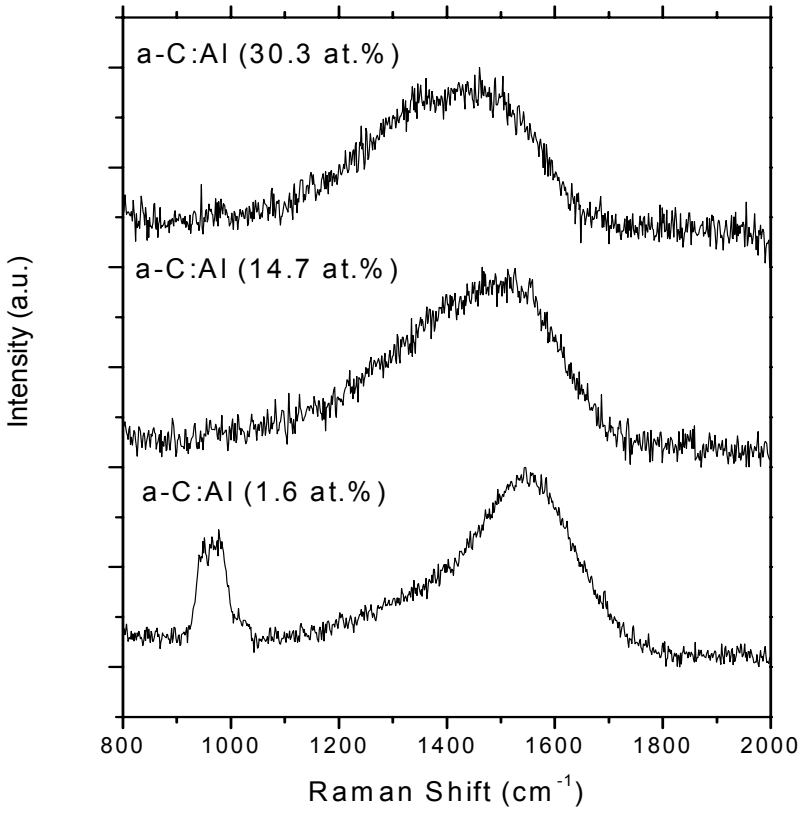

Figure 4.4 Raman Spectra of a-C:Al films

The Raman spectra of a-C:Al films deposited from different Al composition metal/carbon targets are shown in Figure 4.4. In the wavenumber region of 1100-1700 cm^{-1}, there is a broad asymmetric scattering band, which is typical of ta-C films.

The Breit-Wigner-Fano (BWF) method was used to fit the above spectra. The I_D/I_G ratio is shown in Figure 4.5. D peak is used for the fitting. The I_D/I_G ratio of a-C:Al (1.6 at.%) and a-C:Al (14.7 at.%) is almost same. It means the sp^2 cluster size is not

sensitive to the Al composition when it is less than 14.7 at.%. Increasing the Al composition further, the I_D/I_G ratio increases to 0.74. The film contains much bigger sp^2 clusters.

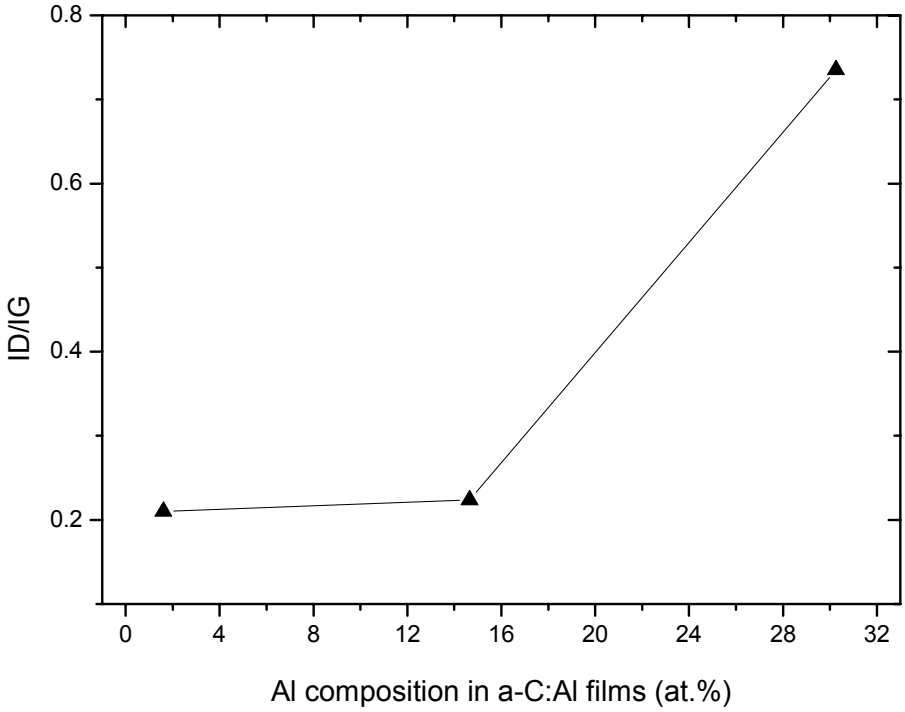

Figure 4.5 The I_D/I_G ratio of a-C:Al films with different Al composition

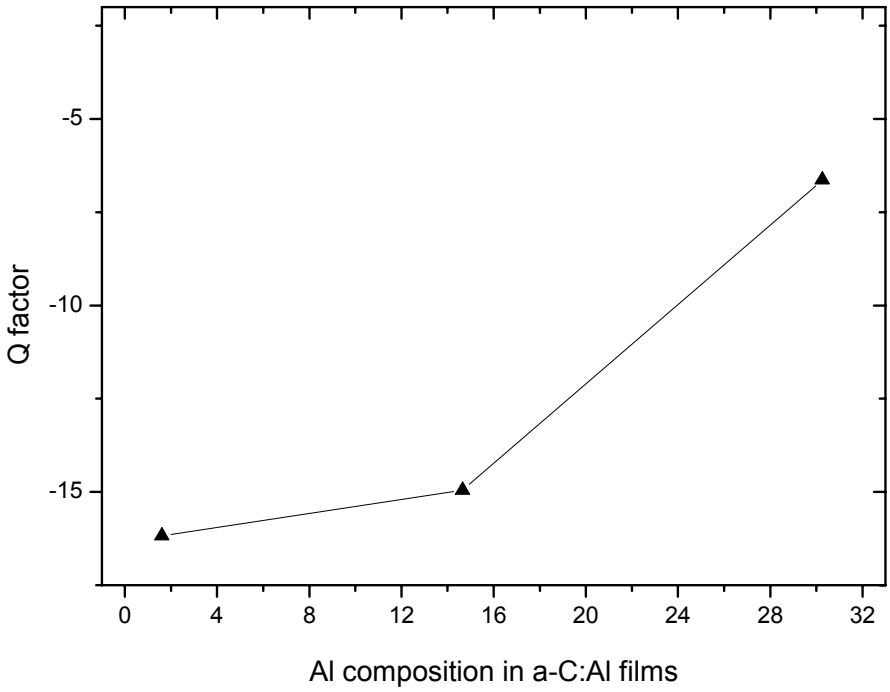

Figure 4.6 The Q factor of a-C:Al films with different Al composition

The Q factor is shown in Figure 4.6. The Q factor continuously decreases with the increase in Al composition. This indicates the sp^3 composition decreases. Similar to the a-C:Ti film, Al atoms affect their neighboring C atoms to form sp^3 structure.

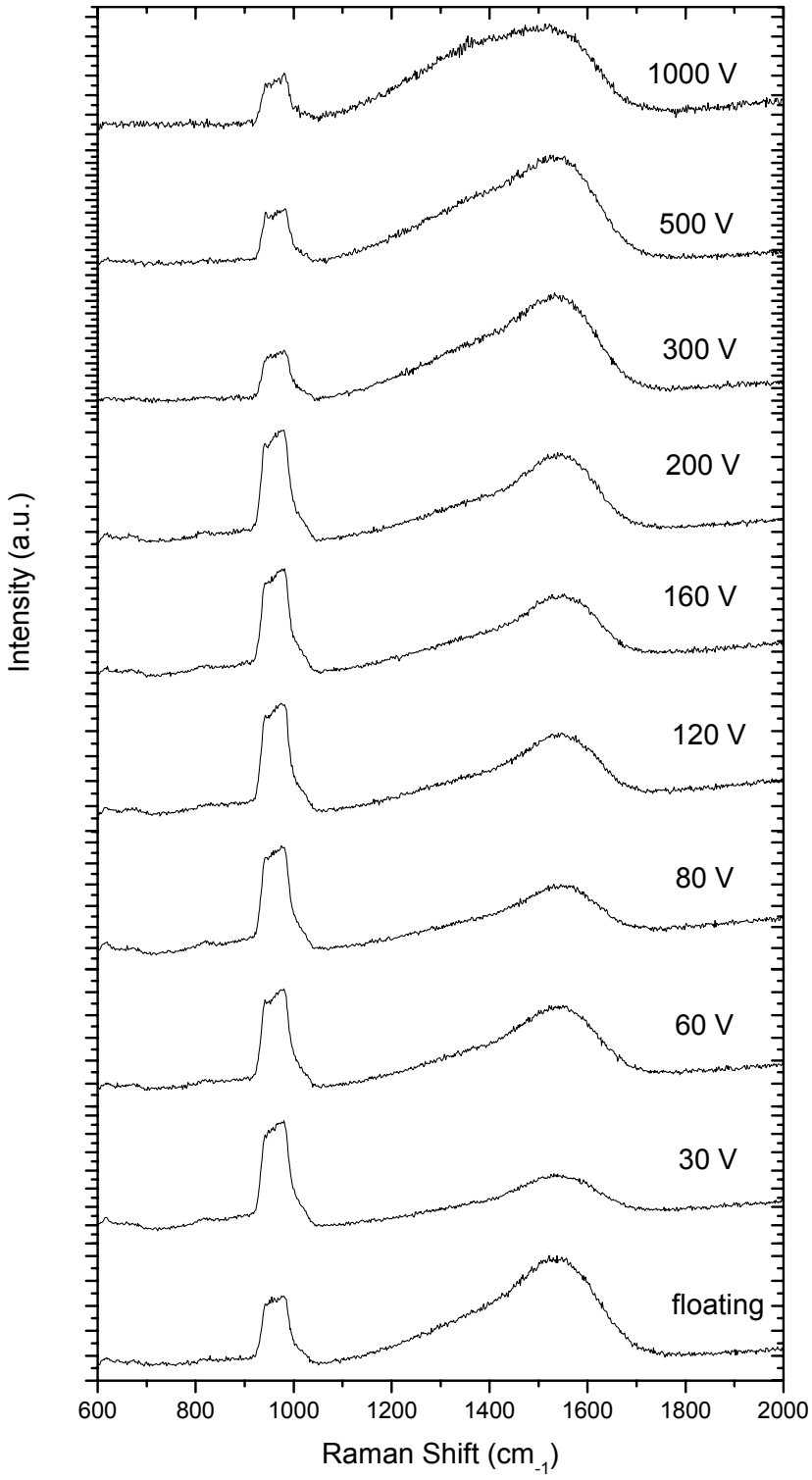

Figure 4.7 Raman spectra of a-C:Al films deposited at different bias

The Raman spectra of a-C:Al films deposited at different bias from the 5 at.% Al composition targets are shown in Figure 4.7. The peak around 950 cm^{-1} is the second order vibrational mode of the Si substrate. Similar to that of a-C:Ti films, the Si signal increases with the increase in substrate bias from floating to mid bias but decreases with further increase in substrate bias. According to the previous discussion on the relation between the Si signal and the sp^3 composition, the a-C:Al films have a maximum sp^3 composition around –80 V bias.

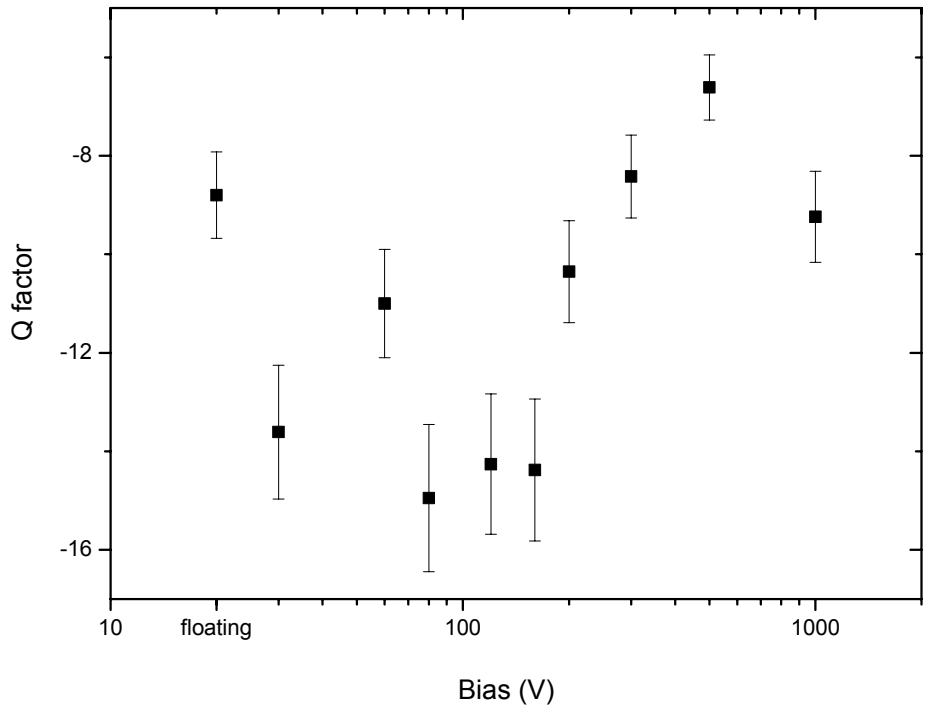

Figure 4.8 The Q factor of a-C:Al films deposited at different bias

The BWF method was used to fit the broad asymmetric scattering band in the wavenumber region of 1100-1700 cm^{-1}. Figure 4.8 shows the Q factor as a function of

substrate bias. The Q factors of a-C:Al films deposited at –80 V, -120 V and –200 V are very close to each other, which indicates that these films have a similar sp^3 composition. The shape of Figure 4.8 is very similar to that of ta-C and a-C:Ti films deposited at different energy [50]. This suggests that the sp^3 composition of a-C:Al films is rich at mid bias.

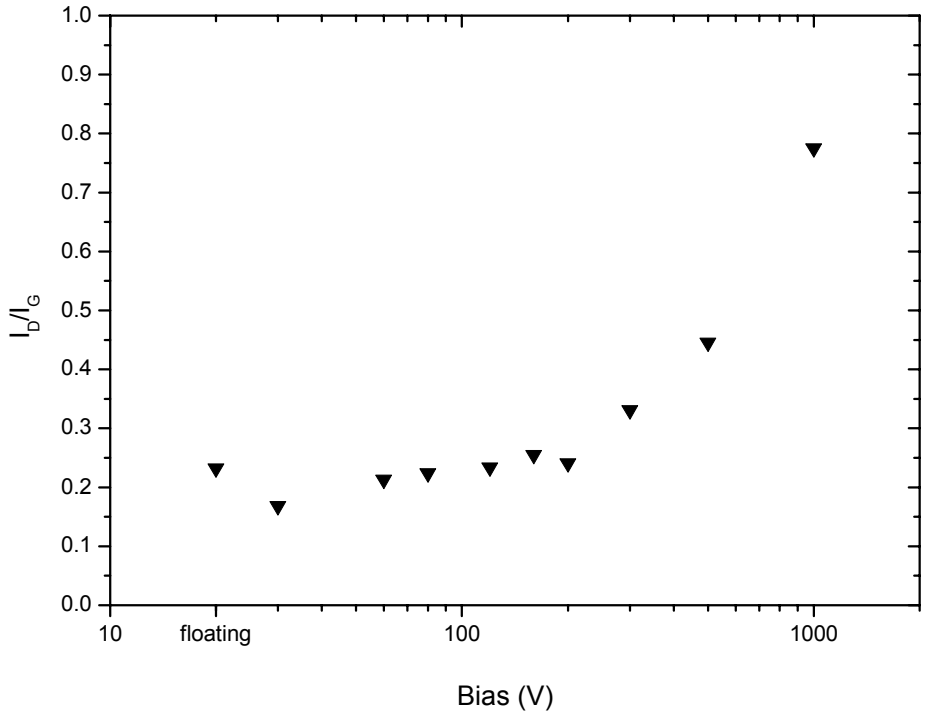

Figure 4.9 The I_D/I_G ratio of a-C:Al films deposited at different bias

The I_D/I_G ratio is shown in Figure 4.9. The I_D/I_G ratio of a-C:Al films remains almost constant with increasing bias to –200 V and increases with further increase in bias to –1000 V. This indicated that the size of the sp^2 clusters within the a-C:Al films is not affected by the substrate bias up to –200V and increases when higher bias is applied.

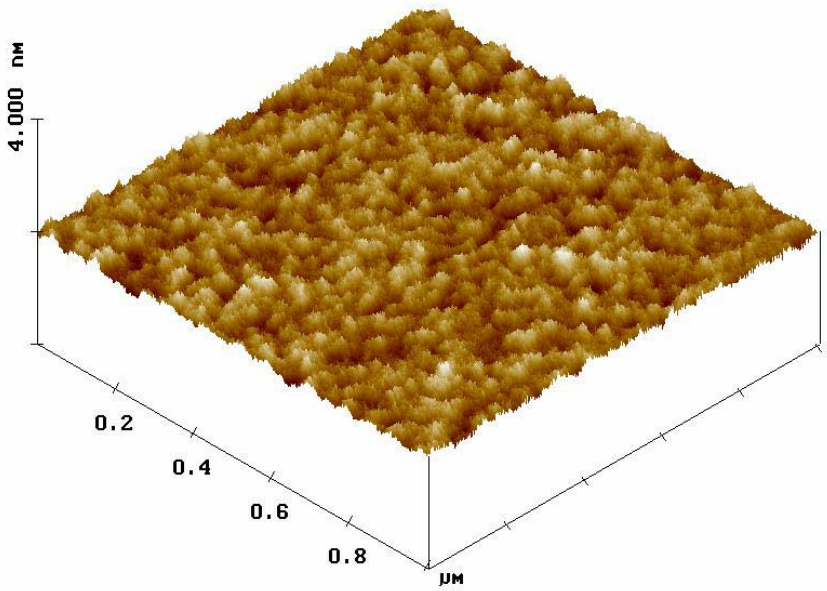

Figure 4.10 A typical AFM image of a-C:Al film

A typical image of the a-C:Al film deposited from a 5 at.% composite target at –80 V bias is shown in Figure 4.10. The RMS roughnesses of a-C:Al (1.6at.%), a-C:Al .7 (14at.%), and a-C:Al (30.3 at.%) are 0.10 nm, 0.28 nm, and 0.33 nm, respectively.

4.3 Surface Energy

Figure 4.11 and Figure 4.12 show the contact angle for water in contact with a-C:Al films with different Al composition and a-C:Al films deposited at various bias, respectively. The contact angle for both a-C:Al films with different Al composition and a-C:Al films deposited at various bias deposited with various substrate bias show relatively constant, around 102 ^{o}. A typical image of an a-C:Al film in contacting with water is shown in Figure 4.13. This value is larger than that of a-C:Ti films, which indicates that the a-C:Al is more hydrophobic.

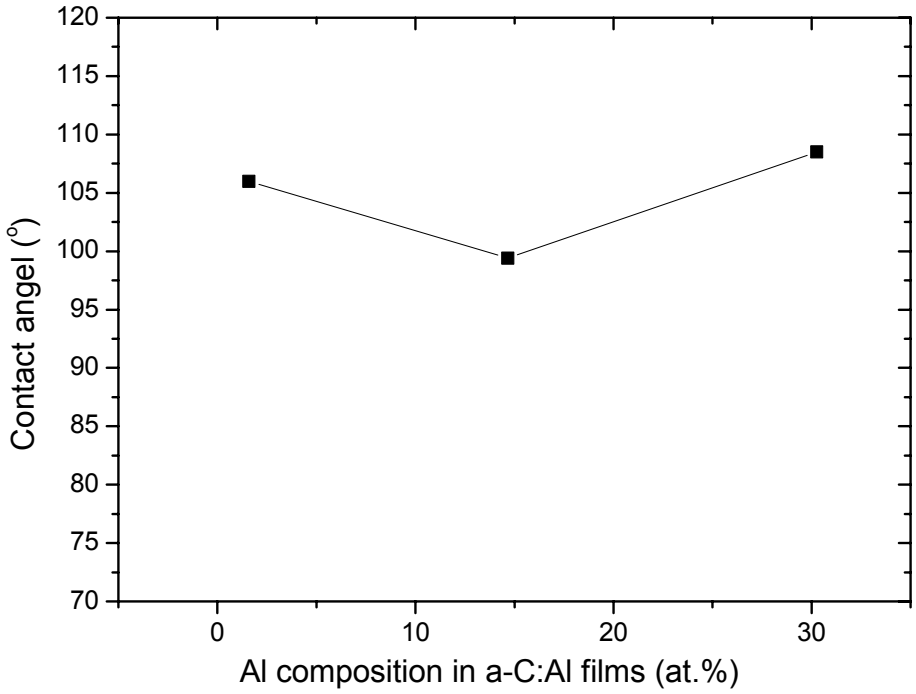

Figure 4.11 The contact angle between water and a-C:Al with different Al composition

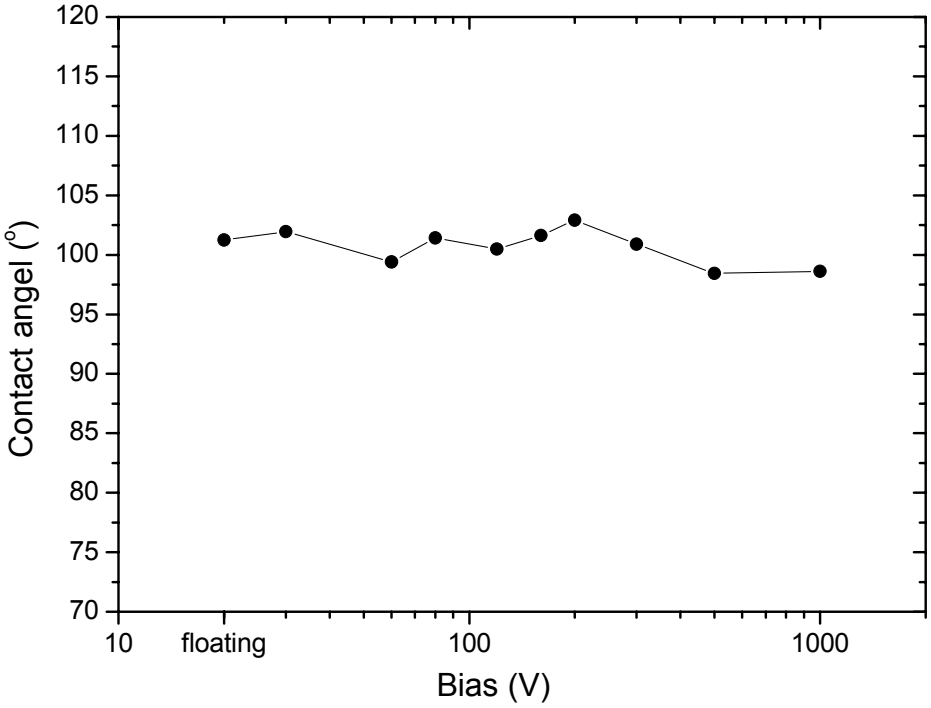

Figure 4.12 The contact angle between water and a-C:Al as a function of bias

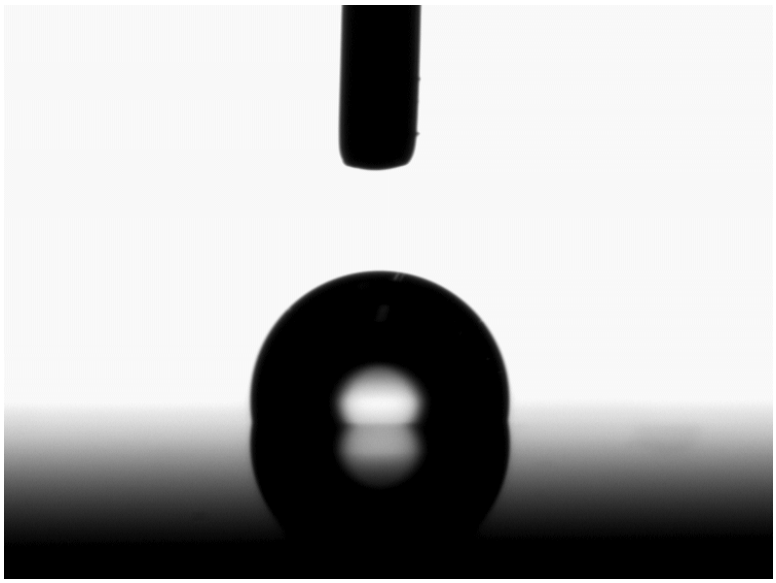

Figure 4.13 A typical image of an a-C:Al film in contacting with water

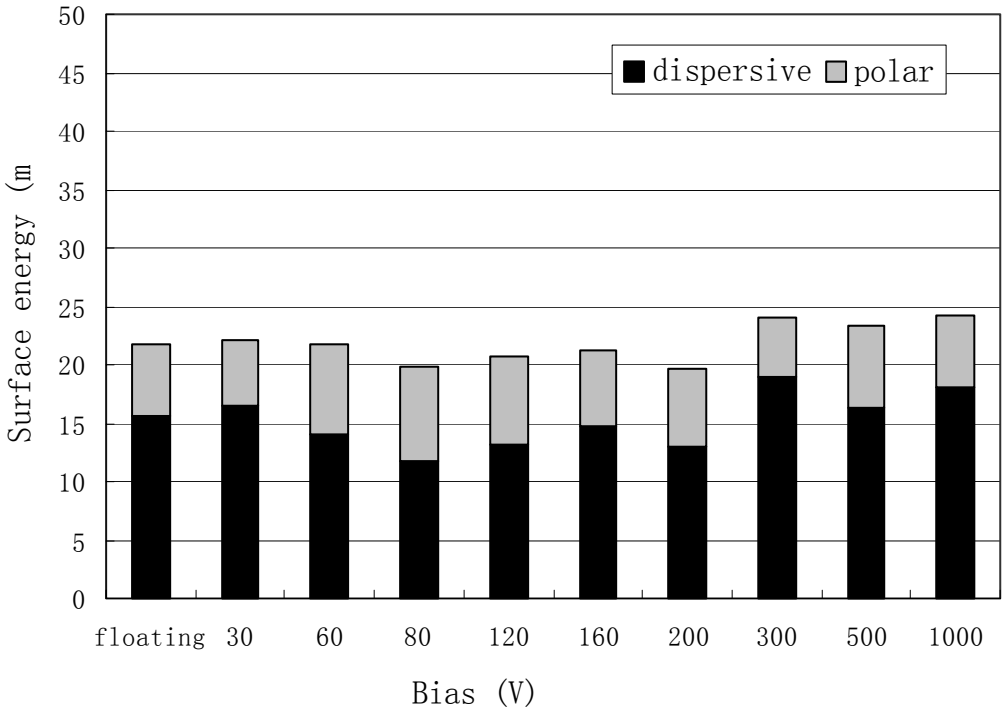

Figure 4.14 The surface energy of a-C:Al films as a function of bias

The surface energy, including both the dispersive and polar components was calculated using the contact angle for three liquids. The dispersive and polar components and total surface energy of the a-C:Al films deposited at various bias are shown in Figure 4.14. Within experimental error, both the dispersive and polar components of a-C:Al films are independent of the bias. It is noticed that the polar component of the a-C:Al films is as low as 6.64 mN/m. The formation of the Al-O electrovalent bond makes the electron of the Al localized [55]. Thus, the induced dipole decreases and the polar component of surface energy decreases.

Unlike in the a-C:Ti film, there is no change in the contact angle for the a-C:Al film when it is under UV irradiation.

4.4 Mechanical Properties

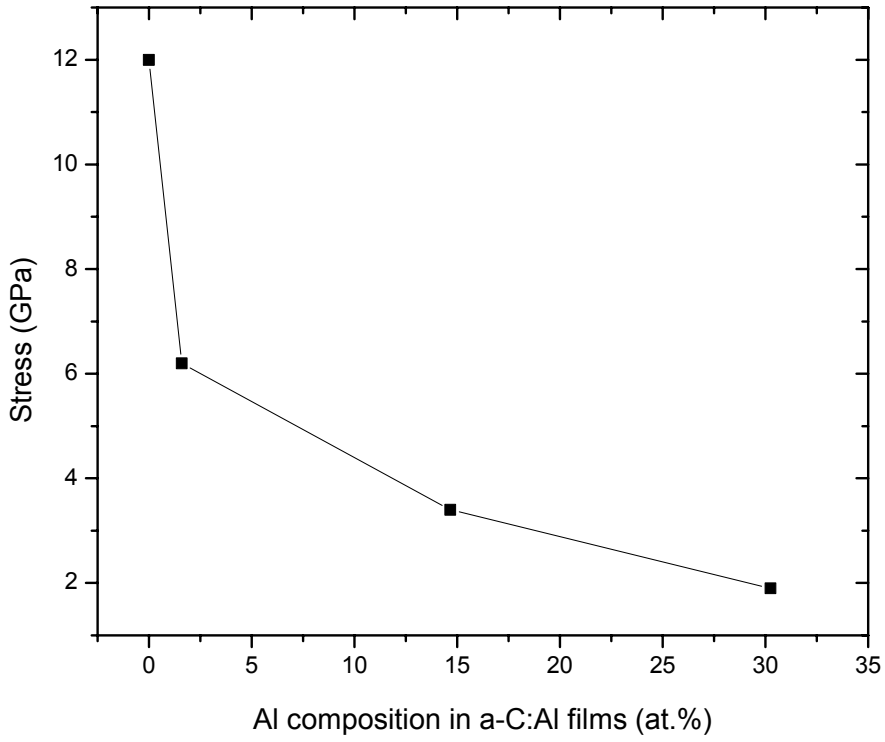

Figure 4.15 The stress of a-C:Al films with different Al composition

Figure 4.15 shows the stress of a-C:Al films as a function of the metal composition in the films. It is clear that incorporating Al into films leads to the reduction of compressive stress. Only 1.6 at.% Al in the film makes the stress drop to 6.2 GPa. With further increase in Al composition to 30.3 at.%, the stress drops from 6.2 to 1.9 GPa. The reduction of sp^3 composition is attributed to the reduction of stress. The stress of a-C:Al film with same metal composition is lower than that of a-C:Ti film. The reason may be the Al in bulk is softer than Ti and there is a hard TiC phase in a-C:Ti films.

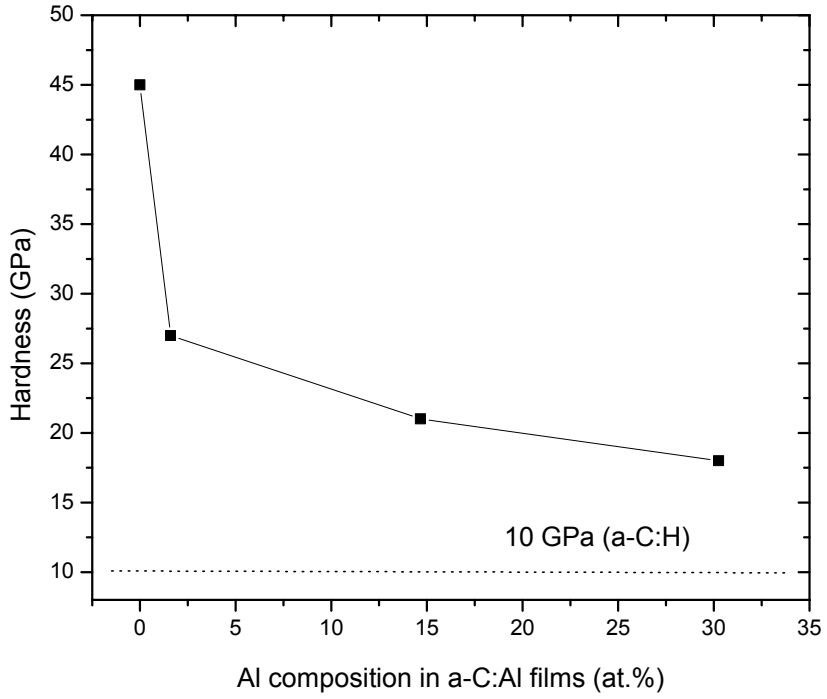

Figure 4.16 The hardness of a-C:Al films with different Al composition

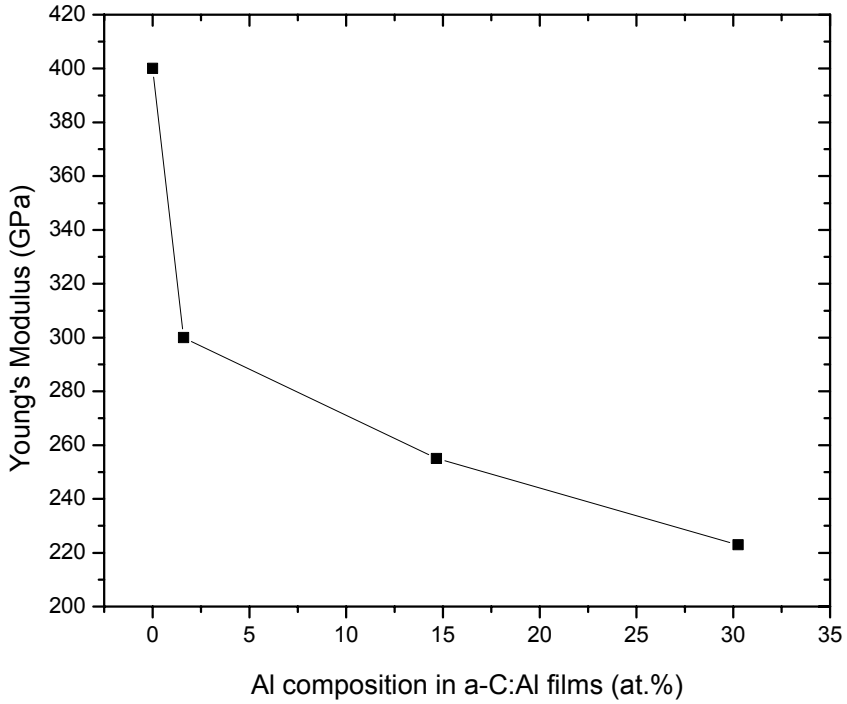

Figure 4.17 The Young's modulus of a-C:Al with different Al composition

Figure 4.16and Figure 4.17 show that the incorporation of Al into the films leads to a decrease of hardness and Young's modulus. The relative decrease in hardness and Young's modulus is similar to the reduction of the compressive stress. The hardness drops from 24 GPa to 18 GPa while the Al composition in the films increases from 1.6 to 30.3 at.%. However, the hardness and Young's are still relatively high. The increase in sp^2 composition in a-C:Al films is the main reason for the decrease of hardness and Young's modulus. Same as the stress, the hardness and Young's modulus of a-C:Al films is lower than that of a-C:Ti films.

4.5 Electrical Properties

The electrical resistivity of a-C:Al films with different metal composition in the films is showed in Figure 4.18. By incorporating Al into the film, the electrical resistivity changes significantly from its initial value of 10^8 Ω-cm. It decreases by 7 orders of magnitude.

As discussed, with increase in Al composition, the sp^2 composition in the films increases, resulting in a decrease of the resistivity of the films. For the a-C:Al film with 1.6 at.% Al, the electrical resistivity is around 40 Ω-cm. This is a dramatic change from the 10^8 Ω-cm in the films without Al. Unlike metal containing hydrogenated amorphous carbon (a-C:H:Me) films, it has been reported that its electrical resistivity has a continuous change in the range from 10 to 10^5 Ω-cm with different metal composition [23, 24]. It is believed that the 1.6 at.% Al introduces numerous hopping sites to enable conduction. With further increase in Al composition

to 30.3 at.%, the electrical resistivity decrease to ~ 10 Ω-cm, within the same order of magnitude of a-C:Al film with 1.6 at.% Al. This indicates there is no continuous conducting channel formed and electron hopping is still the mechanism of conduction.

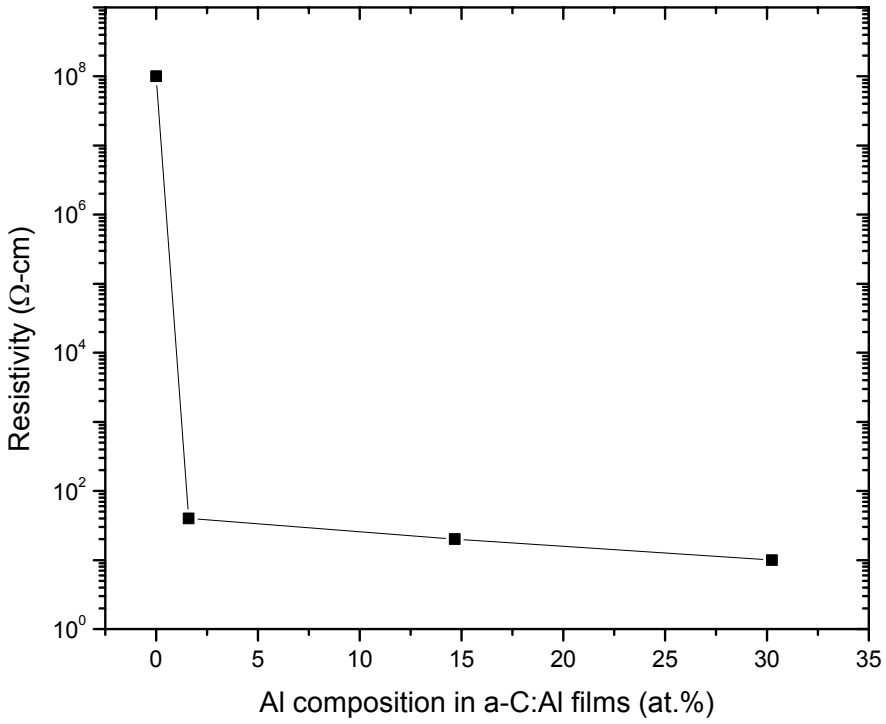

Figure 4.18 The resistivity of a-C:Al films with different metal composition

4.6 Summary

In this chapter, the microstructure, morphology, composition, surface energy, mechanical and electrical properties of the a-C:Al films were investigated in detail. The Al composition in a-C:Al films increases with the increase in Al composition in the composite targets. The Al composition in a-C:Al films has a maximum at –200 V bias. The sp^2 cluster size and composition increases with the increase in metal composition in the targets. The a-C:Al films are sp^3 rich at the mid bias. The surface energy of a-C:Al films is not sensitive to either the Al composition or substrate bias. Al incorporation has been found to be an effective method to decrease the internal stress of a-C films. Electron hopping between sp^2 sites is regarded as the main conduction mechanism of a-C:Al.

Chapter 5. Si Containing Amorphous Carbon Films

5.1 Film Composition and Chemical Bonding States

The film composition of a-C:Si films was calculated by XPS. The chemical bonding state of each element was studied by narrow scan XPS.

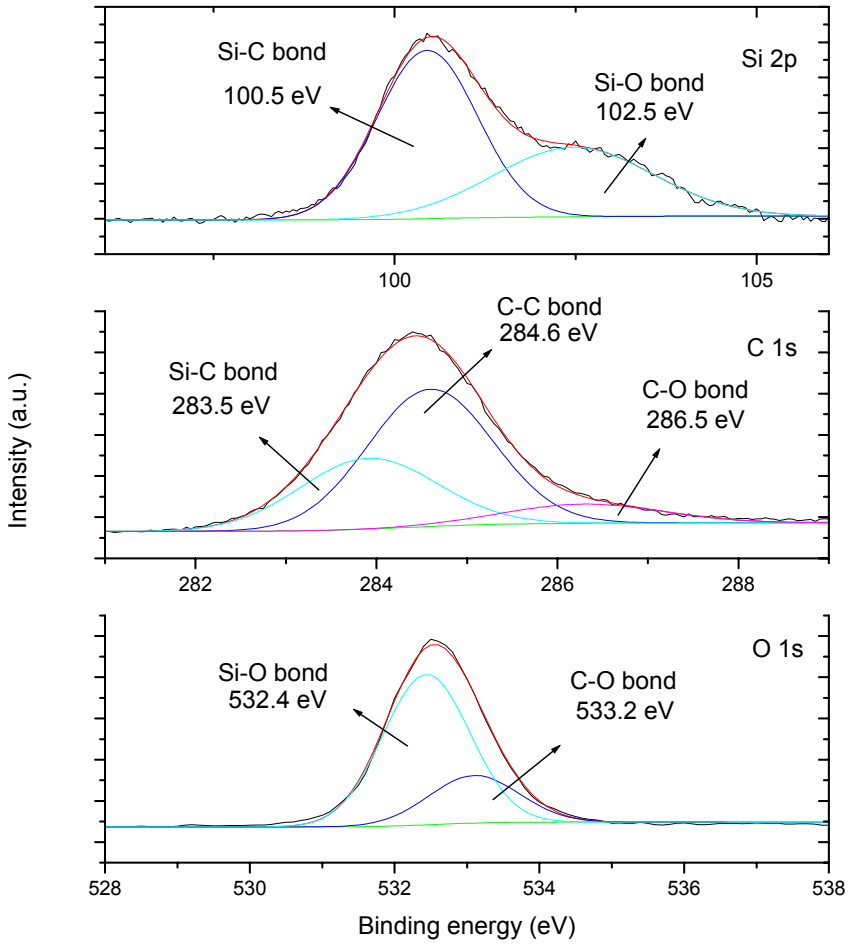

Figure 5.1 Narrow scan of an a-C:Si films deposited from a 5 at.% target at –80 V bias

Typical Si 2p, C 1s, and O 1s XPS spectra of a-C:Si film are shown in Figure 3.1. The Si 2p peak corresponds to the Si-C bond (Si 2p at 100.5 eV) and the Si-O bond (Si 2p at 102.5 eV) [73, 74]. The C 1s peak is presented as three components. The peak around 283.5 eV is assigned to the Si-C bond. The peak around 284.6 eV corresponds to the C-C bond. The peak around 286.5 eV can be attributed to the C-O bond. As for the a-C:Ti and a-C:Al films, oxygen was absorbed from the environment and chemically bonded with Si and carbon when the freshly deposited films were removed from the vacuum chamber.

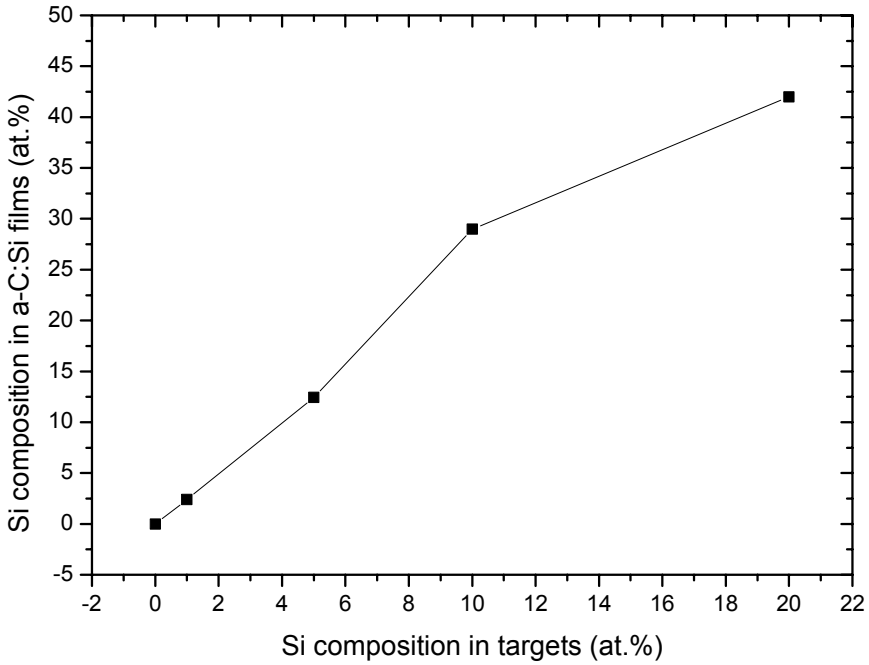

Figure 5.2 The Si composition in films vs. the Si composition in targets

The Si composition of a-C:Si films deposited from different Si composition composite targets is shown in Figure 5.2. The Si composition in the films increases with the increase in metal composition in the targets and is always larger than that in

the targets. This is attributed to two reasons. One is the melting point of Si (~1410°C) is much lower than that of graphite (~3870°C). Hence, the Si particles in the arc spot area are completely sublimated and consequently ionized. But the graphite particles can only be partly evaporated with the formation of macro-clusters and micro-particles, which are trapped by the OPDB filter. The Si ions composition in the plasma is higher than that of composite target.

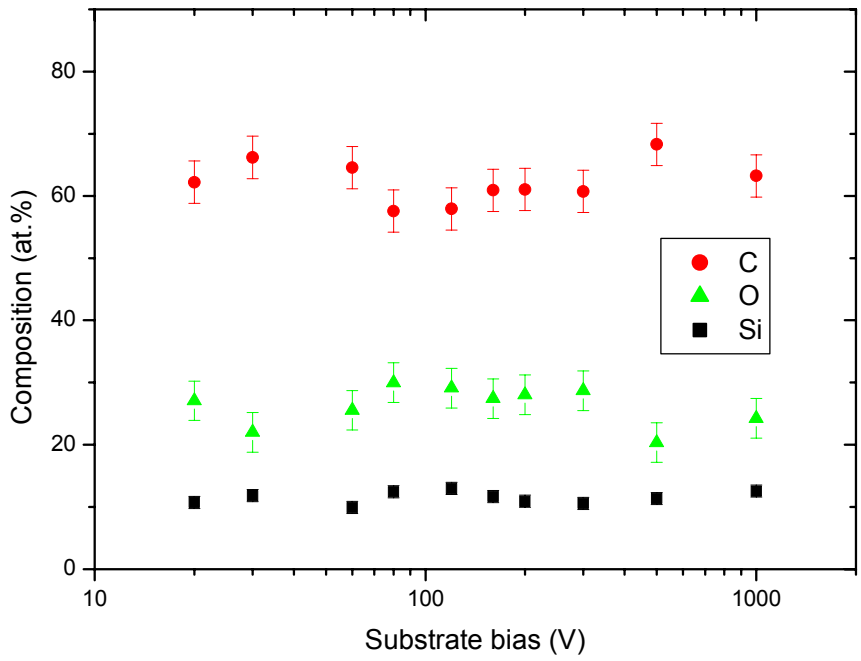

Figure 5.3 The film composition of a-C:Si films deposited at different bias

The films composition of a-C:Si films deposited at different substrate bias was calculated by XPS and the results are shown in Figure 5.3. Unlike that in the a-C:Ti and a-C:Al films, the Si composition of the a-C:Si films deposited at various bias is

relatively constant. The different behavior of a-C:Si films may due to the fact that Si and C belong to the same periodic group and Si is not a metal.

5.2 Microstructure and Morphology

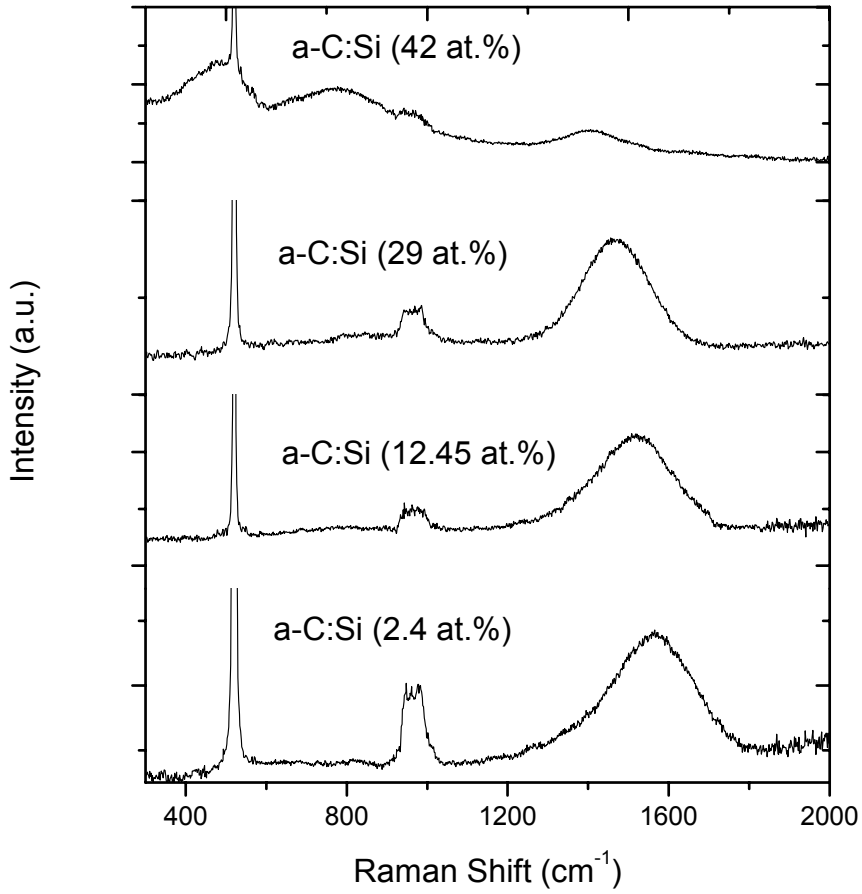

Figure 5.4 Raman Spectra of a-C:Si films

The Raman spectra of a-C:Si films deposited from different metal composition metal/carbon targets are shown in Figure 5.4. In the wavenumber region of 1100-1700 cm^{-1}, there is a broad asymmetric scattering band, which is typical of ta-C films. A strong narrow peak at 520 cm^{-1} and a wide peak around 950 cm^{-1} are the first and

second order Raman vibrational modes of the silicon substrate. For the a-C:Si (42 at.%) film, a broad peak around 780 cm^{-1} and a nonsymmetrical wide peak around 480 cm^{-1} appear. The former one is considered as the vibrational mode of the amorphous silicon carbide cluster [75, 76] and the latter one is due to the amorphous silicon cluster [77].

The Breit-Wigner-Fano (BWF) method was used to fit the above spectra. No D peak is required for the fitting of the a-C:Si films. So the I_D/I_G ratio is zero. This indicates the sp^2 cluster effective size is nearly zero in such films.

The G peak position is shown in Figure 5.5. The great decrease of the G peak position of the carbon cluster can be qualitatively explained as follows. At low silicon concentration, the silicon atom predominately substitutes the carbon atom. As the atomic fraction of silicon in the film increases, more and more silicon atoms substitute the carbon atoms into the ring shaped sp^2-bonded carbon cluster. As the silicon atom is heavier than the carbon atom and the Si-C bond is weaker than the C-C bond, the vibrational energy of the stretching mode of the ring becomes lower and lower.

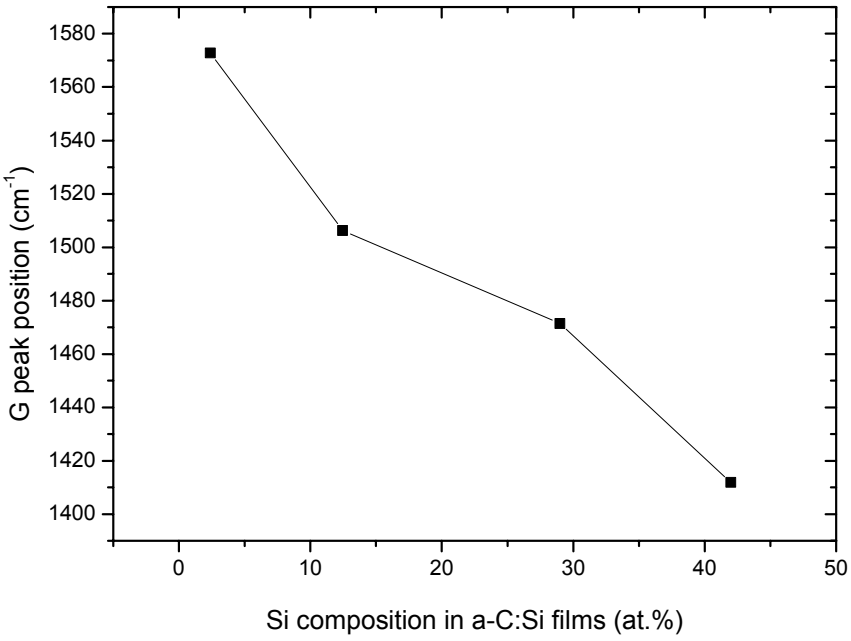

Figure 5.5 The G peak position of a-C:Si films with different Si composition

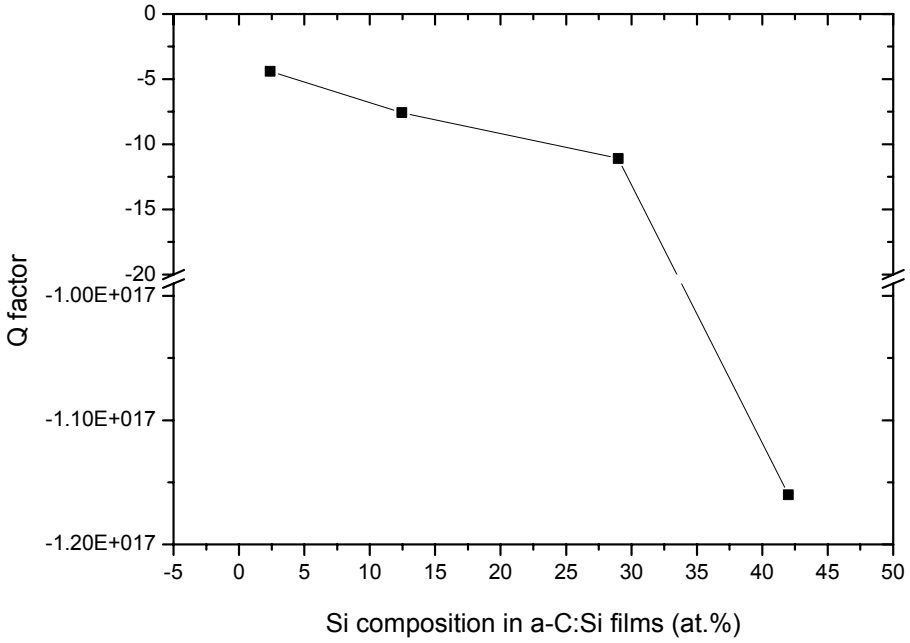

Figure 5.6 The Q factor of a-C:Si films with different Si composition

The Q factor is shown in Figure 5.6. It is believed that the sp^3 composition will decrease with the increase in Si composition. Therefore, the decrease of Q factor is expected. One proof is that the second order Si peak is decrease with the increase in Si composition as shown in Figure 5.4. However, the Q factor is more negative with the increase in Si composition. In the Breit-Wigner-Fano fitting method, the Q factor is a parameter for the symmetric of the peak. This change shows the G peak is more symmetric when more Si atoms substitute the C atoms in the sp^2 clusters. Therefore, the Q factor of a-C:Si films is related to the content of C atoms in sp^2 clusters which are replaced by Si atoms but not the sp^3 composition in the a-C:Si films.

The Raman spectra of a-C:Si films deposited from different Si composition Si/carbon targets are shown in Figure 5.7. The Si second order signal remains relatively constant with the increase in substrate bias from floating to 1000 V. This shows the sp^3 composition of the a-C:Si films is not greatly affected by substrate bias.

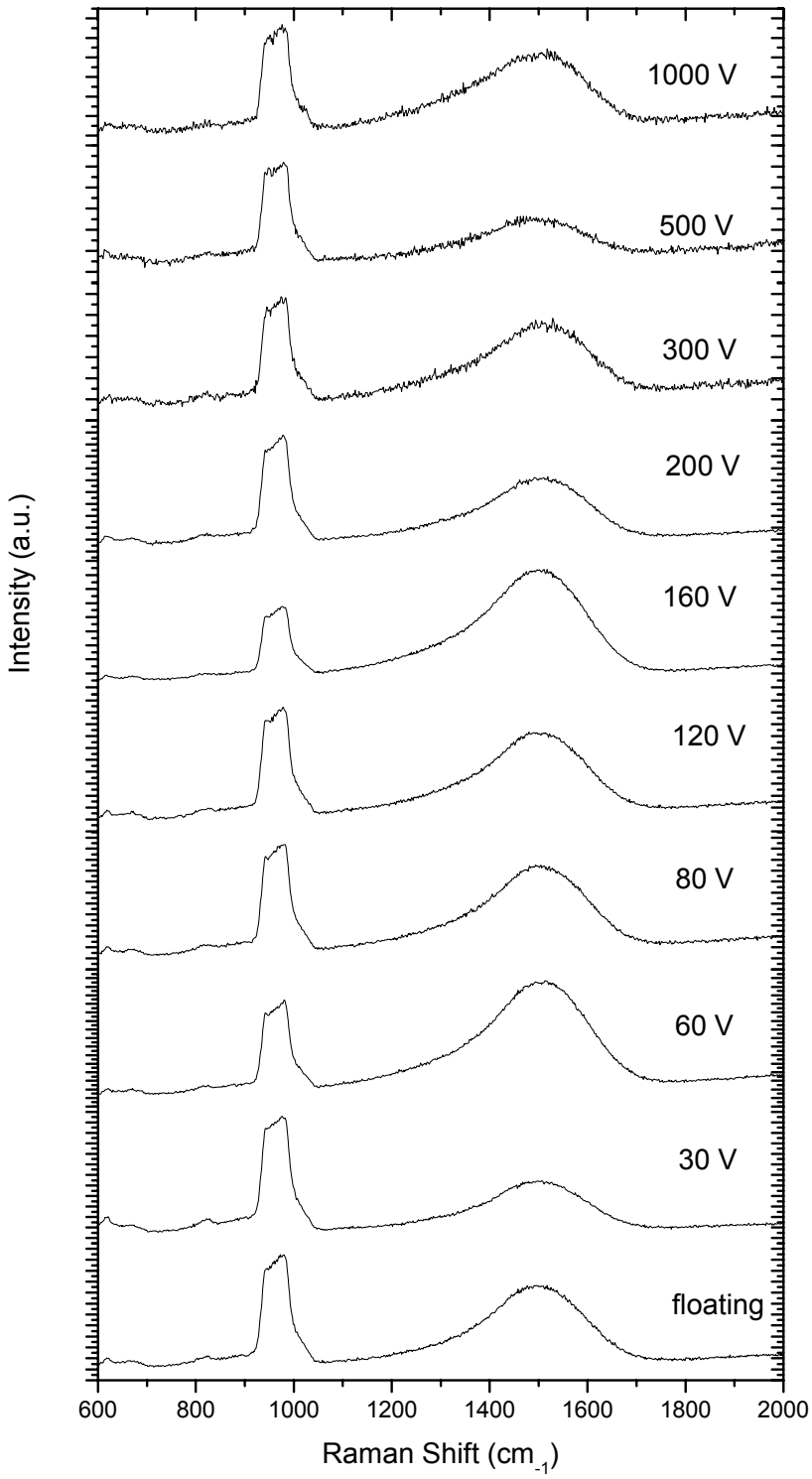

Figure 5.7 Raman spectra of a-C:Si films deposited at different bias

The BWF method was used to fit the broad asymmetric scattering band in the wavenumber region from 1100 to 1700 cm^{-1}. Figure 5.8 shows the Q factor of the a-C:Si films. The Q factor remains constant. It indicates the content of C atoms in sp^2 clusters, which are replaced by Si atoms, does not affect by the substrate bias.

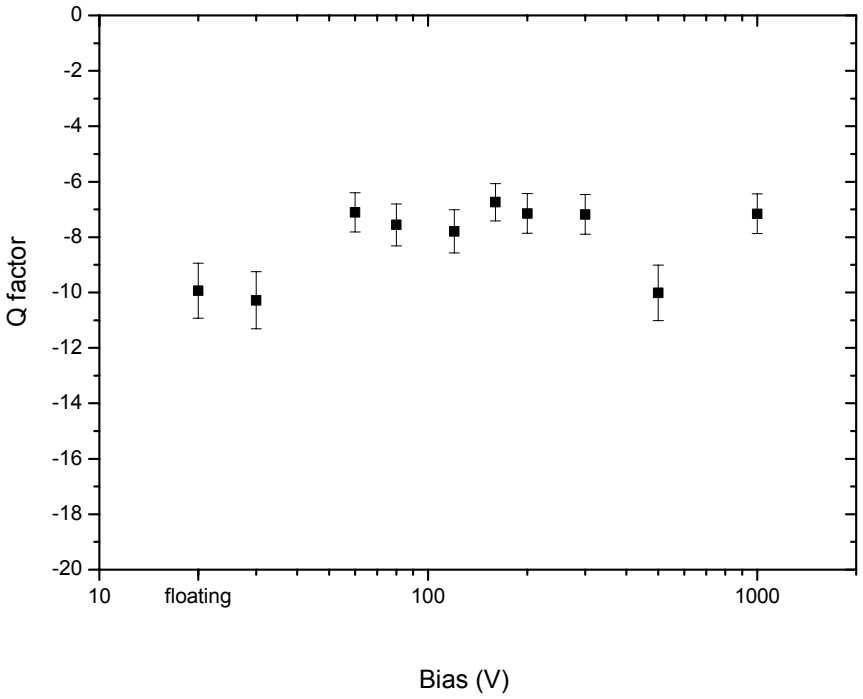

Figure 5.8 The Q factor of a-C:Si films deposited at different bias

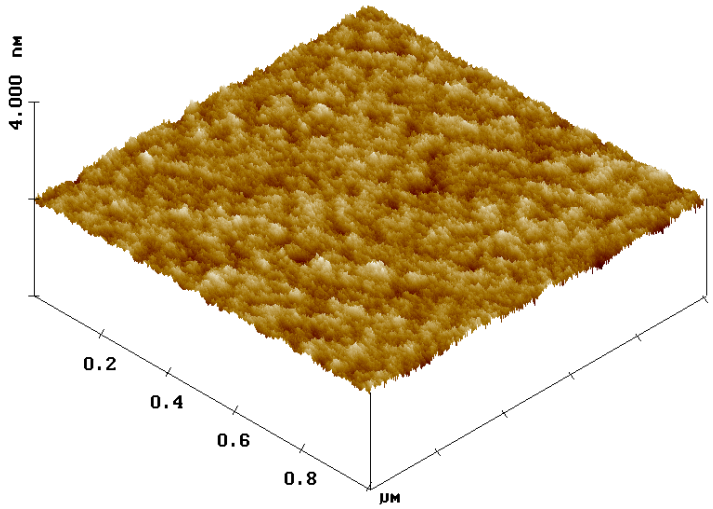

Figure 5.9 A typical AFM image of an a-C:Si film

A typical image of an a-C:Si film deposited from a 5 at.% composite target at –80 V bias is shown in Figure 5.9. The RMS roughnesses of a-C:Si (12.45 at.%) is 0.23 nm. The roughnesses of a-C:Si (29 at.%) and a-C:Si (42 at.%) films are 0.21 nm and 0.17nm respectively.

5.3 Surface Energy

Figure 5.10 shows the measured contact angle for water in contact with a-C:Si films deposited at various bias. The contact angle remains relatively constant, around 65 ^{o}. A typical snapshot of a water droplet on an a-C:Si film is shown in Figure 5.11.

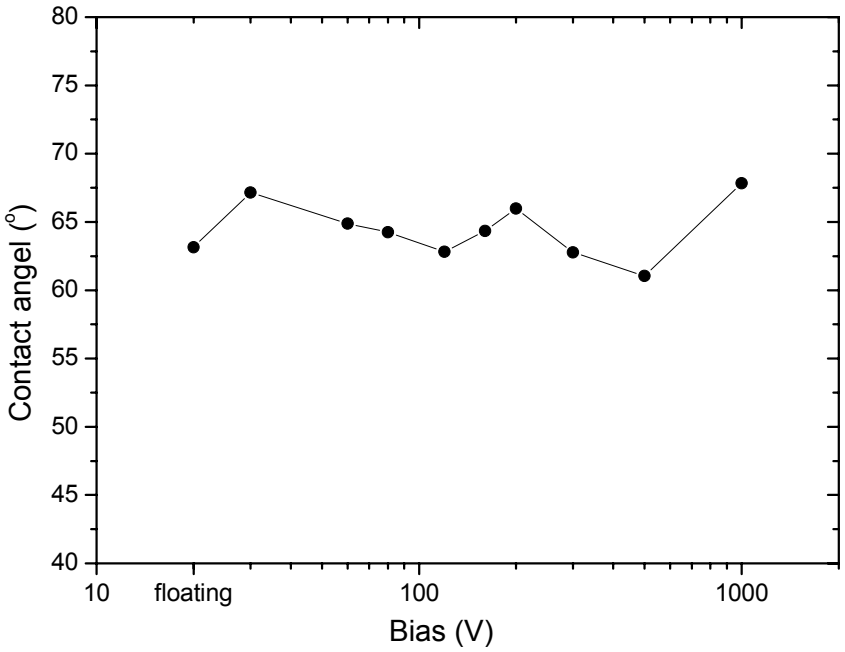

Figure 5.10 The contact angle between water and a-C:Si films as a function of bias

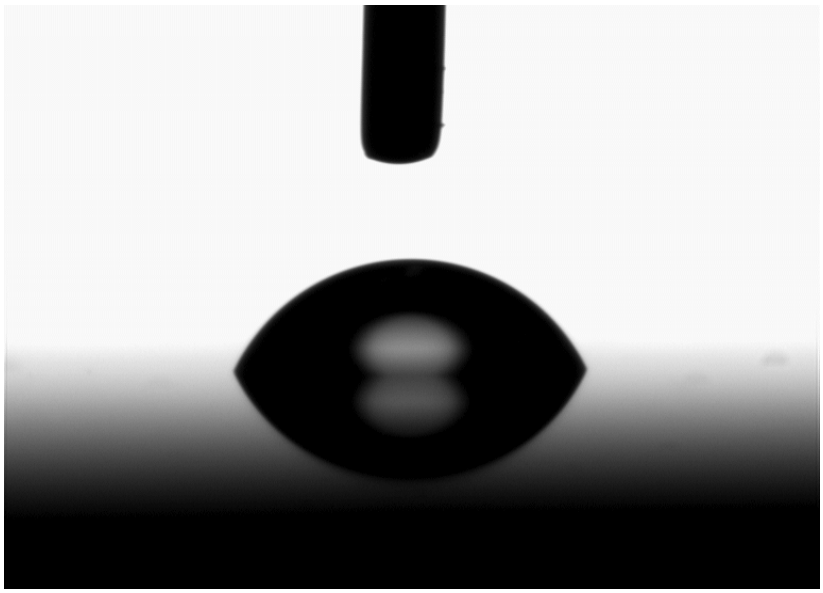

Figure 5.11 A typical image of an a-C:Si film contacting with water

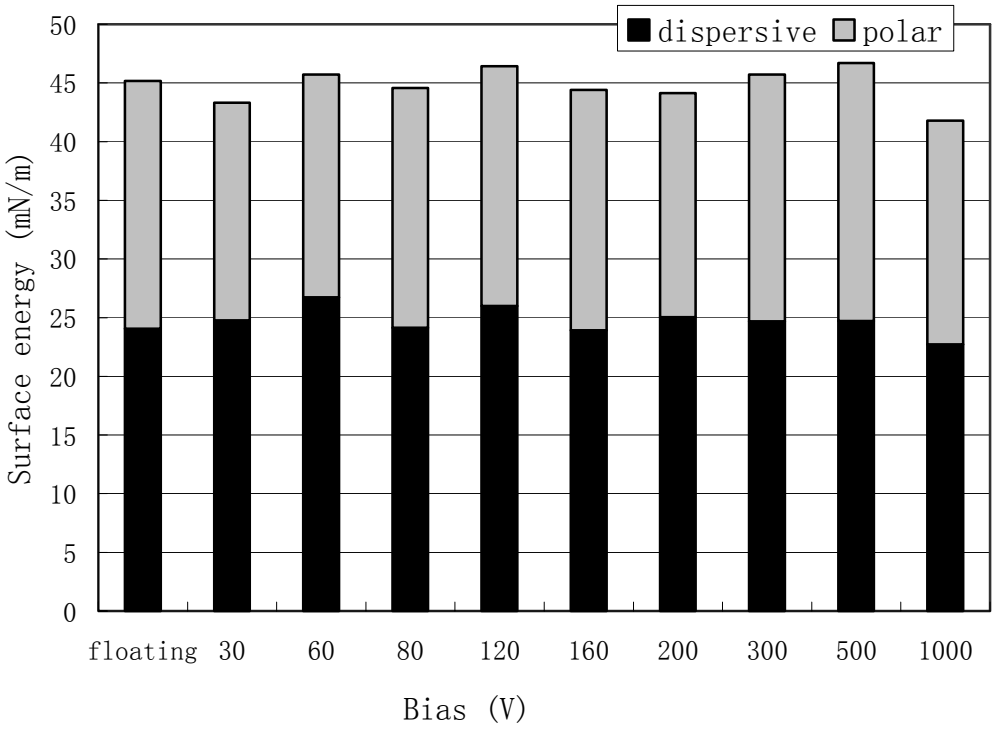

Figure 5.12 The surface energy of a-C:Si films as a function of bias

The surface energy, including both the dispersive and polar components was calculated using the contact angle for three liquids. The dispersive and polar components and total surface energy of the a-C:Si films deposited at various bias are shown in Figure 5.12. Within the experimental error, both the dispersive and polar components of a-C:Si films are independent of the bias. The polar component of the a-C:Si films is as high as 20.13 mN/m. The high polar component leads to the high surface energy. The XPS study shows the Si-O bond, a covalent bond, is formed. The electrons of the Si-O bond is shared by Si and O, it may form some induced dipoles and results in a high polar component.

Unlike in the a-C:Ti film, there is no change in the contact angle for the a-C:Si film under UV irradiation.

5.4 Mechanical Properties

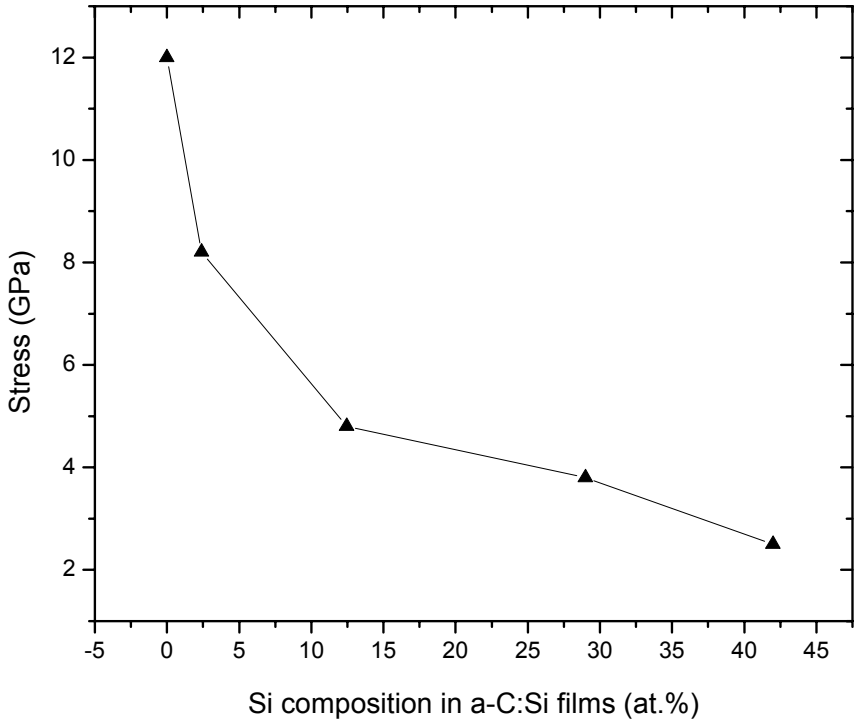

Figure 5.13 The stress of a-C:Si films with different Si composition

Figure 5.13 shows the stress of a-C:Si films as a function of the Si composition in the films. Incorporating Si into films leads to the reduction of compressive stress. The stress drops from 8.2 GPa to 2.5 GPa with the Si composition in the films increases from 2.4 to 42 at.%. The reduction of sp^3 composition is attributed to the reduction of stress.

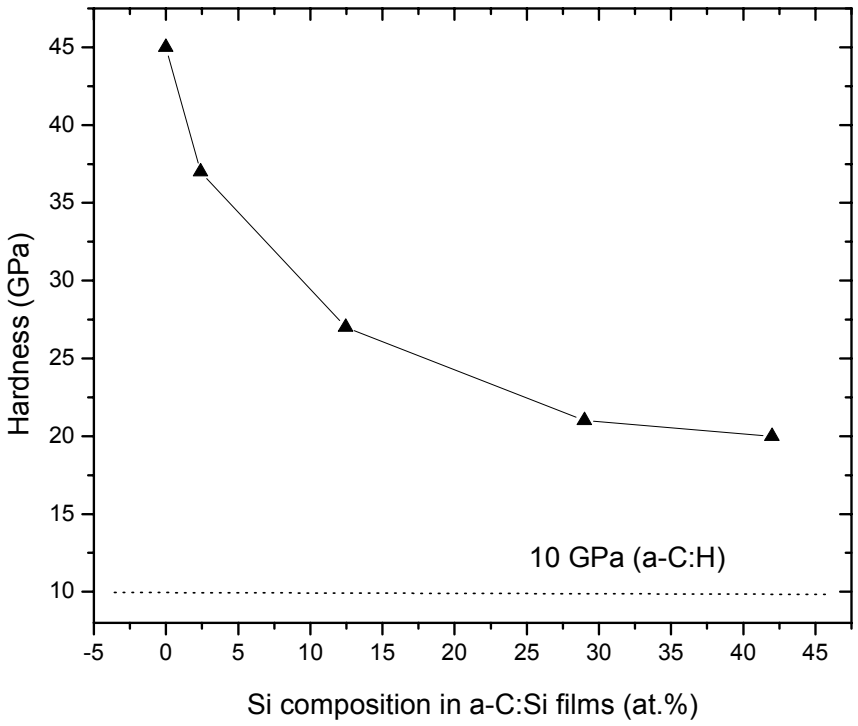

Figure 5.14 The hardness of a-C:Si films with different Si composition

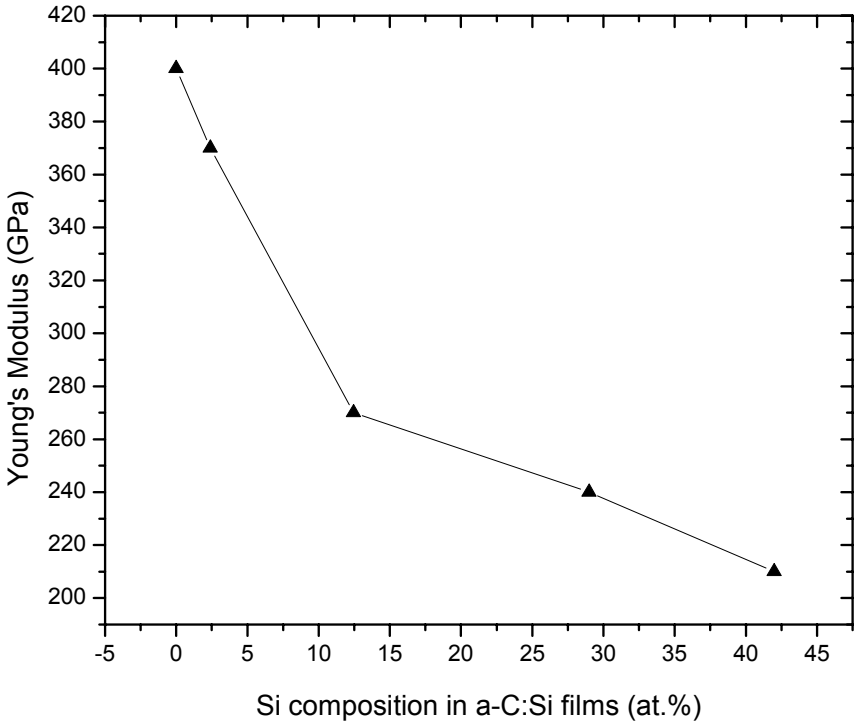

Figure 5.15 The Young's modulus of a-C:Si with different Si composition

Figure 5.14 and Figure 5.15 show that the incorporation of Si leads to the decrease of hardness and Young's modulus of the films. The relative decrease in hardness and Young's modulus is similar to the reduction of the compressive stress. The hardness drops from 37 GPa to 20 GPa when the Si composition increases from 2.4 to 42 at.%. However, the hardness and Young's are still high.

5.5 Summary

In this chapter, the microstructure, morphology, composition, surface energy, and mechanical properties of the a-C:Si films were investigated in detail. The Si composition in a-C:Si films increases with the increase in Si composition in the composite targets. The Si composition in the a-C:Si films is not sensitive to the substrate bias. The surface energy of a-C:Si films is not sensitive to the substrate bias. Si incorporation is an effective method to decrease the internal stress of a-C films. Though such incorporation also results in the decrease of hardness and Young's modulus, their values remains relatively high.

Chapter 6. Ni Containing Amorphous Carbon Films

6.1 Film Composition and Chemical Bonding States

The chemical bonding state of each element was studied by narrow scan XPS.

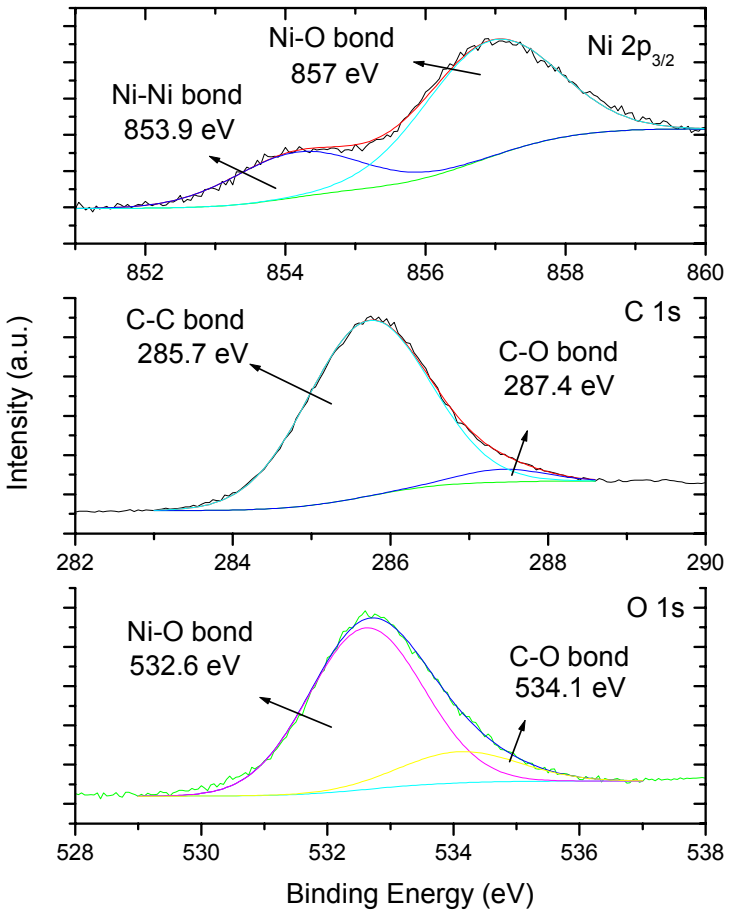

Figure 6.1 Narrow scans of an a-C:Ni films deposited from a 5 at.% target at –80 V bias

Typical Ni 2p, C 1s, and O 1s XPS spectra of a-C:Ni film are shown in Figure 6.1. The Ni 2p peak corresponds to the metal state Ni (Ni $2p_{3/2}$ at 853.9 eV) and the Ni-O bond (Ni $2p_{3/2}$ at 857 eV) [78]. There is no Ni carbide phase. It is believed that oxygen was absorbed from the environment and chemically bonded with the metal and carbon when the freshly deposited films are removed from vacuum chamber. It is known that the bulk Ni is very inert. But the Ni at the surface of a-C:Ni films reacted with oxygen from the environment. This indicates the Ni in the a-C:Ni films is more reactive than the bulk one. The discussion on the TEM and XRD in the next section will show that the Ni has formed nano clusters in the a-C:Ni films. This decreased dimension makes Ni more reactive.

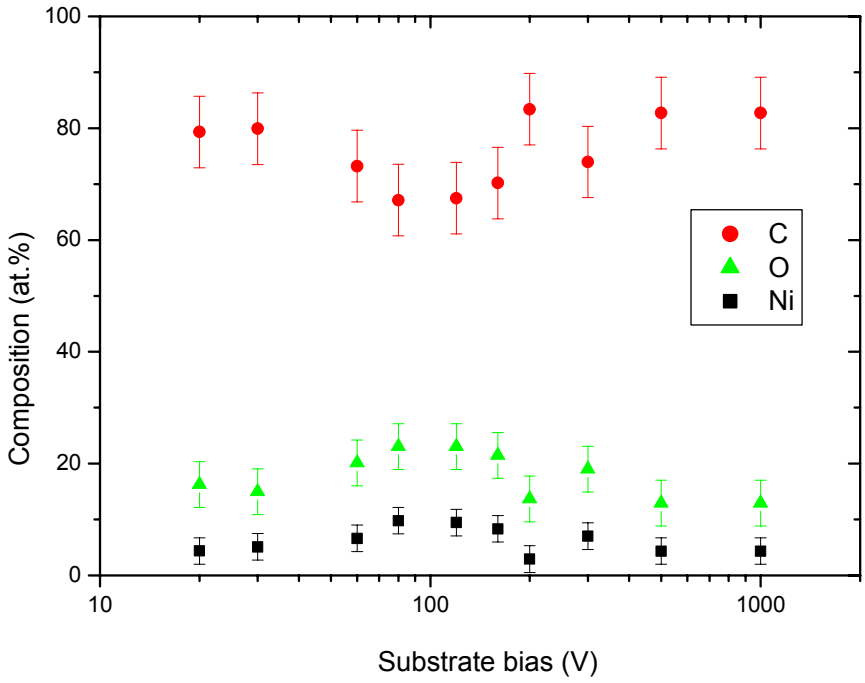

Figure 6.2 Film composition of a-C:Ni films deposited at different bias

The films composition of a-C:Ni films deposited at different substrate bias was calculated by XPS and the results are shown in Figure 6.2. As for the a-C:Ti and a-C:Al films, the Ni composition is larger than that in the targets and has a maximum value at –120 V bias.

6.2 Microstructure and Morphology

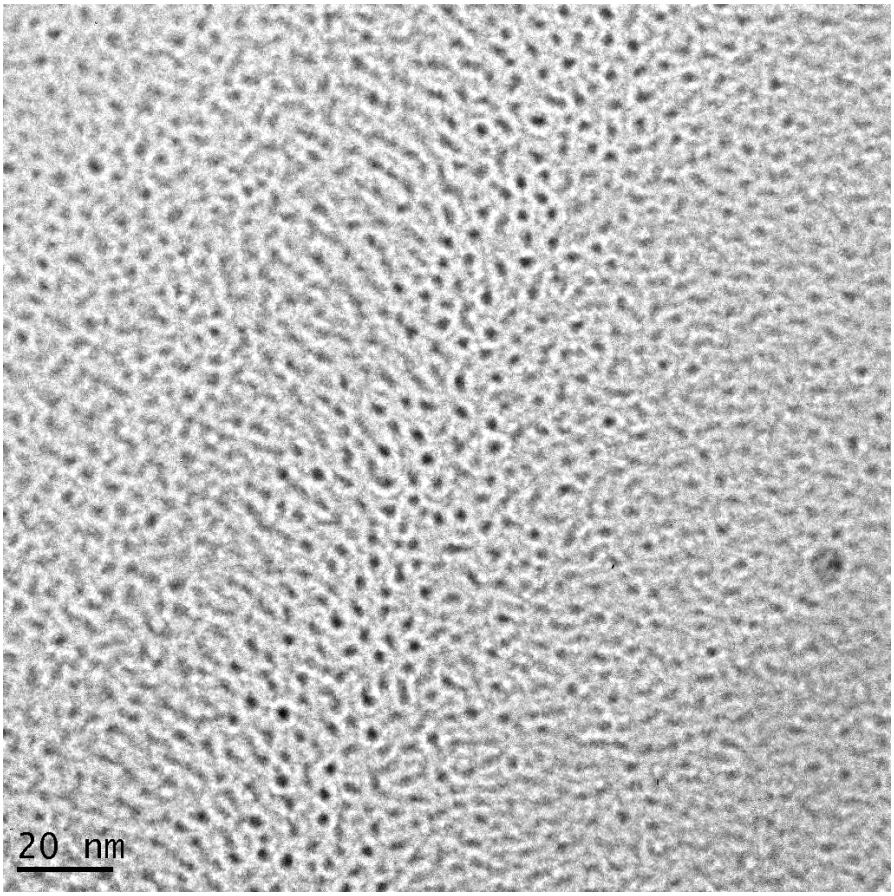

Figure 6.3 The TEM image of a-C:Ni

Figure 6.3 shows the TEM image of an a-C:Ni film. The Ni clusters can be seen embedded in the carbon matrix. The contrast is a result of the higher density of Ni

than that of carbon and hence fewer electrons transmit from Ni region, forming a dark contrast. A higher magnification image was taken on this sample and is shown in Figure 6.4. The Ni clusters are uniformly embedded in the carbon matrix while the carbon exhibits a typical amorphous phase [29, 30]. The diameter of Ni cluster is around 2 nm. This self-assembled nano structure is very interesting and is promising for nano-magnetic or non-linear optical materials.

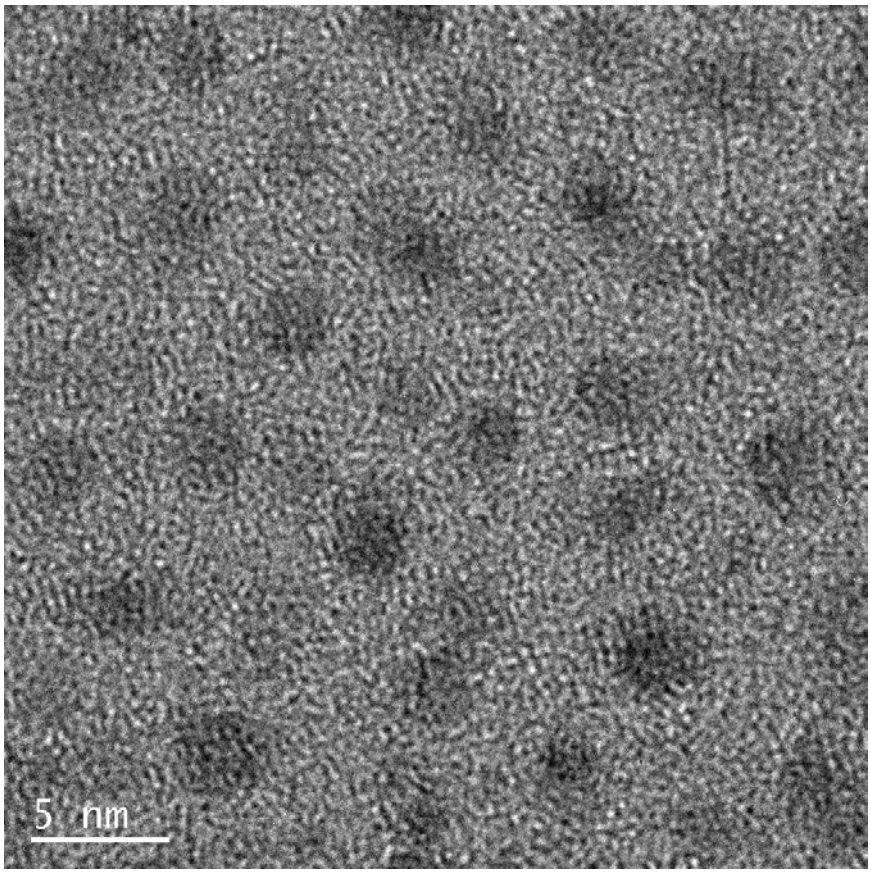

Figure 6.4 The high resolution TEM image of a-C:Ni

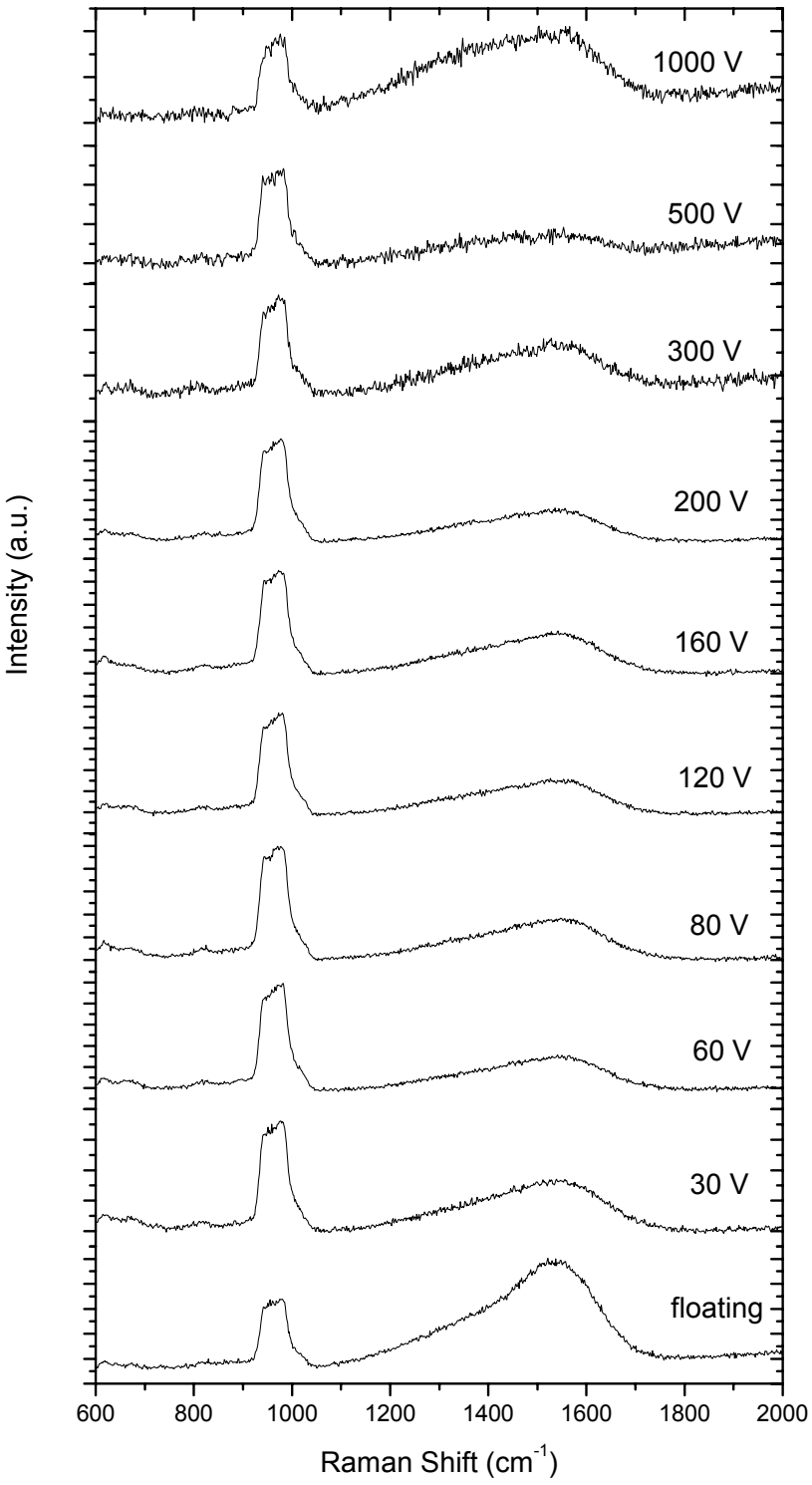

Figure 6.5 Raman spectra of a-C:Ni films deposited at different bias

The Raman spectra of a-C:Ni films deposited from different metal composition metal/carbon targets are shown in Figure 3.9. The peak around 950 cm^{-1} is from the second order vibration mode of the Si substrate. The Si signal remains relatively constant with the increase in substrate bias from floating to 1000 V. Hence the a-C:Ni films are not greatly affected by the substrate bias. The Breit-Wigner-Fano (BWF) method was used to fit the broad asymmetric scattering band in the wavenumber region of 1100-1700 cm^{-1}. Because of the noise in the Raman spectra of a-C:Ni films deposited at –300 V, –500 V and –1000 V, the fittings of the films deposited at –300V and –100V do not converge but reach a minimum and even the fitting of the film deposited at –500 V cannot be achieved. So only the results of a-C:Ni films deposited at bias from floating to –200 V can be discussed.

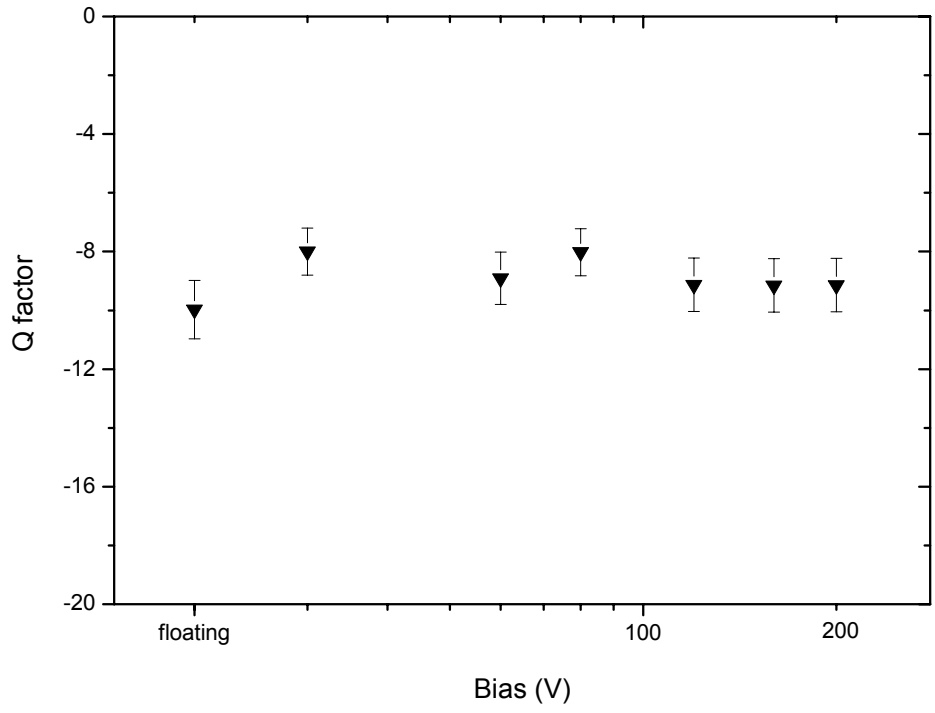

Figure 6.6 The Q factor of a-C:Ni films deposited at different bias

Figure 6.6 shows the Q factor for the a-C:Ni films. Unlike that of a-C:Al and a-C:Ti films, the Q factor of the a-C:Ni films up to – 200 V bias is almost constant. This suggests that applying bias up to 200 V bias does not significantly affect the sp^3 composition of the a-C:Ni films. The a-C:Ni films may have a different growth mechanism due to the formation of Ni nano clusters.

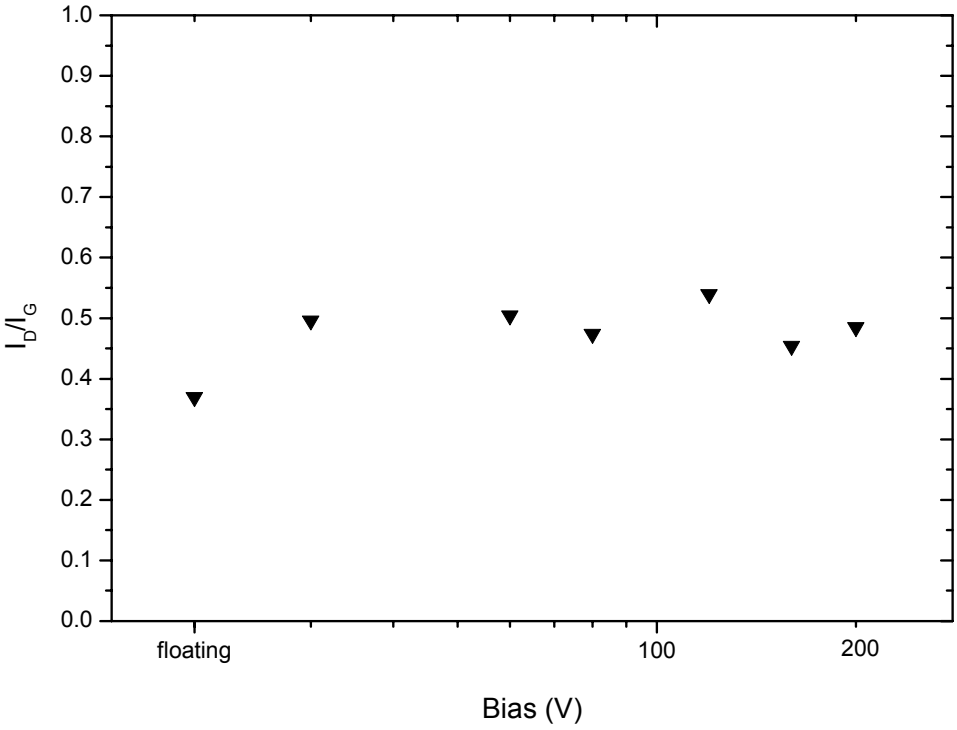

Figure 6.7 The I_D/I_G ratio of a-C:Ni films deposited at different bias

The I_D/I_G was shown in Figure 6.7. The I_D/I_G ratio of a-C:Ni films remains constant (around 0.5). This indicates that the size of sp^2 cluster size is small and the sp^2 cluster size within the a-C:Ni films is not sensitive to the substrate bias.

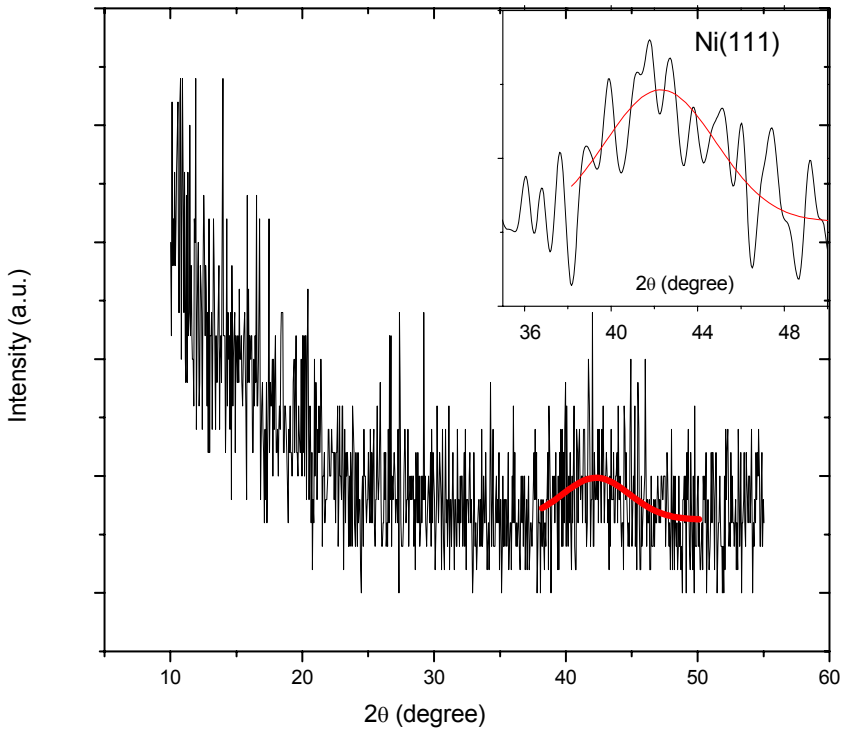

Figure 6.8 The glancing angle XRD spectrum of a-C:Ni films

The XRD spectrum of an a-C:Ni film is shown in Figure 6.8. There is a very broad peak around 42°, which corresponds to the Ni(111) peak [79]. This peak confirms that the Ni clusters present in the carbon matrix as shown in the TEM image. Due to the small size of the Ni clusters, the signal is very weak and nearly blended with the background noise. To analyze this peak, a 10 points FFT method is used to smooth the background noise by Origin 6.0 and one Gaussian shape peak is used to fit it as shown in the right-up corner of Figure 6.8. The fitting result shows the peak center is at 42.2° and the FWHM is 5°. The grain size can be calculated by using the Scherrer's equation [80]:

$$t = \frac{C\lambda}{B\cos\theta} \qquad \textbf{(6.1)}$$

in which λ is the x-ray wavelength (nm), B is FWHM of the peak (radians) corrected for instrumental broadening, θ is Bragg angle. C is a factor (typically 1.0) depending on crystallite shape, and t is the crystallite size (nm). The x-ray wavelength of Cu K_α is 0.154 nm. Using 21.1^o as the Bragg angle and 5/180*π as the FWHM of the peak, the grain size calculated from Scherrer's equation is 1.89 nm. This value agrees with the TEM result.

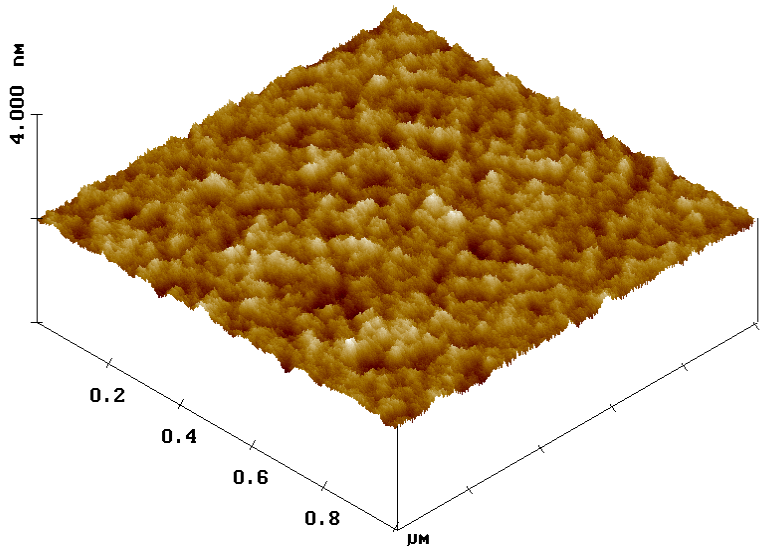

Figure 6.9 A typical AFM image of an a-C:Ni film

A typical image of an a-C:Ni film deposited from a 5 at.% composite targets at –80 V bias is shown in Figure 6.9. The RMS roughness for this film is 0.10 nm.

6.3 Surface Energy

Figure 6.10 shows the contact angle for water in contact with a-C:Ni films deposited at various bias. The contact angle is observed to be relatively constant (around 80 ^{o}) except the one deposited at – 500V,. A typical snapshot of a water droplet on an a-C:Ti film is shown in Figure 6.11.

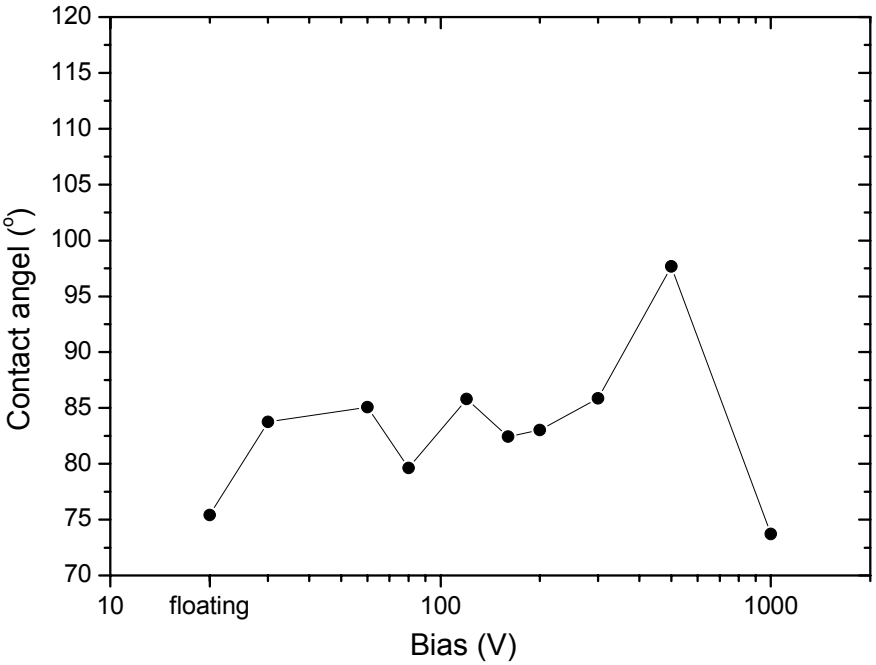

Figure 6.10 The contact angle between water and a-C:Ni as a function of bias

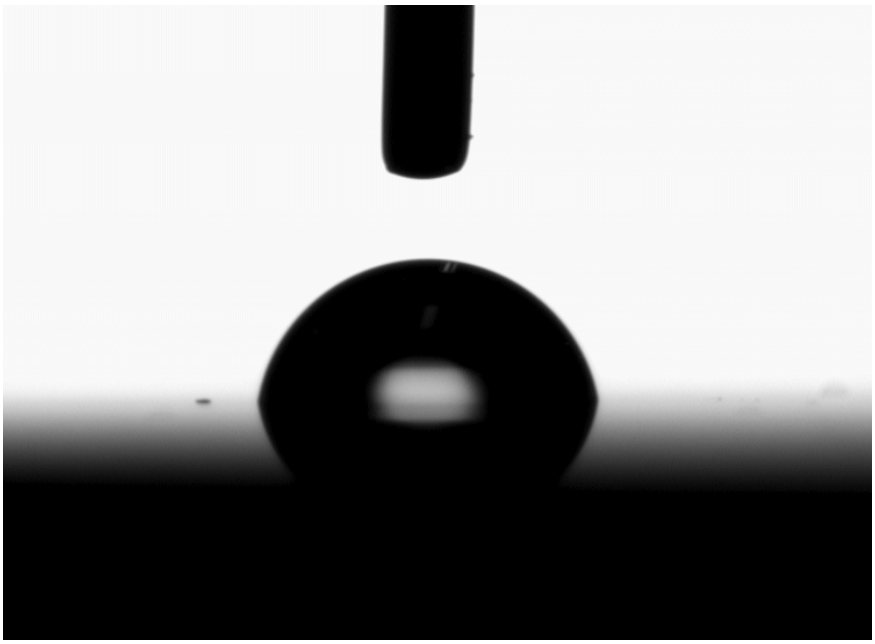

Figure 6.11 Typical image of a-C:Ni film contacting with water

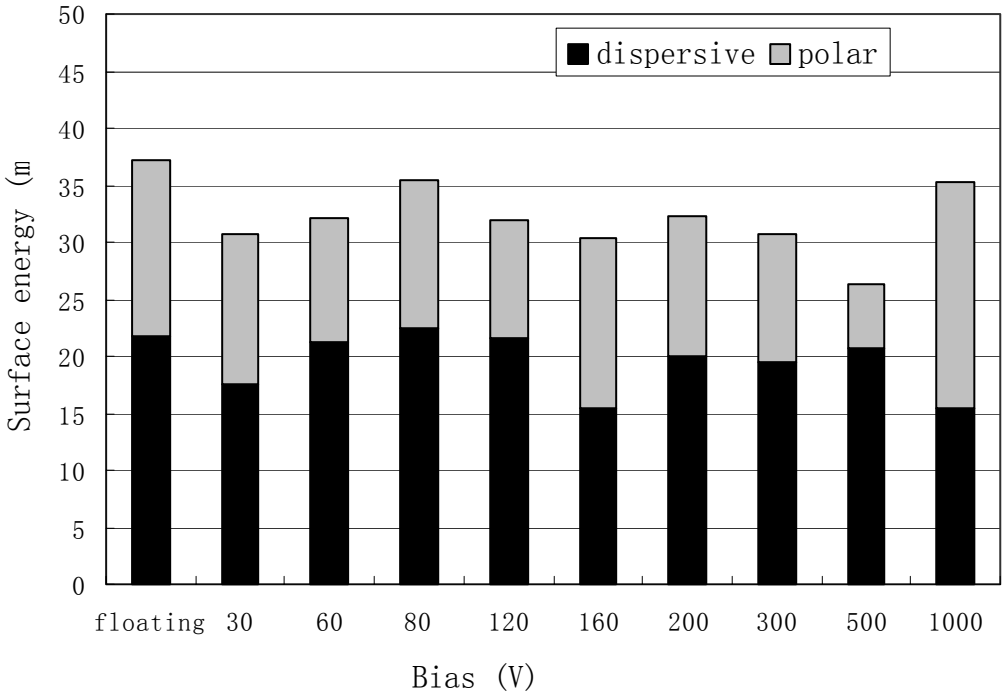

Figure 6.12 The surface energy of a-C:Ni films as a function of bias

The surface energy, including both the dispersive and polar components was calculated using the contact angle for three liquids. The dispersive and polar components and total surface energy of the a-C:Ni films deposited at various bias are shown in Figure 6.12. The polar component of the a-C:Ni films is around 12.6 mN/m. This value is much higher than that of a-C:Al and a-C:Ti films. This is due to the presence of metallic Ni bond. As Ni is only partly oxidized, the oxidization state of each sample can vary a lot from other samples. As a result, the variation of surface energy of a-C:Ni films is more pronounced than that of a-C:Al, a-C:Ti, and a-C:Si films [55].

6.4 Summary

In this chapter, the microstructure, morphology, composition, surface energy, and mechanical properties of the a-C:Ni films were investigated in details. The Ni composition in a-C:Ni films has a maximum at –120 V bias. The sp^3 composition of the a-C:Ni films is not sensitive to the substrate bias. 1.89 nm Ni clusters are found within the a-C:Ni films.

Chapter 7. Discussions on The Metal Containing Amorphous Carbon

7.1 Film growth mechanism

The deposition of a-C:Me mainly contains two processes: a) metal/carbon plasma generation; b) film growth from plasma. From the previous chapters, we observe that the metal composition in film is always higher than that in target, shown in Figure 3.16.

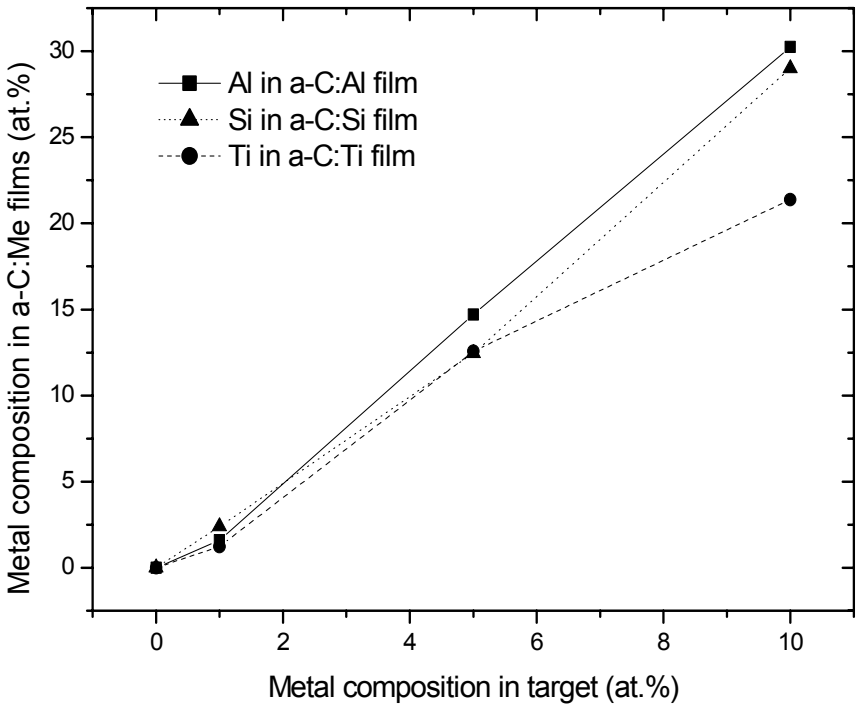

Figure 7.1 The metal composition in film as a function of metal composition in target

Two simple models are proposed and discussed in this section. One is related to the ionized efficiency difference between metal and carbon. Another one is depending on the film growth process from the metal/carbon plasma.

7.1.1 The carbon/metal plasma generation model

During the arc process, target atoms are evaporated at very high spot temperature and become ionized by electrons that are accelerated in the cathode voltage drop [81]. The typical arc spot size is several ten micrometers. There is a temperature gradient from the arc spot center (up to several thousand degree) to the rest water-cooling target [82]. This temperature gradient results in vapor, melting and solid regions existing at the same time. We divide three regions along the radius direction according to the boiling and melting temperature of C for C target, shown in Figure 7.2. In region 1, the temperature is higher than the boiling temperature of C (4827^{o}C [83]). In region 2, the temperature is between boiling point and melting point (3550^{o}C [83]) of C. C is in liquid phase. In region 3, the C is still solid phase. C vapor are formed from region 1 and is ionized to C ions. Due to the plasma pressure, thermo-elastic stress and the soft and fracture properties of graphite, droplets and macroparticles may also generate from region 2 and 3 [81,84].

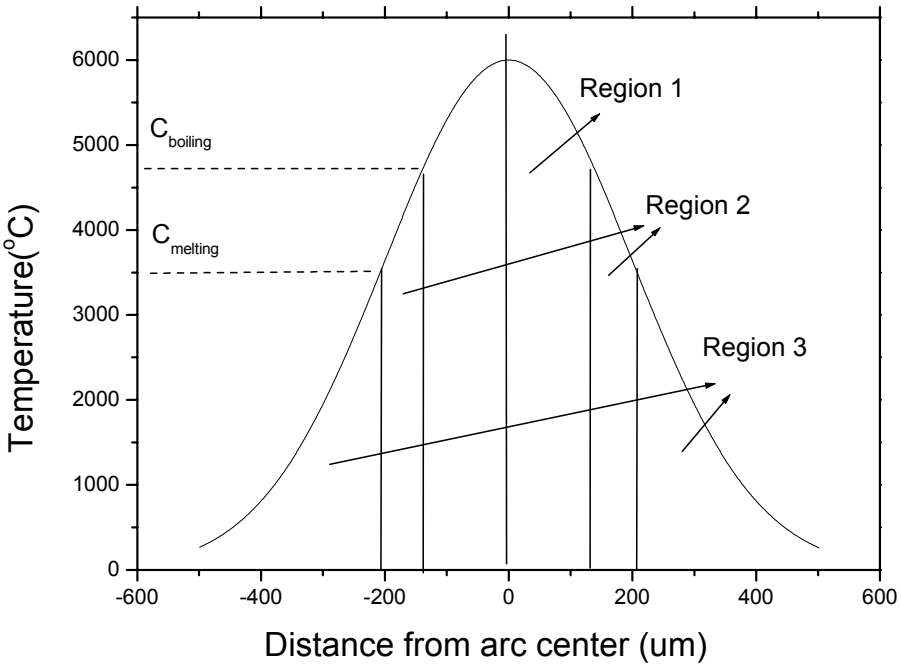

Figure 7.2 The schematic of arc temperature gradient on C target

A C/metal composite target is more complex since the melting point and boiling point of metal is different with C. As shown in Figure 7.3, we use C/Ti target as an example and divide 5 regions for C/Ti composite target. The temperature in region I is higher than the boiling point of both C (4827^{o}C) and Ti (3287^{o}C [83]). C and Ti are both evaporated. In region II, The temperature is higher than the melting point of C and the boiling point of Ti. Ti forms vapor but C is in liquid phase. In region III, the temperature is lower than the melting point of C but still higher than the boiling point of Ti. Ti still forms vapor in this region but C is in solid phase. In region IV, the temperature is lower than the melting point of C and between the boiling point and melting point of Ti. Ti is in liquid phase. In region V, the temperature is lower than the melting point of C and Ti. Both C and metal are in solid phase. From the above

discussion, Ti can form vapor in region I, II and III but C can only form vapor in region I. In region II, III, IV and V, C droplets and particles are generated and only in region IV and V Ti form droplets and particles. As a result the composition of Ti in the Ti/carbon vapor is higher than the target. Consequently the Ti ion concentration of Ti/carbon plasma is higher than the target.

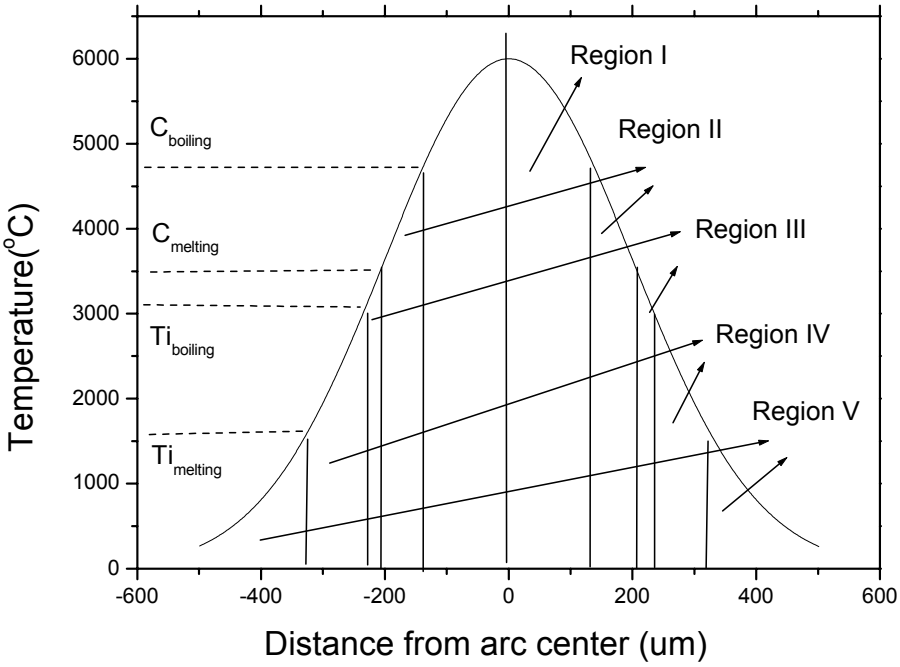

Figure 7.3 The schematic of arc temperature gradient on C/Ti target

Since boiling point of Al (2467°C [83]), Si (2355°C [83]) is lower than Ti (3287°C [83]), then more Al and Si can form vapor. This is one reason for the a-C:Al and a-C:Si having higher metal composition than a-C:Ti.

7.1.2 The film growth model

The subplantation model is well known for the pure amorphous carbon growth. However this is no available model on the metal containing amorphous carbon film growth. We propose a model based on the subplantation model.

First, let's review the subplantation model [85]. The schematic diagram of subplantation model is shown in Figure 1.4.

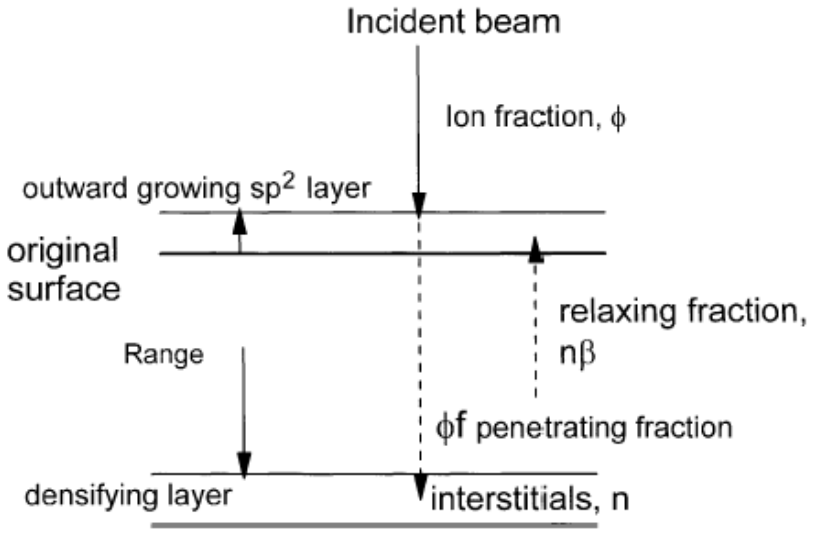

Figure 7.4 Schematic diagram of subplantation process [85]

The model assumes an incident beam of flux F with a fraction ϕ of energetic ions of energy Ei. A fraction f of the ions penetrates the surface. The neutral atoms have no energy and do not penetrate. Thus, a fraction fϕ of the beam penetrates, while the remainder does not penetrate and just stick on the outer surface. A fraction b of the interstitial atoms can relax back to the surface in the thermal spike. This flux is proportional to a driving force, the fraction of interstitials remaining below the

surface, n. In the steady state, the fraction of subsurface interstitials giving densification is n=fϕ-bn. This gives:

$$n = \frac{f\phi}{1+\beta} \quad \textbf{(7.1)}$$

Thus, a fraction n of the beam becomes subplanted inside the film and a fraction 1-n is left on the surface, as sp^2 sites. The subplanted fraction n creates a density increment within the subplanted layer of

$$\frac{\Delta\rho}{\rho} = \frac{n}{1-n} \quad (7.2)$$

Substituting for n gives

$$\frac{\Delta\rho}{\rho} = \frac{f\phi}{1-f\phi+\beta} \quad (7.3)$$

where ρ is the density of sp^2 carbon, Δρ is the density increase. The penetrating fraction is approximated as

$$f = 1 - \exp\left(-\frac{E-E_P}{E_s}\right) \quad (7.4)$$

where E_P is the penetration threshold and E_S is a constant parameter.

The relaxation rate in a thermal spike is

$$\beta = 0.016p\left(\frac{E_i}{E_0}\right)^{5/3} \quad (7.5)$$

in terms of the ion energy Ei and the diffusion activation energy E_0, with p a constant p~1.

The sp^3 fraction is well known rich at ~100eV ion energy. The subplantation model has made a good agreement with the experimental result as shown in figure 1.5. The increase of sp^3 fraction at low ion energy is due to the increase in penetration probability f. The decrease of sp^3 fraction at high ion energy is due to the thermal spike caused by the excess ion energy.

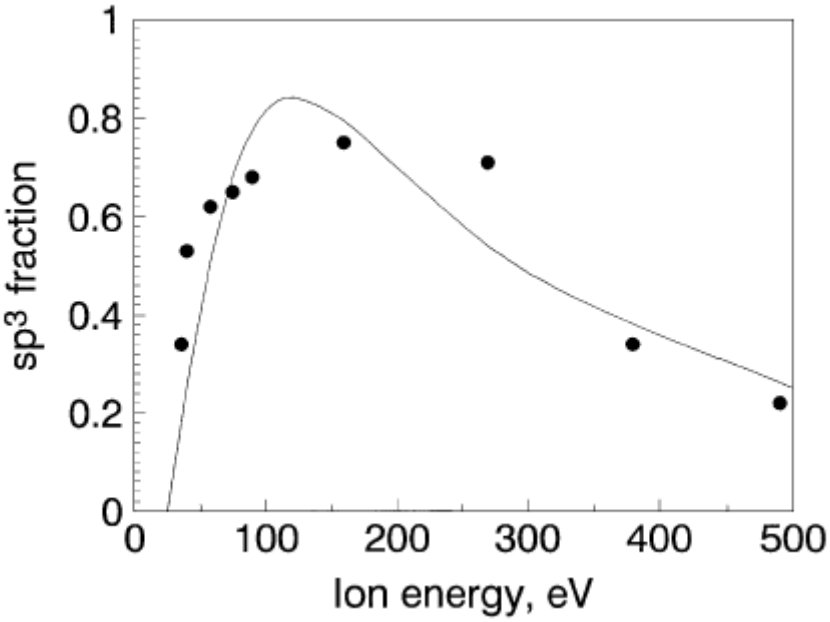

Figure 7.5 Comparison between calculated and experimental sp^3 data by Robertson [85], in which line stand for the simulation curve and dots for experimental data

The growth of C/metal composite film is more complex than the pure carbon film. Both metal and C ions penetrate into the C/metal composite matrix. The metal composition of different metal in a-C:Me films as a function of bias is shown in Figure 1.6. The composition of Al, Ti and Ni increases at low bias side and decreases at high bias side. The “peak” bias for Al is at 200 V while for “peak ” bias Ti and Ni is around 80 to 120 bias. The composition of Al is always the highest and that of Ni is

always the lowest. We have just discussed the effect of melting/boiling temperature difference on the ionized efficient. However, Al (2467°C) and Ni (2372°C) have a similar boiling point. This must not be the main reason for this phenomenon.

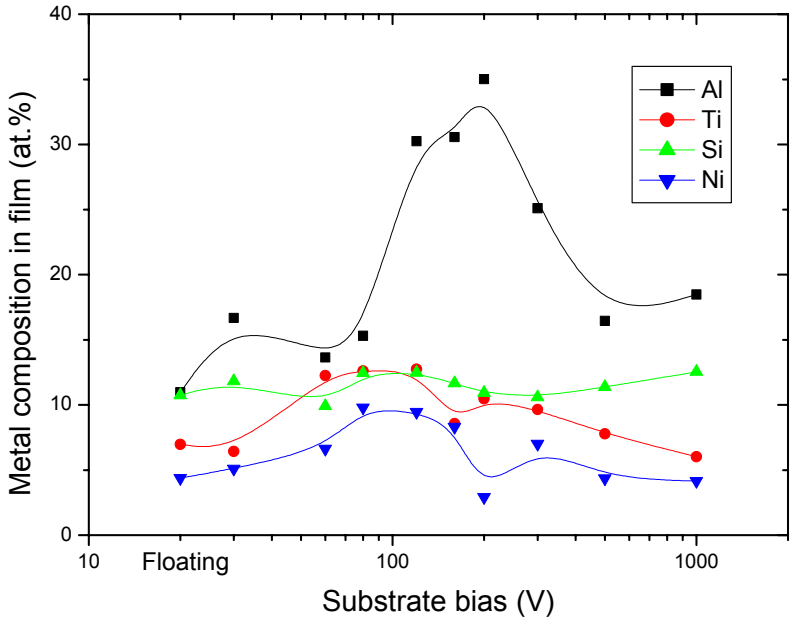

Figure 7.6 The metal composition in films as a function of bias

It is proposed that the metal composition change is mainly due to the subplantation of both metal ions and C ions. With the same ion energy, the small atomic weight ion has a faster speed and can penetrate deeper than the large ions. Therefore at the same bias, the small atomic weight ion is rich in the film. We have seen the Al composition is always higher than Ti and Ni. As the small atomic weight ion has a smaller dimension, the collision cross-section is smaller. Therefore at the same ion energy, smaller thermal spike is generated. We have seen the "peak" bias for Al is at a higher bias than Ti and Ni.

Si is an exception and shows a relatively constant composition as a function of bias. This may due to Si is in the same element group with C. The a-C:Si structure is significantly different from other a-C:Me. As discuss in the Raman study on a-C:Si, Si atoms may substitute the C atoms in C sp^2 network.

7.2 The discussion on the microstructure of a-C:Me

In the pervious chapters, the microstructure of a-C:Me has been studied by Raman spectroscopy. composite targets.

Table 7.1 summaries the Q factor of a-C:Al, a-C:Ti and a-C:Si films deposited from different metal composition composite targets.

Table 7.1 The Q factor of different a-C:Me films

Films:	a-C	a-C:Al (1.6 at.%)	a-C:Al (14.7 at.%)	a-C:Al (30.3 at.%)
Q factor	-17.4	-16.18	-14.95	-6.63
Films:	a-C	a-C:Ti (1.2 at.%)	a-C:Ti (12.6 at.%)	a-C:Ti (21.4 at.%)
Q factor	-17.4	-16.68	-15.76	-3.34
Films:	a-C	a-C:Si (2.4 at.%)	a-C:Si (12.45 at.%)	a-C:Si (29 at.%)
Q factor	-17.4	-4.4	-7.56	-11.1

The Q factor represents the symmetrical of the G peak. In comparison with a-C film, the incorporation of both Al and Ti results in the decrease in Q factor. These reveal

the sp^3 composition of a-C:Al and a-C:Ti films decreases with the increase in metal composition. We just discussed the metal ions subplantation process. The thermal spikes cause the metal diffusion to the surface and affect the final metal composition. These spikes do not only affect the metal atoms, they affect the C matrix in the same time. The metastable sp^3 structure can convert to the stable sp^2 structure. The increase in metal composition causes that more thermal spikes are generated by the metal ions. This is one reason for the decrease of sp^3 composition with the increase of metal composition. Another possible reason is due to the bonding configuration difference between the metal atoms, which embed in the C matrix, the metal atoms limit their neighbor C atoms forming sp^3 bonding configuration. Therefore with the increase in metal composition, the sp^3 composition decreases. The Q factor trend of a-C:Si films is different from a-C:Al and a-C:Ti films. The Q factor is more negative with the increase in Si composition. This shows the G peak of high Si composition a-C:Si film is more symmetric than the one of low Si composition a-C:Si. This is attributed to C atoms in the C sp^2 cluster is substituted by Si atoms. Since Si only has sp^3 bonding configuration, the vibration of C sp^2 cluster containing Si atoms is more symmetric. Thus the G peak of high Si composition a-C:Si is more symmetric than the low Si composition one. Due to the Si is a same group element with C in the period table, a-C:Si always has different properties with other a-C:Me.

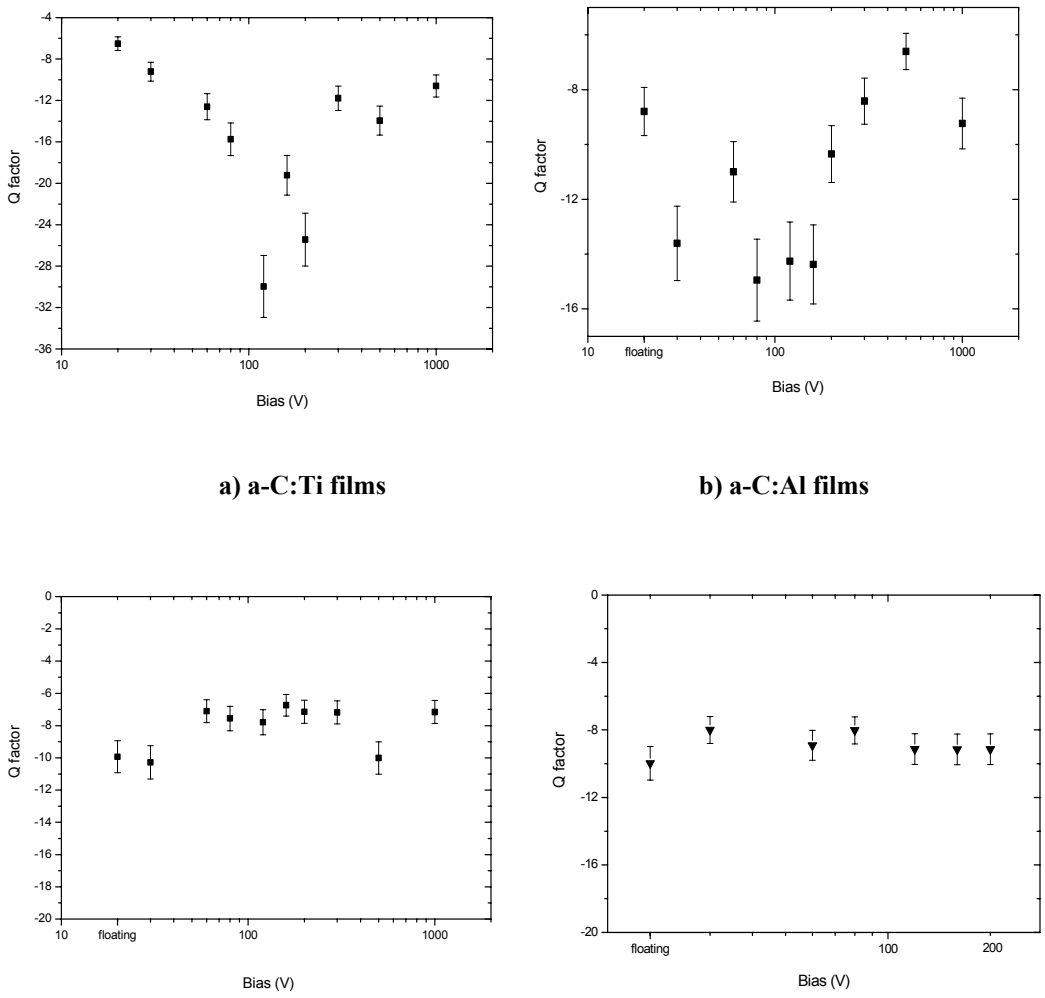

a) a-C:Ti films **b) a-C:Al films**

c) a-C:Si films **d) a-C:Ni films**

Figure 7.7 The Q factor for a) a-C:Ti films, b) a-C:Al films, c) a-C:Si films, and d) a-C:Ni films deposited at different bias

Figure 7.7 shows together the Q factor for different a-C:Me films deposited at different bias. The subplantation mechanism determines that the sp^3 composition of amorphous carbon film is sensitive to the substrate bias. The Q factor of a-C:Ti and a-C:Al films shows the same behavior as pure carbon. However the Q factor of a-C:Si keeps relatively constant. It shows a different behavior from other a-C:Me again. This is attributed to the special properties of Si. A-C:Ni films shows a relatively constant

Q factor up to 200 V bias (No fitting result is acshieved for the a-C:Ni from 300 V to 1000 V bias.). The Ni is a well-known catalyst for sp^2 formation. For example, Ni is one widely used catalyst for carbon nanotube growth. Thus the present of Ni in the growth film may catalyze the surrounding C atoms forming sp^2 cluster. Therefore the sp^3 composition of a-C:Ni is not sensitive to the substrate bias.

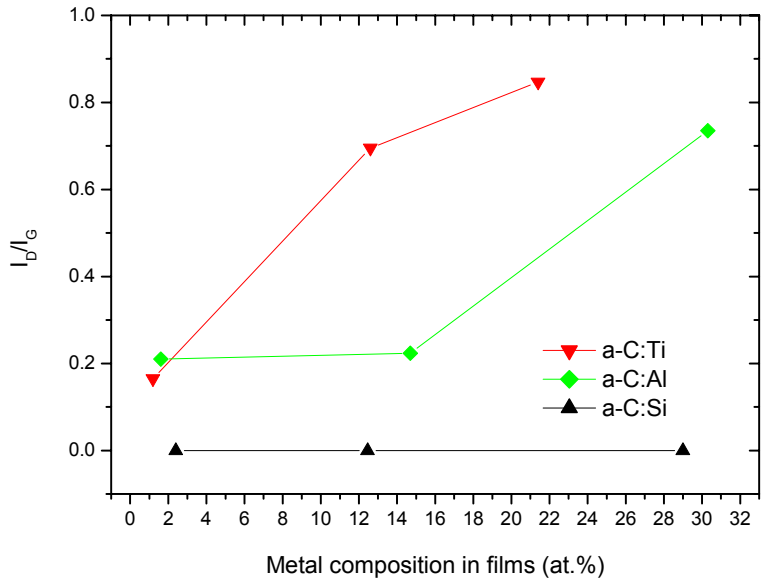

Figure 7.8 I_D/I_G ratio of a-C:Me films with different metal composition

The I_D/I_G ratio of a-C:Me deposited from different metal composition composite targets is shown in Figure 3.7. The I_D/I_G ratio is related to the effective sp^2 cluster size. It is found that no D peak is needed for the fitting of a-C:Si films deposited from Si containing targets. This indicates the sp^2 clusters effectively size is still near zero in a-C:Si films. A D peak is required to properly fit Raman spectra of Al and Ti containing films. The I_D/I_G ratio of a-C:Ti and a-C:Al films increases with the increase in metal composition. This indicates the increase in metal composition causes the sp^2 cluster size increases.

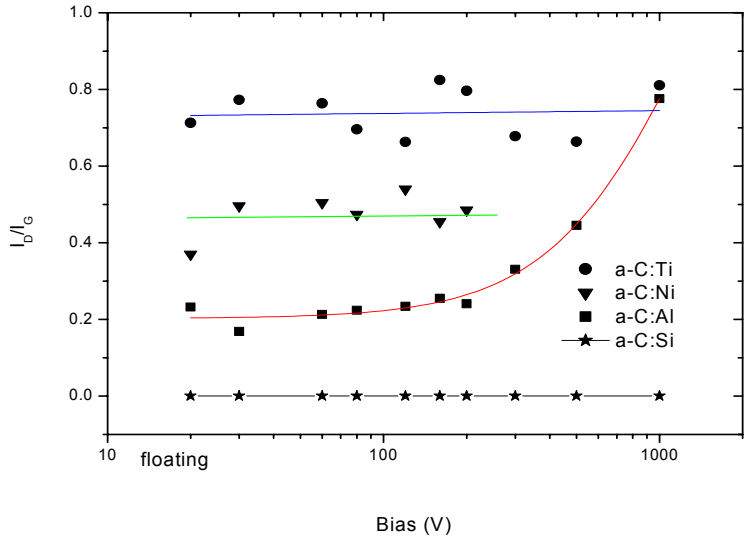

Figure 7.9 I_D/I_G ratio of a-C:Me films deposited at different bias

Figure 7.9 shows the I_D/I_G ratio of a-C:Me films deposited from 5 at.% metal composite targets at different bias. No D peak is need for a-C:Si films, therefore I_D/I_G ratio of a-C:Si films is 0. The I_D/I_G ratio of a-C:Al and a-C:Ni films keeps relative constant from floating to 200 V bias. (No fitting result is acshieved for the a-C:Ni from 300 V to 1000 V bias.) The I_D/I_G ratio of a-C:Al obviously increases from 300 to 1000 V. The I_D/I_G ratio of a-C:Ti is constant from floating to 1000 V bias. This reveals the sp^2 cluster size is not sensitive for all a-C:Me from floating to 200 V bias. The sp^2 cluster size of the a-C:Al films increases with the bias increases from 200 V to 1000 V.

7.3 The discussion on the surface energy of a-C:Me

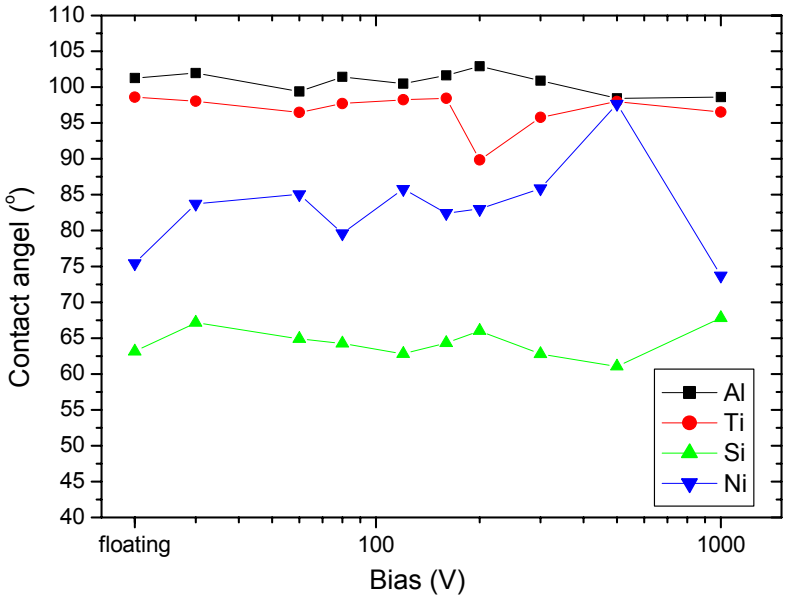

Figure 7.10 The contact angle between water and a-C:Me films as a function of bias

Figure 7.10 summarizes the measured contact angle for water in contact with a-C:Me films deposited at various bias. The contact angle mainly depends on the type of metallic elements.

Table 7.2 The average dispersive (γ_{sv}^{d}) and polar (γ_{sv}^{p}) components and total surface energy (γ) of different metal containing amorphous carbon films

Films	γ_{sv}^{d} (mN/m)	γ_{sv}^{p} (mN/m)	γ (mN/m)
a-C:Si	24.67	20.13	44.80
a-C:Ni	19.58	12.64	32.22
a-C:Ti	21.32	5.86	27.28
a-C:Al	15.21	6.64	21.85
a-C	23.52	12.41	35.93

The average dispersive and polar components and total surface energy of a-C:Me films are summarized in Table 7.2. It has been discussed that the metal-oxide bond plays an important role on the surface energy. Due to the Al and Ti are fully oxidized (electrovalent bond), a-C:Al and a-C:Ti films have a very low polar component. The Si-O (covalent bond) contributes to a high polar component. The dispersive component is related to the film density. An interesting finding is that the dispersive component of carbide-formed a-C:Si and a-C:Ti films is higher than that of noncarbide-formed a-C:Ni and a-C:Al films. The present of carbide phase may result in a higher film density. It is a pity no density measurement has been done in this work. To have a further understanding on the metal incorporation influence on the surface energy, the contact angle between pure metal substrates and water is measured. The contact results between Al, Ti, Ni and Si substrates and water is 93^{o}, 90^{o}, 78^{o} and 52^{o}, respectively. This trend is in a good agreement with the trend of corresponding a-C:Me films and it can be concluded that the type of metallic elements determines the surface energy of a-C:Me films.

The photo inducing reversible wettability of a-C:Ti film has been discussed in detail. Figure 3.21 shows the UV treatment on each film. There is no photo inducing wettability change for the ta-C, a-C:Al, and a-C:Si films. Since no chemical reaction happens on the surface of such films. Beside the reversible wettability of a-C:Ti film, another amazing finding is the UV treatment makes a-C:Ni films more hydrophobic. A possible reason is the UV irradiation made the partly oxidized surface Ni fully oxidized. Due to the time limitation, no XPS data is acquired.

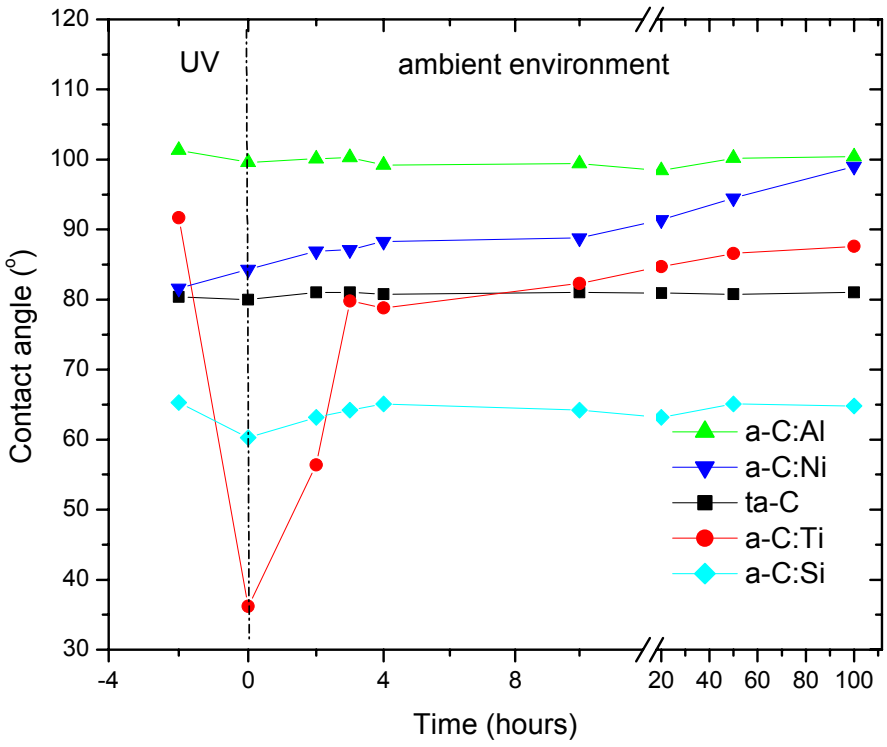

Figure 7.11 The variation of the contact angle of a-C:Me films by UV treatment and stored in ambient environment

7.4 The mechanical properties of a-C:Me

Figure 3.23 summarizes the stress of films as a function of metal composition in a-C:Me films. The incorporating metal leads to the reduction of compressive stress. As discussed, the increase in sp^2 composition is the main reason for the stress reduction. The stress of a-C:Al films is lower than that of a-C:Ti and a-C:Si films containing the same metal composition. The present of carbide phase in a-C:Ti and a-C:Si films is attribute to this result.

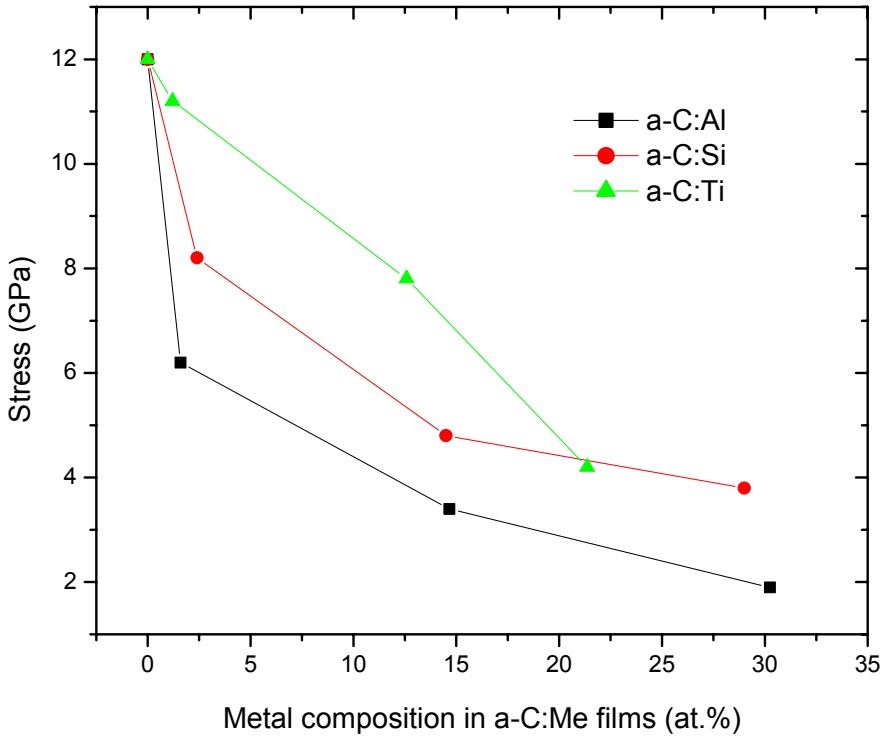

Figure 7.12 The chang in stress of a-C:Me films as a function of metal composition in the films

Figure 3.24 and Figure 3.25 summarize the incorporation of metal leads to the decrease of hardness and Young's modulus of the films. The relative decrease trend of hardness and Young's modulus is similar to the reduction of the compressive stress. The present of carbide phase in a-C:Ti and a-C:Si films results in a compensation of the hardness and Young's modulus reduction caused by the sp^2 composition increasing. Although the hardness of a-C:Al (30.3 at.%) film is the lowest among all films, it is still 18 Gpa. But this hardness is still much higher than the typical hardness of a-C:H film (10 GPa).

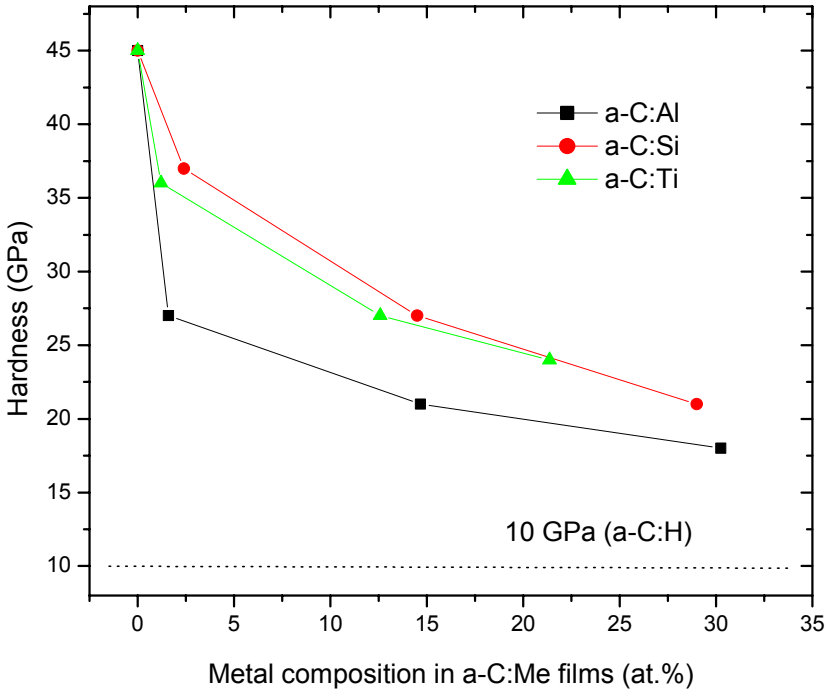

Figure 7.13 The chang in hardness of a-C:Me films as a function of metal composition in the films

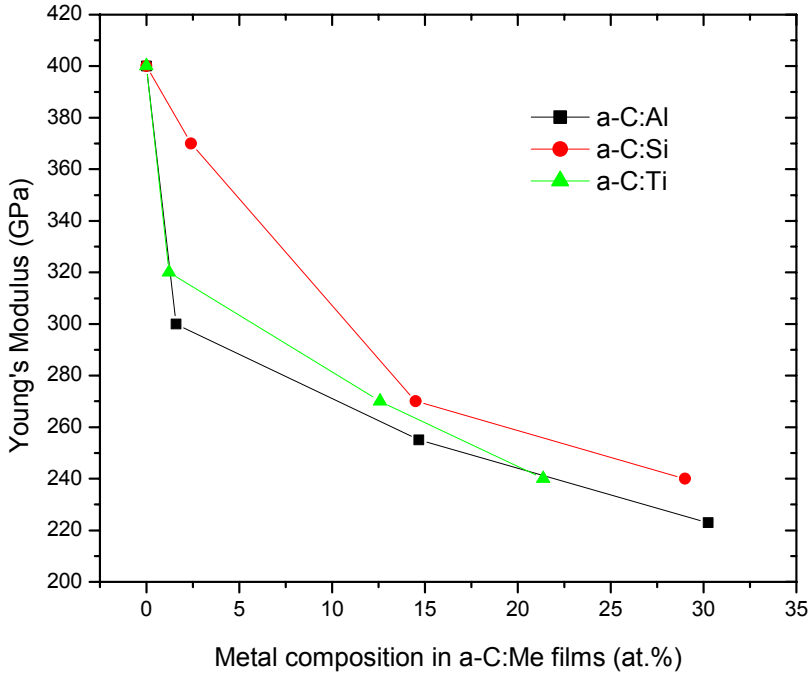

Figure 7.14 The change in Young's modulus of a-C:Me as a function of metal composition in the films

7.5 The comparison between metal containing amorphous carbon and hydrogenated metal containing amorphous carbon

There are a lot of studies on the hydrogenated metal containing amorphous carbon already. It is interests to make a simple comparison between a-C:Me films studied in this work to the references.

7.5.1 The deposition methods of hydrogenated metal containing amorphous carbon (a-C:H:Me)

There are mainly two type of methods to deposit the a-C:H:Me films - plasma-assisted CVD and plasma-assisted PVD techniques [86].

Plasma-assisted CVD technique is using the mixing of metal gas precursors and carbon gas precursors. Generally metal gas precursors are volatile metal halides. The use of these compounds is associated with the problem of corrosion caused by halide compounds to pumping units and hydrophilic compounds that condense on the reactor walls and pipes. The use of organometallic compounds as gas precursors results usually in the incorporation of carbon atoms in the films. But there are no suitable organometallic compounds for some metals. Overall, the plasma-assisted CVD method is limited by many factors.

Plasma-assisted PVD technique is a hybrid of CVD technology to sputtering technology. It offers the advantage over plasma-assisted CVD to use pure metal sources. Thus, the problems associated with metal gas precursors are eliminated. So far, there is no standard system for this technique. Different researchers design their own systems. For example, University of Barcelona, Spain has fabricated a-C:H:Me films in their magnetron sputtering system in the argon/methane mixing gas atmosphere [87, 88]. Nanyang Technology University of Singapore has modified the ECR CVD system with a metal grid as the metal sputtering source [89, 90]. Mo, W, and Ti are successfully incorporated into amorphous carbon films by this system. National Polytechnic Institute of Grenoble, France uses a so-called distributed ECR system to deposit the a-C:H:Me films. The diagrams for two special ECR systems are shown in Figure 7.15.

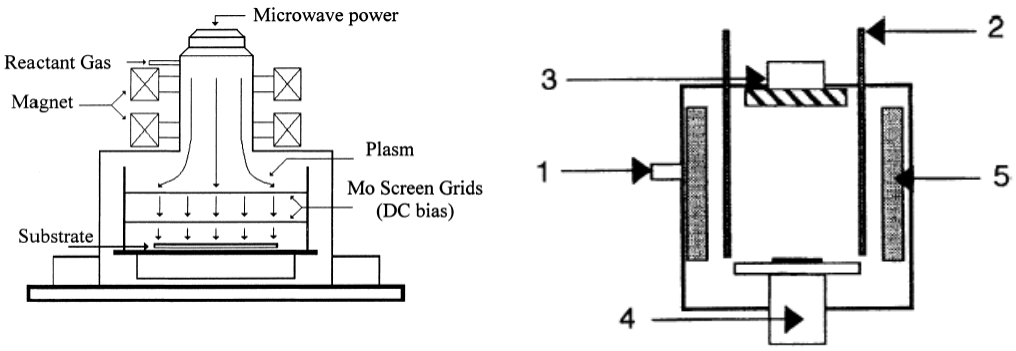

a) the ECR with metal grid **b) the distributed ECR**

Figure 7.15 Schematic drawing of a) the ECR with metal grid and b) the distributed ECR microwave plasma chamber: 1 gas inlet; 2 antenna; 3 copper target; 4 substrate holder; 5 permanent magnets.

Generally, the metal composition of a-C:H:Me films is controlled by the argon to hydrocarbon gas ratio. The ion energy is controlled by the substrate bias.

7.5.2 Mechanical properties

The high mechanical properties are one driving force for people to study the DLC film, especially the application as a protective layer. The elastic modulus of amorphous carbons depends on the rigidity of the individual bonds and the average coordination of the network. The presence of C-H bond make the a-C:H film is not as rigid as a-C film. Therefore the Young modulus and hardness of a-C:H film is much lower than that of a-C film. In both a-C:H and a-C films, the hardness is related to the sp^3 composition. Since it determines the average coordination of the amorphous network. The typical hardness of a-C:H film with optimized sp^3 composition is ~ 15 GPa and the typical hardness of a-C film with optimized sp^3 composition is higher than 40 GPa and can reach up to 80 GPa [91].

In the metal containing amorphous carbon film, two factors determine the hardness. One is the sp^3 composition of the carbon matrix itself. Another is the metal or metal carbide – carbon matrix composite. The carbide has a higher hardness than the a-C:H film. Incorporating carbide forming metals (Ti, W, Mo…) into a-C:H film increases the hardness. Rusli [90] reported that the hardness of a-C:H:Mo can be up to 22 GPa. Incorporating non-carbide forming metals (Cu, Ni, …) into a-C:H film decreases the hardness. Pauleau [86] reported that the hardness of a-C:H:Cu approaches the bulk hardness of Cu - 2.5 GPa with the increase in Cu composition.

As mentioned, the incorporation of metal into a-C film decreases the sp^3 composition. The incorporation of non-carbide forming metal (Al in this work) determinately

decreases the film hardness. However due to the super high original hardness of a-C, the hardness of a-C:Al in this study is still 18 GPa, higher than the typical hardness of a-C:H film. Since the hardness of a-C with optimized sp^3 composition is higher than the carbide, the carbide phase cannot totally compensate the hardness reduction due to the sp^3 composition reduction. The hardness of carbide forming metal (Ti and Si in this work) amorphous carbon film decreases with the metal incorporation. This is different to the a-C:H case. Due to the presence of carbide, the hardness of a-C:Ti and a-C:Si is higher than that of a-C:Al.

7.5.3 Electrical properties

The resistivity of a-C film can up to 10^8 Ω-cm and the resistivity of a-C:H film can up to 10^{10} Ω-cm. The dangling bonds can form the hopping center in the amorphous matrix, in a-C:H film, H atoms passive almost all dangling bonds. Therefore the resistivity of a-C:H can be two orders higher than a-C film.

Several papers report the conductivity of a-C:H:Me film changes over several orders with the increase in metal composition and the thermal activation energy reduces with the increase in metal composition [88, 90]. The conductivity of a-C:Ti in this work shows the same behavior. However, the presence of H affects the thermal stability of a-C:H:Me, Huang [92] mentioned that temperature over 200°C results in an irreversible conductivity change. Huang attributes the dehydrogenation, oxidization, graphitization as the reason. In another word, this is due to the thermal instability of a-C:H:Me film. Since there is no unstable H in a-C:Me film, the thermal stability of a-

C:Me is much better. In this work, the conductivity is measured up to 270°C. Besides the thermal stability, it seems the H does not have a significant effect on the electrical conduction for the metal containing hydrogenated and hydrogen-free amorphous carbon films.

7.5.4 Surface energy

There are very few reports on the surface energy of a-C:H:Me films. One paper simply mentioned the contact angle between the a-C:H:Ti film with water is 107.4° [87]. It is a little higher than the a-C:Ti film in this work (95°). The lower density of a-C:H:Ti film than a-C:Ti film is considered to be the reason.

Chapter 8. Some Applications of a-C:Me Films

8.1 Catalyst for Carbon Nanotubes Growth

Carbon is a unique element because it can assume many structures and forms. These range from hard diamond-like to soft graphite and now molecular fullerenes. Iijima identified carbon nanotubes (CNT) in 1991 [93]. Since there, many laboratories worldwide have begun research in this field. Carbon nanotubes are graphite sheets with hexagonal lattices that are wrapped into hollow cylinders. They have extraordinary structural, mechanical and electrical properties, which derive from the special properties of carbon bonds, their unique quasi-one-dimensional nature, and their cylindrical symmetry [94, 95]. Due to their unique properties, CNTs have a wide range of potential applications. These range from passive filters in composite materials to single-molecular computing elements, single electron transistors, artificial muscles, sensors, and electron emitters for flat panel displays.

To obtain high quality CNTs, the catalyst is a very important factor. As discussed in chapter 6, Ni clusters are uniformly embedded in a-C:Ni films. Therefore it would be interesting to grow CNTs from these a-C:Ni films.

A thermal chemical vapor deposition (T-CVD) system was used to grow the CNTs from the a-C:Ni films. Figure 8.1 shows the aligned CNTs grown from the a-C:Ni films.

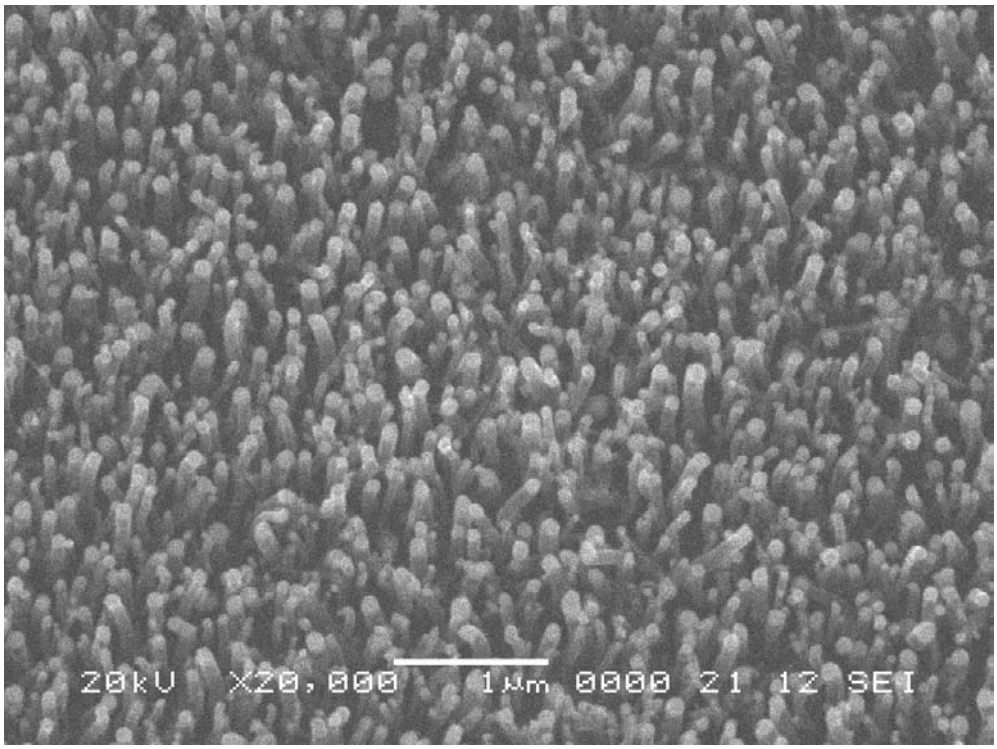

Figure 8.1 CNTs growth from a-C:Ni films

CNTs grown from a-C:Ni films have a controllable diameter, site-density, excellent field emission properties and strong adhesion to the substrate [96].

My colleagues have successfully fabricated prototype field emission displays (FED) using the CNTs growth from the a-C:Ni films as electron emission source as shown in Figure 8.2 and Figure 8.3. The FED uses the same principle as cathode-ray tube (CRT). Electrons are emitted and accelerated through the vacuum and then hit the phosphorus layer, which converts the energy of electrons into light.

Figure 8.2 The prototype FED (static)

Figure 8.3 The prototype FED (dynamic)

Currently, the display market is worth billions of dollars and the LCD currently dominates the flat panel display market. Nevertheless, there are limitations, which include the low brightness, small contrast, narrow view angle, and slow response speed. Hence the excellent properties of FED make it a possible candidate to replace the LCD and CRT in the near future.

8.2 Barrier Layer in Bio-MEMS Mould

The bio-medical field will become a leading industry in the 21st century. One of the interesting research areas is the study of drug delivery [97, 98, 99, 100]. There is no need to take tablets several times everyday and one tablet can take effect for a day and up to a few days [101]. In the mean time, the amount of drug delivered is precisely controlled. Even the control of the strength of the drug can be externally controlled (i.e. ultrasonic sound wave) [102].

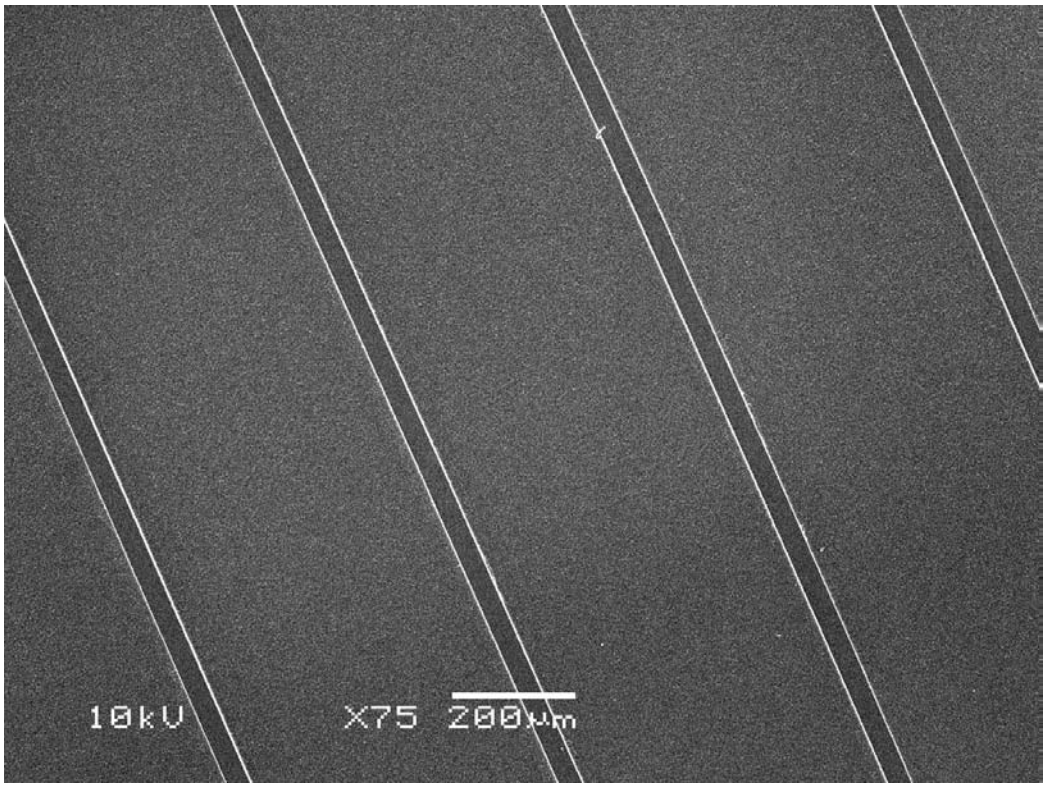

Figure 8.4 The Si mould (Low magnification)

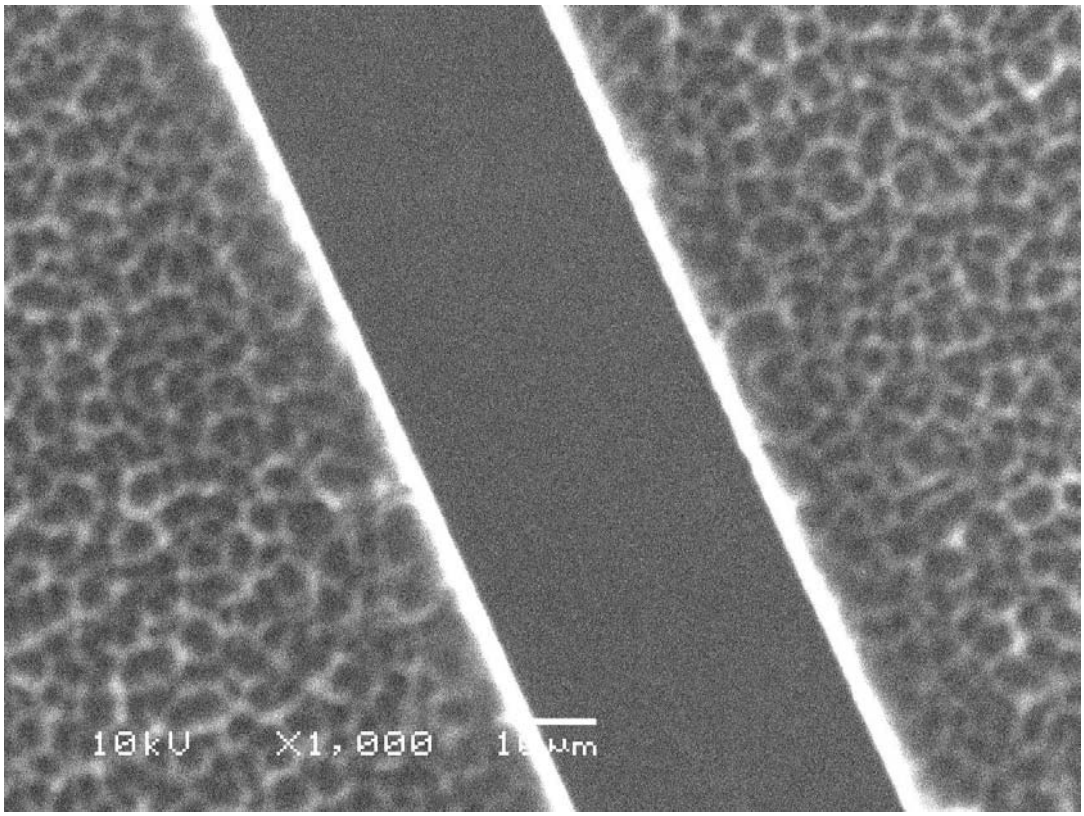

Figure 8.5 The Si mould (High magnification)

In one drug delivery project, a rubber mould was needed to transfer the pattern from a Si mould to the final polymer mould, which would be used to contain cell solutions. One simple approach to fabricate this kind of rubber mould was by using the Si MEMS mould as a template, which was shown in Figure 8.4 and Figure 8.5.

However, due to the high surface energy of Si, the rubber filled into the Si mould sticks to the Si. Since the a-C:Ti films have a very low surface energy with excellent mechanical properties, a 20 – 30 nm a-C:Ti film was deposited on a Si mould as a barrier layer. As expected, the rubber mould was successfully fabricated from the a-C:Ti barrier Si mould as shown in Figure 8.6.

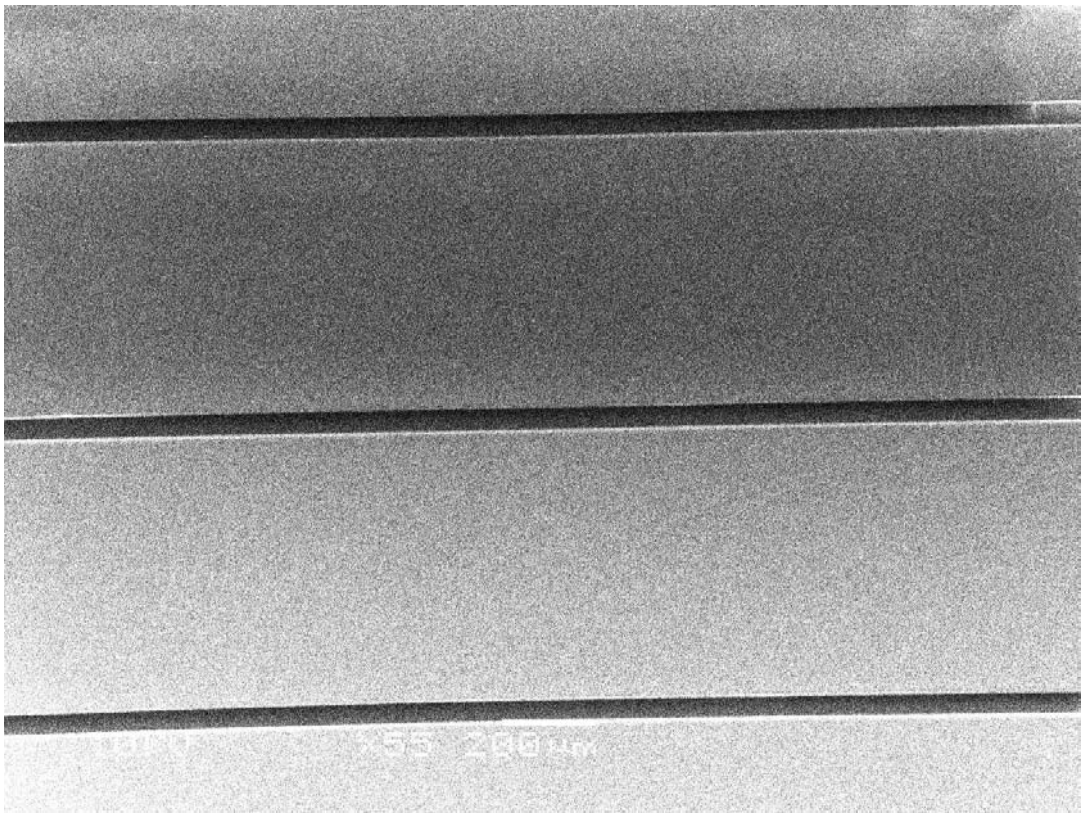

Figure 8.6 The rubber mould (Low magnification)

Some organic polymers with low surface energy were also tested as the barrier layer. Though the rubber mould could be fabricated, the mould failed very fast. It could only be used for less than three times. This is due to their poor mechanical properties. There is no much difference observed for the a-C:Ti barrier Si mould after using it for ten times.

Another advantage of the a-C:Ti films are their excellent bio-compatibility. DLC is known for its biocompatibility and non-toxic [103, 104, 105]. Ti is also a widely used biocompatible material, i.e., Ti-6Al-4V is a widely used bio alloy [106].

It is expected that there will be a big market share for the bio-MEMS. The a-C:Ti film deposited by FCVA technique may play an important role in this industry.

8.3 Summary

In this chapter, two excellent applications of a-C:Me films are presented. Due to their excellent properties, the a-C:Me films can be applied in both information display industry and the MEMS industry.

Chapter 9. Conclusions and Recommendations for Future Work

9.1 Conclusions

Several sets of metal containing amorphous carbon films were successfully deposited by using an FCVA system from metal/carbon composite targets. This deposition technique used fully ionized plasma, free of macro particles. The ions energy could be easily adjusted by the substrate bias. All films exhibit atomically smooth surface.

The metal composition in all a-C:Me films increases with the increase in metal composition in the composite targets and is larger than that in the composite targets. The low melting point of the metals in comparison with C is considered as one major reason. The metal composition in a-C:Al, a-C:Ti, and a-C:Ni films is found rich at middle-bias (80 V for Ti, 120 V for Ni, and 200 V for Al.). However, the Si composition of a-C:Si films deposited at various bias maintains relatively constant. The different behavior of a-C:Si films may due to the fact that Si and C belong to the same periodic group and Si was not a metal. The XPS study also shows the TiC and SiC form in a-C:Ti and a-C:Si films, respectively. There is no carbide phase observed in a-C:Al and a-C:Ni films.

The Raman study shows the sp^2 cluster size and composition increases with the increase in metal composition in the targets. The sp^2 cluster size of a-C:Al film is

sensitive to the substrate bias but not much change for a-C:Ti and a-C:Si is observed. Like ta-C films, the sp^3 composition of a-C:Al and a-C:Ti films has a higher value at middle-bias (80 – 120 V). 1.89 nm nanocrystalline Ni nanoparticles are found in a-C:Ni films

Metal incorporation such as Ti, Al and Si is an effective method to reduce the internal stress of ta-C films. The increase in sp^2 composition in a-C:Me films is the main reason for the decrease of stress. Though such incorporation also results in the decrease of the hardness and Young's modulus, their values remain relatively high (much higher than that of a-C:H films).

The surface energy of the a-C:Me films remains relatively constant with different substrate bias and metal composition. A-C:Al and a-C:Ti films are hydrophobic and a-C:Si films are hydrophilic. The photocatalysis mechanism is used to explain the reversible wettability of a-C:Ti films under UV irradiatoin.

With the increase in metal composition, the electrical resistivity of a-C:Al films decreases from 40 to 10 Ω-cm and the electrical resistivity of a-C:Ti films decreases from 133 to 2.3×10^{-4} Ω-cm. A-C:Ti films shows a small double layer capacitance. The sensitivity of a-C:Ti films to the negative ions solution is much higher than that to the positive ions solution. The sensitivity of the a-C:Ti films decreases with the increase in Ti composition and the electrochemical stability of the low Ti composition films is better. Thus the low Ti composition a-C:Ti film is more promising for electrochemical applications.

Finally, the successful applying a-C:Me films in information display and bio-MEMS fields is demonstrated.

9.2 Recommendations for future work

The a-C:Me films have been shown to have very unique mechanical properties. More applications, such as the application of a-C:Ti films in the bio-MEMS, should be further explored.

The preliminary study on the electrical properties of a-C:Ti films shows its good electrical and electrochemical properties, and this field should be further investigated.

The a-C:Ni films are more interesting than the rest due to the presence of nanocrystalline Ni clusters. It is a pity that due to the time and equipment limitations, the magnetic property of a-C:Ni film has not been characterized. By finding the ways to control Ni clusters size and density will make a-C:Ni films much more useful.

Author's Publications

Journal

1. **P. Zhang**, B.K. Tay, Y.B. Zhang, S.P. Lau, and K.P. Yung, "The reversible wettability of Ti containing amorphous carbon films by UV irradiation", Surface & Coatings Technology, 198 (2005) 184– 188
2. D.H.C. Chua, B.K. Tay, **P. Zhang**, E.H.T. Teo, L.T.W. Lim, S. O'Shea, J. Miao, W.I. Milne, "Vibratory response of diamond-like amorphous carbon cantilevers under different temperatures", Diamond & Related Materials, 13 (11-12) (2004), 1980-1983
3. **P. Zhang**, B.K. Tay, G.Q. Yu, and S.P. Lau, "On the wettability of nanocomposite amorphous carbon films", Journal of Metastable & Nanocrystalline Materials, 23 (2005) 67-70
4. **P. Zhang**, W.M. Tan, B.K. Tay, "Investigation of amorphous silicon-carbon films deposited by filtered vacuum cathodic arc", Journal of Metastable & Nanocrystalline Materials, 23 (2005) 351-354
5. **P. Zhang**, B.K. Tay, G.Q. Yu, and S.P. Lau, "Surface energy of metal containing amorphous carbon films deposited by filtered cathodic vacuum arc", Diamond & Related Materials, 13(3) (2004) 459-464

6. **P. Zhang**, B.K. Tay, and S.P. Lau, "Rapid thermal annealing study on the metal containing amorphous carbon films", Diamond & Related Materials, 12(10-11) (2003) 2093-2098
7. D.H.C. Chua, B.I. Milne, B.K. Tay, **P. Zhang**, and D.X. Zhao, "Microstructural and surface properties of cobalt containing amorphous carbon thin film deposited by a filtered cathodic vacuum arc", Journal of Vacuum Science and Technology A 21(2) (2003) 353-358
8. X.Z. Ding, B.K. Tay, S.P. Lau, **P. Zhang**, and X.T. Zeng, "Structural and mechanical properties of Ti-containing diamond-like carbon films deposited by filtered cathodic vacuum arc", Thin Solid Films 408 (2002) 183-187
9. B.K. Tay, **P. Zhang**, "On the properties of nanocomposite amorphous carbon films prepared by off-plane double bend filtered cathodic vacuum arc", Thin Solid Films, 420-421 (2002) 177-184
10. **P. Zhang**, B.K. Tay, S.P. Lau, and C.Q. Sun, "Microstructure and mechanical properties of nanocomposite amorphous carbon films", Journal of Vacuum Science and Technology A 20(4) (2002) 1390-1394

Conference

1. K.P. Yung, J. Wei, Z.F. Wang, B.K. Tay, **P. Zhang**, "Effects of Catalyst Layer on Carbon Nanotubes Growth", the 1st International Conference on Nanotechnology, Jul 13-17, 2003, Singapore

2. **P. Zhang**, G. Wang, B.K. Tay, and C.M. Li, "The electrochemical behaviour of Ti containing amorphous carbon films", submitted to Diamond & Related Materials, the 9th International Conference on New Diamond Science and Technology, March 26-29, 2004, Tokyo, Japan
3. D. Sheeja, B.K. Tay, **P. Zhang**, J.M. Miao, A. Takada, C.B. Yeo, C. T. Cheng, "Optimisation of DLC Coating prepared on the Side Walls of Si Trenches by a hybrid processing of FCVA and PI3", the 9th International Conference on New Diamond Science and Technology, March 26-29, 2004, Tokyo, Japan
4. **P. Zhang**, B.K. Tay, D. Sheeja, S.P. Lau, D.H.C. Chua, and W.I. Milne, "The study of dynamic balance deposition effect of metal containing amorphous carbon films", International Conference on Metallurgical Coatings and Thin Films 2003, April 28-May 2, 2003, San Diego, California, USA

References

1 S. Aisenberg, R. Chabot, "Ion-Beam Deposition of Thin Films of Diamondlike Carbon", J. Appl. Phys. 42 (1971) 2953

2 J.J. Pouch, S.A. Alterovitz (Eds.), "Properties and Characterization of Amorphous Carbon Films", Mater. Sci. Forum (1990) 52

3 D.R. McKenzie, "Tetrahedral bonding in amorphous carbon", Rep. Prog. Phys. 59 (1996) 1611

4 S.R.P. Silva, J. Robertson, W.I. Milne, G.A.J. Amaratunga (Eds.), "Amorphous Carbon: State of the Art", Proceedings of Specialist Meeting on Amorphous Carbon, 31 July–1 August, 1997, Cambridge, UK, World Scientific, Singapore, 1998

5 J. Robertson, "Properties of diamond-like carbon", Surf. Coat. Technol. 50 (1992) 185

6 M.W. Geis, M.A. Tamor, "Diamond and Diamondlike Carbon", Encycl. Appl. Phys. 5 (1993) 1

7 R. Lo, D.B. Bogy, Technical report on the measurement of nanohardness and elastic modulus of ultra-thin overcoats: effect of W-doping and annealing on the properties of DLC., Department of Mechanical Engineering, University of California, Berkeley, CA 94720: Computer Mechanics Laboratory.

8 V.K. Kudoyarova, A.V. Chernyshov, T.K. Zvonareva, N.B. Dzhelepova, M.B. Tsolov, "Study of diamond-like carbon films for protective coatings", Surf. Coat. Technol. 101(1-3) (1998) 192

9 Y. Lifshitz, "Diamond-like carbon — present status", Diamond Relat. Mater. 8 (1999) 1659

10 Business Wire, April 14, 1998

11 O.R. Monteiro, J.W. Ager, III, D.H. Lee, R. Yu Lo, K.C. Walter and M. Natasi, "Annealing of nonhydrogenated amorphous carbon films prepared by filtered cathodic arc deposition", J. Appl. Phys. 88(5) (2000) 2395

12 A. L. Baia Netoa, R. A. Santosa, S. S. Jr. Camargoa, F. L. Jr. Freirec, R. Cariusd, W. Beyerd and F. Fingerd, "Relation between mechanical and structural properties of silicon-incorporated hard a-C:H films", Thin Solid Films 293 (1997) 206

13 Y. Lifshitz, S.R. Kasi, J.W. Rabalais, and W. Eckstein, "Subplantation model for film growth from hyperthermal species", Phys. Rev. B 41(15) (1990) 10468

14 D.R. Mckenzie, D. Muller, and B.A. Pailthorpe, "Compressive-stress-induced formation of thin-film tetrahedral amorphous carbon", Phys. Rev. Lett. 67 (1991) 773

15 C.A. Davis, "A simple model for the formation of compressive stress in thin films by ion bombardment ", Thin Solid Films 226 (1993) 30

16 J. Robertson, "Deposition mechanisms for promoting sp^3 bonding in diamond-like carbon", Diamond Relat. Mater. 2 (1992) 984

17 H. Windischmann, "An intrinsic stress scaling law for polycrystalline thin films prepared by ion beam sputtering", J. Appl. Phys. 62 (1987) 1800

18 B.F. Dorfman, "Critical parameters of percolation in metal-dielectric diamond-like composites of atomic scale ", Thin Solid Films 330 (1998) 76

19 A. Schuler, C. Ellenbergr, P. Oelhafen, C. Haug, and R. Brenn, "Optical properties of titanium containing amorphous hydrogenated carbon films", J. Appl. Phys. 87 (2000) 4285

20 C. Laurent, D. Mauri, E. Kay, and S.S.P. Parkin, "Magnetic properties of granular Co-polymer thin films", J. Appl. Phys. 65 (1989) 2017

21 W. Luithardt and C. Benndorf, "Deposition of Fe-C:H coatings from a ferrocene precursor in a plasma-activated r.f. process", Diamond Relat. Mater. 4 (1995) 346

22 H.E. Hintermann, "Exploitation of wear- and corrosion-resistant cvd-coatings", Tribol. Int. 13 (1980) 267

23 H. Dimigen, H. Hubsch, and R. Memming, "Tribological and electrical properties of metal-containing hydrogenated carbon films", Appl. Phys. Lett. 50 (1987) 1056

24 C. Laurent and E. Kay, "Properties of metal clusters in polymerized hydrocarbon versus fluorocarbon matrices", J. Appl. Phys. 65 (1989) 1717

25 C. P. Klages and R. Memming, "Microstructure and Physical Properties of Metal-Containing Hydrogenated Carbon Films", Material Science Forum 52&53 (1989) 609

26 O.R. Monteiro, "THIN FILM SYNTHESIS BY ENERGETIC CONDENSATION", Annu. Rev. Mater. Res., 31 (2001) 111

27 M. Chhowalla, Y. Yin, G.A.J. Amaratunga, D.R. McKenzie, Th. Frauenheim, "Highly tetrahedral amorphous carbon films with low stress", Appl. Phys. Lett. 69(16) (1996) 2344

28 Q. Wei, R.J. Narayan, J. Narayan, J. Sankar, A.K. Sharma, "Improvement of wear resistance of pulsed laser deposited diamond-like carbon films through incorporation of metals", Mater. Sci. and Engin. B53 (1998) 262

29 I. Gerhards, C. Ronning, H. Hofsass, M. Seibt, and H. Gibhardt, "Ion beam synthesis of diamond-like carbon thin films containing copper nanocrystals", J. Appl. Phys. 93(2) (2003) 1203

30 B. Feng, D.M. Cao, W.J. Meng, J. Xu, R.C. Tittsworth, L.E. Rehn, P.M. Baldo, and G.L. Doll, "Characterization of microstructure and mechanical behavior of sputter deposited Ti-containing amorphous carbon coatings", Surf. Coat. Technol. 148 (2001) 153

31 A. K. Chaddha, J. D. Parsons, and G. B. Kruaval, "Thermally stable, low specific resistance (1.30×10^{-5} Ωcm^2) TiC Ohmic contacts to n-type 6H-SiC", Appl. Phys. Lett. 66(6) (1995) 760

32 I. Aksenov, V. Belous, V. Padalka and V. Khoroshikh, "Transport of plasma streams in a curvilinear plasma-optics system", Soviet J. Plasma Phys. 4 (1978) 425

33 G.F. You, B.K. Tay, S.P. Lau, D.H.C. Chua, and W.I. Milne, "Carbon arc plasma transport through different off-plane double bend filters", Surf. Coat. Technol., 150 (2002) 50

34 http://www.nanofilm.com.sg/eng/service_ta_c_film.htm

35 X.Z. Ding, B.K. Tay, H.S. Tan, S.P. Lau, W.Y. Cheung, and S.P. Wong, "Preferential orientation of titanium carbide films deposited by a filtered cathodic vacuum arc technique", Surf. Coat. Technol. 138 (2001) 301

36 X. Shi, B.K. Tay, H.S. Tan, Z. Li, Y.Q. Tu, "Properties of carbon ion deposited tetrahedral amorphous carbon films as a function of ion energy", J. Appl. Phys. 79 (1996) 7234

37 Hand book of XPS, J.F. Moulau, W.F. Stickle, P.E. Sobol, K.D. Bomben, Physical Electronics; Reissue edition (February 1995)

38 A.C. Ferrari, and J. Robertson, "Interpretation of Raman spectra of disordered and amorphous carbon", Phys. Rev. B, 61(20) (2000) 14095

39 E. Liu, X. Shi, B.K. Tay, L.K. Cheah, H.S. Tan, J.R. Shi, and Z. Sun, "Micro-Raman spectroscopic analysis of tetrahedral amorphous carbon films deposited under varying conditions", J. Appl. Phys. 86(11) (1999) 6078

40 R.O. Dillo, J.a. Woollam, and V. Katkanant, "Use of Raman scattering to investigate disorder and crystallite formation in as-deposited and annealed carbon films", Phys. Rev. B 29 (1984) 3482

41 H. Tsai, and D.B. Bogy, "Characterization of diamondlike carbon films and their application as overcoats on thin-film media for magnetic recording", J. Vac. Sci. Technol. A 5 (1987) 3287

42 S. Prawer, K.W. Nugent, Y. Lifshitz, G.D. Lempert, E. Grossman, J. Kulik, I. Avigal, and R. Kalish, "Systematic variation of the Raman spectra of DLC films as a function of sp2:sp3 composition", Diamond Relat. Mater. 5 (1996) 433

43 T. Young, "An essay on the cohesion of fluids", Philos. Trans. R. Soc. Lond. 9 (1805) 255

44 S. Wu, Polymer Interface and Adhesion, Marcel Dekker, New York, 1982, pp. 178–181

45 A. Argon, V. Gupta, H. Landis, and J. Cornie, "Intrinsic toughness of interfaces", Mater. Sci. Enging. A 107 41

46 W.C. Oliver, and G.M. Pharr, "An improved technique for determining hardness and elastic modulus using load and displacement sensing indentation experiments", J. Mater. Res. 7 (1992) 1564

47 F. Santerre, M.A. El Khakani, M. Chaker, J.P. Dodelet, "Properties of TiC thin films grown by pulsed laser deposition", Appl. Surf. Sci. 148 (1999) 24

48 X.Z. Ding, Y.J. Li, Z. Sun, B.K. Tay, S.P. Lau, and G.Y. Chen, "Electron field emission from Ti-containing tetrahedral amorphous carbon films deposited by filtered cathodic vacuum arc", J. Appl. Phys. 88(11) (2000) 6842

49 M.V. Klein, J.A. Holy, and W.S. Williams, "Raman scattering induced by carbon vacancies in TiCx", Phys. Rev. B 17 (1978) 1546

50 X. Shi, D. Flynn, B.K. Tay, S. Prawer, K.W. Nugent, S.R.P. Silva, Y. Lifshitz, and W.I. Milne, "Mechanical properties and Raman spectra of tetrahedral amorphous carbon films with high sp(3) fraction deposited using a filtered cathodic arc", Phil. Mag. B 76(3) (1997) 351

51 X. Shi, L. K. Cheah, J.R. Shi, Z. Sun and B.K. Tay, "On the upper limit of content in tetrahedral amorphous carbon film", J. Phys.: Condens. Matter 11 (1999) 185

52 J.S. Chen, S.P. Lau, B.K. Tay, G.Y. Chen, Z. Sun, Y.Y. Tan, and G. Tan, "Surface energy of amorphous carbon films containing iron", J. Appl. Phys. 89(12) (2001) 7814

53 H. Han, F. Ryan, and M. McClure, "Ultra-thin tetrahedral amorphous carbon film as slider overcoat for high areal density magnetic recording", Surf. Coat. Technol. 120-121(1999) 579

54 A.W. Neumann, "Contact angles and their temperature dependence: thermodynamic status, measurement, interpretation and application", Adv. Collid. Interface. Sci. 4 (1974) 105

55 P. Zhang, B.K. Tay, G.Q. Yu, and S.P. Lau, "Surface energy of metal containing amorphous carbon films deposited by filtered cathodic vacuum arc", Diamond & Related Materials, 13(3) (2004) 459-464

56 R.D. Sun, Akira Nakajima, Akira Fujishima, Toshiya Watanabe, and Kazuhito Hashimoto, "Photoinduced Surface Wettability Conversion of ZnO and TiO2 Thin Films", J. Phys. Chem. B 105 (2001) 1984

57 Masahiro Miyauchi, Nobuo Kieda, Shunichi Hishita, Takefumi Misuhashi, Akira Nakajima, Toshiya Watanabe, Kazuhito Hashimoto, "Reversible wettability control of TiO2 surface by light irradiation", Surf. Sci. 511 (2002) 401

58 P. Zeman, and S. Takabayashi, "Self-cleaning and antifogging effects of TiO_2 films prepared by radio frequency magnetron sputtering", J. Vac. Sci. Technol. A 20(2) (2002) 388

59 Rong Wang, Kazuhito Hashimoto, Akira Fujishima, Makoto Chikuni, Eiichi Kojima, Atsushi Kitamura, Mitsuhide Shimohigoshi, Toshiya Watanabe, "Light-induced amphiphilic surfaces", Nature 388 (1997) 431

60 J.P. Sullivan, T.A. Friedmann and A.G. Baca, "Stress Relaxation and Thermal Evolution of Film Properties in Amorphous Carbon", J. Electron. Mater. 26 (1997) 1021

61 A.C. Ferrari, B. Kleinsorge, N.A. Morrison, "Stress reduction and bond stability during thermal annealing of tetrahedral amorphous carbon", J. Appl. Phys. 85(10) (1999) 7191

62 Q.F. Huang, S.F. Yoon, Rusli, H. Yang, J. Ahn, Q. Zhang, "Molybdenum-containing carbon films deposited using the screen grid technique in an electron cyclotron resonance chemical vapor deposition system", Diamond Relat. Mater. 9 (2000) 534

63 J. Robertson, "The deposition mechanism of diamond-like a-C and a-C: H", Diamond Relat. Mater. 3 (1994) 361

64 K.L. Soh, W.P. Kang, J.L. Davidson, A. Wisitsora-at, G. Swain, D.E. Cliffel, "CVD diamond anisotropic film as electrode for electrochemical sensing", Sensor Actuat. B. Chem. 91 (1-3) (2003) 39

65 C. Levy-Clement, N.A. Ndao, A. Katty, M. Bernard, A. Deneuville, C. Comninellis, A. Fujishima, "Boron doped diamond electrodes for nitrate elimination in concentrated wastewater", Diamond Relat. Mater. 12 (3-7) (2003) 606

66 R. C. Mani, S. Sharma, M.K. Sunkura, J. Gullapalli, R.P. Baldwin, R. Rao, A.M. Rao, and J.M. Cowley, "Synthesis and Electrochemical Characteristics of a Nanocomposite Diamond Electrode", Electroch. Solid-State Lett. 5(6) (2002) E32

67 Application Notes from Autolab Electrochemical instruments (http://www.ecochemie.nl/applnotes.htm)

68 C.H. Hamann, A. Hamnett, W. Wielstich, Electrochemistry, Willey-VCH, Weinheim, 1998, p. 241

69 J. Li, L.S. Chia, N.K. Goh, S.N. Tan, "Renewable silica sol–gel derived carbon composite based glucose biosensor", J. Electroanal. Chem. 460 (1999) 234

70 R.N. Adams, Electrochemistry at Solid Electrodes, Marcel Dekker, Inc, New York, 1969, p. 37

71 A.J. Bard, L.R. Faulkner, Electrochemical Methods: Fundamentals and Applications, Wiley, New York, 1980, p. 412

72 H. Randhawa, "High-rate deposition of Al_2O_3 films using modified cathodic arc plasma deposition processes", J. Vac. Sci. Technol. A 7(3) (1989) 2346

73 M.A. Khakani, M. Chaker, A. Jean, S. Boily, H. Pepin, J.C. Kieffer, and S.C. Gujrathi, "Effect of rapid thermal annealing on both the stress and the bonding states of a-SiC:H films", J. Appl. Phys. 74 (1993) 2834

74 W.K. Choi, T.Y. Ong, L.S. Tah, F.C. Loh, and K.L. Tan, "Infrared and x-ray photoelectron spectroscopy studies of as-prepared and furnace-annealed radio-frequency sputtered amorphous silicon carbide films", J. Appl. Phys. 83 (1998) 4968

75 X. Zhang, W.H. Weber, W.C. Vassell, T.J. Potter, and M.A. Tamor, "Optical study of silicon-containing amorphous hydrogenated carbon", J. Appl. Phys. 83 (1998) 2820

76 A.S. Kumbhar, D.M. Bhusari, and S.T. Kshirsagar, "Growth of clean amorphous silicon–carbon alloy films by hot-filament assisted chemical vapor deposition technique", Appl. Phys. Lett. 66 (1995) 1741

77 G. Morell, R.S. Katiyar, S.Z. Weisz, and I. Balberg, "Characterization of the silicon network disorder in hydrogenated amorphous silicon carbide alloys with low carbon concentrations", J. Non-cryst. Solids 194 (1996) 78

78 G.Y. Chen, J.S. Chen, Z. Sun, Y.J. Li, S.P. Lau, B.K. Tay, and J.W. Chai, "Field emission properties and surface structure of nickel containing amorphous carbon", Appl. Surf. Sci. 180 (2001) 185

79 A.K. Sikder, T. Sharda, D.S. Misra, D. Chandrasekaram, and P. Selvam, "Chemical vapour deposition of diamond on stainless steel: The effect of Ni-diamond composite coated buffer layer", Diamond Relat. Mater. 7 (1998) 1010

80 Harold P. Klug, and L. E. Alexander, X-ray Diffraction Prodedures for Polycrystalline and Amorphous Materials (Wiley-Interscience, New York, 1974)

81 G.W. McClure, "Plasma expansion as a cause of metal displacement in vacuum-arc cathode spots", J. Appl. Phys. 45(5) 1974 2078

82 M. Takeuchi, and T. Kubono, "Temperature and Metal Vapor Near the Cathode in Copper Breaking Arcs According to Spectroscopic Measurement", IEEE TRANS. on PLASMA SCI., 28(3), 2000, 991

83 http://www.webelements.com

84 S. Shalev, R.L. Boxman, and S. Goldsmith, "Velocities and emission rates of cathode-produced molybdemum macroparticles in a vacuum arc", J. Appl. Phys. 58(7) 1985 2503

85 J. robsertson, "Diamond-like amorphous Carbon", Mater. Sci. and Eng. R 37, 2002, 129

86 Y. Pauleau, F. Thiery, "Deposition and characterization of nanostructured metalycarbon composite films", Surf. & Coat. Tech. 180 –181 (2004) 313

87 C. Corbella, M. Vives, A. Pinyol, E. Bertran, C. Canal, M.C. Polo, J.L. Andujar, "Preparation of metal (W, Mo, Nb, Ti) containing a-C:H films by reactive magnetron sputtering", Surf. & Coat. Tech. 177 – 178 (2004) 409

88 C. Corbella, G. Oncins, M.A. Go´mez, M.C. Polo, E. Pascual, J. Garcı´a-Ce´spedes,J.L. Andujar, E. Bertran , "Structure of diamond-like carbon films containing transition metals deposited by reactive magnetron sputtering", Diamond & Relat. Mater., 14 (2005) 1103

89 Rusli, S.F. Yoon, H. Yang, J. Ahna, Q.F. Huang, Q. Zhang, Y.P. Guo, C.Y. Yang, E.J. Teo, A.T.S. Wee, A.C.H Huan, "Investigation of tungsten incorporated amorphous carbon film", Thin Solid Films 355-356 (1999) 174

90 Rusli, S.F. Yoon, Q.F. Huang J. Ahn, Q. Zhang, H. Yang, Y.S. Wu, E.J. Teo, T. Osipowicz, F. Wattb, "Metal-containing amorphous carbon film development using electron cyclotron resonance CVD", Diamond & Relat. Mater. 10 (2001) 132

91 J. Robertson, "Diamond like amorphous carbon", Mater. Sci. & Engin. R 37 (2002) 129

92 Q.F. Huang, "Fabrication & Characterization of Metal containing carbon films", PhD thesis of Nanyang Technology University, p.75

93 S. Iijima, "Helical microtubules of graphitic carbon", Nature 354 (1991) 56

94 A. Javey, J. Guo, Q. Wang, M. Lundstrom, H. Dai, "Ballistic carbon nanotube field-effect transistors", Nature 424 (2003) 654

95 J. A. Misewich, R. Martel, Ph. Avouris, J. C. Tsang, S. Heinze, J. Tersoff, "Electrically induced optical emission from CNT FET", Science 300 (2003) 783

96 K.P. Yung, J. Wei, Z.F. Wang, B.K. Tay, P. Zhang, "Effects of Catalyst Layer on Carbon Nanotubes Growth", the 1st International Conference on Nanotechnology, Jul 13-17, 2003, Singapore

97 H.Y. He, X. Cao, L.J. Lee, "Design of a novel hydrogel-based intelligent system for controlled drug release", J. CONTROL. RELEASE. 95(3) (2004) 391

98 V. Venkateswarlu, K. Manjunath, "Preparation, characterization and in vitro release kinetics of clozapine solid lipid nanoparticles", J. CONTROL. RELEASE. 95(3) (2004) 627

99 U.S. Toti, T.M. Aminabhavi, "Modified guar gum matrix tablet for controlled release of diltiazem hydrochloride", J. CONTROL. RELEASE. 95(3) (2004) 567

100 Y. Akiyama,Y. Nagasaki,K. Kataoka, "Synthesis of Heterotelechelic Poly(ethylene glycol) Derivatives Having -Benzaldehyde and -Pyridyl Disulfide Groups by Ring Opening Polymerization of Ethylene Oxide Using 4-(Diethoxymethyl)benzyl Alkoxide as a Novel Initiator", BIOCONJUGATE. CHEM. 15(2) (2004) 424

101 Y.H. Qiu, J. Garren, E. Samar, G. Cao, C. Abrahm, H.S. Cheskin, K.R. Engh, "Once-a-day controlled-release dosage form of Divalproex sodium II: development of a predictive in vitro drug release method", J. Pharm. Sci-us. 92(11) (2003) 2317

102 M. Levian, M.H. Rubinstein, "", Drug. Dev. Ind. Pharm. 28(5) (2002) 495

103 F.Z. Cui, D.J. Li, "A review of investigations on biocompatibility of diamond-like carbon and carbon nitride films", Surf. Coat. Technol. 131 (2000) 481

104 M. Allen, F. Law, "The Effect of Ultrasonic Vibration on the Compaction Characteristics of Ibuprofen", N. Rushton, Clin. Mater. 17 (1994) 1

105 I. Dion, X. Roques, E. Ch. Baquey, B.B. Baudet, N. More Cathalinat, Biomed. Mater. Eng. 3 (1993) 169

106 P.A. Dearnley, K.L. Dahm, H. Cimenoglu, "The corrosion–wear behaviour of thermally oxidised CP-Ti and Ti–6Al–4V", Wear, 256(5) (2004) 469